

ARMY RESEARCH LABORATORY



Evaluation of IKTS Transparent Polycrystalline Magnesium Aluminate Spinel (MgAl_2O_4) for Armor and Infrared Dome/Window Applications

by James W. McCauley and Parimal Patel

ARL-SR-262

March 2013

NOTICES

Disclaimers

The findings in this report are not to be construed as an official Department of the Army position unless so designated by other authorized documents.

Citation of manufacturer's or trade names does not constitute an official endorsement or approval of the use thereof.

Destroy this report when it is no longer needed. Do not return it to the originator.

Army Research Laboratory

Aberdeen Proving Ground, MD 21005-5069

ARL-SR-262

March 2013

Evaluation of IKTS Transparent Polycrystalline Magnesium Aluminate Spinel ($MgAl_2O_4$) for Armor and Infrared Dome/Window Applications

**James W. McCauley and Parimal Patel
Weapons and Materials Research Directorate, ARL**

REPORT DOCUMENTATION PAGE			Form Approved OMB No. 0704-0188	
<p>Public reporting burden for this collection of information is estimated to average 1 hour per response, including the time for reviewing instructions, searching existing data sources, gathering and maintaining the data needed, and completing and reviewing the collection information. Send comments regarding this burden estimate or any other aspect of this collection of information, including suggestions for reducing the burden, to Department of Defense, Washington Headquarters Services, Directorate for Information Operations and Reports (0704-0188), 1215 Jefferson Davis Highway, Suite 1204, Arlington, VA 22202-4302. Respondents should be aware that notwithstanding any other provision of law, no person shall be subject to any penalty for failing to comply with a collection of information if it does not display a currently valid OMB control number.</p> <p>PLEASE DO NOT RETURN YOUR FORM TO THE ABOVE ADDRESS.</p>				
1. REPORT DATE (DD-MM-YYYY)	2. REPORT TYPE		3. DATES COVERED (From - To)	
March 2013	Final		January 2009–January 2011	
4. TITLE AND SUBTITLE			5a. CONTRACT NUMBER	
Evaluation of IKTS Transparent Polycrystalline Magnesium Aluminate Spinel (MgAl ₂ O ₄) for Armor and Infrared Dome/Window Applications			5b. GRANT NUMBER	
			5c. PROGRAM ELEMENT NUMBER	
6. AUTHOR(S)			5d. PROJECT NUMBER	
James W. McCauley and Parimal Patel			5e. TASK NUMBER	
			5f. WORK UNIT NUMBER	
7. PERFORMING ORGANIZATION NAME(S) AND ADDRESS(ES)			8. PERFORMING ORGANIZATION REPORT NUMBER	
U.S. Army Research Laboratory ATTN: RDRL-WM Aberdeen Proving Ground, MD 21005-5069			ARL-SR-262	
9. SPONSORING/MONITORING AGENCY NAME(S) AND ADDRESS(ES)			10. SPONSOR/MONITOR'S ACRONYM(S)	
			11. SPONSOR/MONITOR'S REPORT NUMBER(S)	
12. DISTRIBUTION/AVAILABILITY STATEMENT				
Approved for public release; distribution is unlimited.				
13. SUPPLEMENTARY NOTES				
14. ABSTRACT				
<p>This report is the first detailed study attempting to relate the ballistic performance of a transparent armor ceramic material with two significantly different grain sizes to a comprehensive set of material characteristics (phase, microstructure, and defects) and quasi-static and dynamic properties. Two fine-grain polycrystalline spinels (magnesium aluminate) of nominal size 0.6 µm (205) and 1.6 µm (200), fabricated under the direction of Dr. Andreas Krell of the Fraunhofer Institute for Ceramic Technologies and Sintered Materials in Dresden, Germany, were studied in depth. The key characteristics and properties determined consisted of the following: microstructural analysis, nondestructive ultrasonic evaluation, porosity determined indirectly from density measurements, hardness, bulk plasticity from load/Knoop hardness curves, spherical indentation, quasi-static bend-bar strength, dynamic compressive strength, and quantification of fragmentation in a ballistic impact event at 850 and 1100 m/s. The fine-grain spinel material V50 was determined to be about 60 ft/s (18 m/s) better than the coarser grain material. This is close to a difference that is considered to be significant.</p>				
15. SUBJECT TERMS				
spinel, fine-grain, properties, ballistic, transparent armor ceramic				
16. SECURITY CLASSIFICATION OF:		17. LIMITATION OF ABSTRACT	18. NUMBER OF PAGES	19a. NAME OF RESPONSIBLE PERSON
a. REPORT	b. ABSTRACT	c. THIS PAGE	UU	James W. McCauley
Unclassified	Unclassified	Unclassified	102	19b. TELEPHONE NUMBER (Include area code) 410-306-0744

Contents

List of Figures	v
List of Tables	ix
Acknowledgments	x
Executive Summary	xi
1. Background and Objectives	1
2. Approach	2
3. Samples	3
4. Results	3
4.1 General Characterization.....	3
4.2 Microstructures.....	4
4.3 Advanced Nondestructive Ultrasound Characterization	6
4.3.1 Introduction	6
4.3.2 Acoustic Spectroscopy Theory	7
4.3.3 Experimental Procedure	8
4.3.4 Results	9
4.3.5 Conclusions	15
4.4 Quasi-Static Mechanical Properties and Raman Spectroscopy Characterization	19
4.4.1 Mechanical Properties and Density	19
4.4.2 Hardness Measurements.....	22
4.5 Bulk Plasticity and Transitional Velocity from Load/Hardness Curves	25
4.5.1 Raman Spectroscopy Analysis	26
4.6 Elastic-Plastic Indentation Response of Transparent Polycrystalline Spinel	29
4.6.1 Introduction and Background.....	29
4.6.2 Inelastic Deformation of Transparent Fine-Grained Spinel	33
4.7 Dynamic Compressive Strength of Micron and Sub-Micron Grain Polycrystalline Spinel ($MgAl_2O_4$)	51
4.7.1 Introduction	51

4.7.2	Specimen Details	51
4.7.3	Experimental Procedures	53
4.7.4	Experimental Results	54
4.7.5	Summary of Results	62
4.8	Dynamic Fragmentation of Spinel	66
4.8.1	Introduction	66
4.8.2	Experimental Configuration and Techniques	67
4.8.3	Ballistic Results	68
4.8.4	High-Speed Photography	69
4.8.5	Fragmentation Analysis	72
5.	Summary and Conclusions	79
Distribution List		81

List of Figures

Figure 1. The 0.6- μm spinel (205 series)	4
Figure 2. The 1.6–2.0- μm spinel (200 series).....	4
Figure 3. Various magnification SEM images of spinels etched in boiling phosphoric acid: left column, sample 205 (0.6 μm); right column, sample 200 (1.6 μm).....	5
Figure 4. An oscilloscope view illustrating top and bottom surface reflections. The gates surrounding the bottom surface reflections correlate with the window used to perform the FFT on the reflected signal.	7
Figure 5. The signal output of the 20-MHz planar transducer used in this study. The FFT taken was of the top surface reflection of a polished silicon carbide mirror.	9
Figure 6. The C-scan map of overall signal attenuation coefficient measured using a 20-MHz transducer on the spinel sample with 1.6- μm mean grain size. The scale used is in units of dB/cm.....	10
Figure 7. Acoustic spectroscopy results for three regions in the 1.6- μm -grain spinel with single Gaussian curve fitting.....	10
Figure 8. The C-scan map of overall signal attenuation coefficient measured using a 20-MHz transducer on the spinel sample with 0.6- μm mean grain size. The scale used is in units of dB/cm.....	12
Figure 9. The attenuation coefficient spectra from the 0.6- μm -grain spinel with single Gaussian curve fitting.	12
Figure 10. Attenuation coefficient spectrum of polycrystalline spinel over region showing visible yellow inclusion.	14
Figure 11. Overall signal attenuations of 200- and 205-series spinel samples.....	14
Figure 12. Attenuation coefficient spectra comparison between spinel samples after correction factors have been taken to account for reflective and diffractive losses.	15
Figure 13. Spatial position of each MOR/C-N bar in relation to the original spinel tile.....	21
Figure 14. Weibull plots of two series of spinel materials.	22
Figure 15. Knoop hardness for spinel 200 and 205.	23
Figure 16. Vickers hardness for spinel 200 and 205.....	23
Figure 17. Knoop vs. Vickers hardness for spinel 205.	24
Figure 18. Knoop vs. Vickers hardness for spinel 200.	24
Figure 19. Raman spectra of spinel standard, 200/3 and 205/18.	26
Figure 20. Schematic of the instrumented indentation test setup.	30
Figure 21. Schematic of the direct contact area measurement test system.	31

Figure 22. SEM micrograph depicting grain size and morphology, and accompanying binary images created using Image J to enhance the grain boundaries. Top images correspond to the small-grain spinel and bottom images to the large-grain spinel.	35
Figure 23. Binary images depicting the grains that were used to determine the Feret's diameter. The left image corresponds to the small-grain spinel and the right to the large-grain spinel (see figure 3).	35
Figure 24. Histogram of Feret's diameter distribution for small-grained and large-grained spinel depicted in figure 3.	36
Figure 25. EDS spectrum for the small- and large-grained spinel.	36
Figure 26. XRD pattern for small- and large-grain spinel matched to ICDD card 00-021-1152 spinel MgAl ₂ O ₄	37
Figure 27. Enlarged view of the largest peak in the XRD pattern for the small- and large-grain spinel, illustrating the larger degree of peak broadening seen in the small-grain spinel.	37
Figure 28. Differential interference contrast (DIC) images showing the typically observed cracking modes in spinel after the application of 50-, 100-, and 200-N maximum compressive forces, using a 261-μm-radius diamond indenter. Top images correspond to the small-grain spinel and the bottom to the large.	38
Figure 29. SEM micrograph showing the typically observed cracking modes in spinel after the application of 250-N maximum compressive forces, using a 261-μm-radius diamond indenter. Left image corresponds to the small-grain spinel and the right to the large.	39
Figure 30. SEM micrograph showing the fractured surface of a three-point bend-bar in which an indentation of 300 N was placed. The left image corresponds to the small-grain spinel and the right image to the large. Note the remnant indenter impression and the intergranular fracture regions below them.	40
Figure 31. Optical profilometer line scans showing the typical surface profiles of the (a) small-(205-2) and (b) large-grain (200-11) spinel as a function of the applied force. Note that the pile-up increases with increasing indentation force.	41
Figure 32. Comparison of impression shape in the small-grain spinel after loading to 200 N with the indenter tip shape. The profilometer scan is shown in green and the impression radius (black) was determined to be 606 μm. The contact area shape (indenter radius, 261 μm) at maximum load is shown in blue. The contact diameter at maximum load is the same as the remnant impression diameter.	41
Figure 33. Meyer's hardness values measured using optical profilometer scans on the small-(205/2) and large-grain (200/11) spinel. Error bars correspond to the standard error of the mean within each given test condition.	42
Figure 34. Representative raw force-displacement curves at maximum loads of 50 N (blue), 100 N (red), and 200 N (green), showing the full loading and unloading sequence for the small-grain spinel using a 261-μm radius spherical diamond indenter.	43
Figure 35. Comparison of a raw (green) and a machine stiffness-corrected (orange) force-displacement curve showing the full loading and unloading sequence for the small-grain (205/2) spinel using a 261-μm-radius spherical diamond indenter.	45

Figure 36. Comparison of indentation stress-strain curves obtained using the Oliver-Pharr and Modified Bushby methods on small- (205/2) and large-grain (200/11) spinel using a 261- μm -radius spherical diamond indenter. Error bars corresponding to the standard error of the mean are contained within the marker.....	46
Figure 37. Comparison of indentation stress-strain curves obtained using the Modified Bushby methods on small- (205/2) and large-grain (200/11) spinel using a 261- μm -radius spherical diamond indenter. Error bars correspond to the standard error of the mean are contained within the marker. Equations are power law fits to the data.....	47
Figure 38. Specimen Geometry. Specimens are loaded along the h dimension. Nominal dimensions: $b, w = 3.8 \text{ mm}$, $h = 3.4 \text{ mm}$, and $k = 425 \mu\text{m}$	52
Figure 39. Comparison of optically visible defects in specimens cut from plates 200/14 (1.6 μm) and 205/04 (0.6 μm).....	53
Figure 40. Schematic of the Kolsky bar set-up.....	54
Figure 41. Specimen SP_200/14-07: $5.4 \times 10^{-5} \text{ MPa}/\mu\text{s}$; strain rate $1.4 \times 10^{-4} \text{ s}^{-1}$; 1.6- μm grain size.....	55
Figure 42. Specimen SP_200/14-06: stress rate $4.4 \times 10^{-3} \text{ MPa}/\mu\text{s}$; strain rate $1.6 \times 10^{-2} \text{ s}^{-1}$; 1.6- μm grain size.....	56
Figure 43. Specimen SP_205/04-04: stress rate $5.4 \times 10^{-5} \text{ MPa}/\mu\text{s}$; strain rate $2 \times 10^{-4} \text{ s}^{-1}$; 0.6- μm grain size.....	56
Figure 44. Specimen SP_205/04-09: stress rate $4.2 \times 10^{-3} \text{ MPa}/\mu\text{s}$; strain rate $1.5 \times 10^{-2} \text{ s}^{-1}$; 0.6- μm grain size.....	57
Figure 45. Specimen SP_200/14-08: stress rate $225 \text{ MPa}/\mu\text{s}$; strain rate 800 s^{-1} ; 1.6- μm grain size; 2- μs interframe time.....	58
Figure 46. Specimen SP_200/14-09: strain rate 1500 s^{-1} ; 1.6- μm grain size; 2- μs interframe time.....	59
Figure 47. SP_205/04-05: stress rate $180 \text{ MPa}/\mu\text{s}$; strain rate 650 s^{-1} ; 0.6- μm grain size; 5- μs interframe time.....	59
Figure 48. Specimen SP_205/04-06: stress rate $200 \text{ MPa}/\mu\text{s}$; strain rate 700 s^{-1} ; 0.6- μm grain size; 2- μs interframe time.....	60
Figure 49. Specimen SP_205/04-07: stress rate $350 \text{ MPa}/\mu\text{s}$; strain rate 1300 s^{-1} ; 0.6- μm grain size; 3- μs interframe time.....	61
Figure 50. Specimen SP_205/04-08: stress rate $400 \text{ MPa}/\mu\text{s}$; strain rate 1500 s^{-1} ; 0.6- μm grain size; 3- μs interframe time.....	61
Figure 51. Summary of compressive strengths as a function of loading rate.....	62
Figure 52. Postmortem SEM micrographs of a fragment from a 1.6- μm -grain specimen. The areas of higher magnification highlight an area of incomplete specimen densification. This roughly spherical cluster is likely the same type of flaw that is optically visible (see figure 2).....	64
Figure 53. Postmortem SEM micrograph showing that both transgranular and intergranular fracture modes were active during failure.....	64

Figure 54. Schematic of ballistic test configuration (left) and target (right).	67
Figure 55. Residual projectile material from tests at 850 m/s (left) and 1100 m/s (right).....	69
Figure 56. Selection of high-speed photographs from impact on spinel 205 at 850 m/s.....	70
Figure 57. High-speed photographs of fragment ejection from impacted spinel ceramic (spinel 205, 850 m/s).....	71
Figure 58. Fragment mass distribution; mean values from three tests with each configuration	73
Figure 59. (a) Cumulative mass, and (b) close-up of cumulative mass plot.....	73
Figure 60. Schematic of the laser lightsheet illumination technique.....	74
Figure 61. Average fragment size vs. time; moving average (mean of 50 frames).....	75
Figure 62. Average fragment size vs. time; moving average (mean of 10 frames).....	76

List of Tables

Table 1. List of characterization techniques utilized to evaluate the IKTS spinel.	2
Table 2. Curve fitting parameters for attenuation coefficient spectra from the 1.6- μm -grain spinel.	11
Table 3. Curve fitting parameters for attenuation coefficient spectra from the 0.6- μm -grain spinel.	13
Table 4. MOR and density.	21
Table 5. Fracture toughness.	21
Table 6. Bulk plasticity and predicted transitional velocities.	25
Table 7. Details of specimen dimensions and density.	52
Table 8. Summary of experimental results.	55
Table 9. Measured crack velocities.	71
Table 10. Fragmentation data collected for all test conditions.	72

Acknowledgments

This detailed study of two fine-grain polycrystalline spinels was carried out in collaboration with investigators Jamie Kimberly and Kaliat Ramesh of the Material Centers of Excellence at The Johns Hopkins University; Andrea Muller and David Green of Penn State University; Vladislav Domnich, Douglas Slusark, Stephen Bottiglieri, Andrew Portune, and Rich Haber of Rutgers University; Elmar Strassburger, Martin Hunzinger, and Steffen Bauer of the Fraunhofer Institute for High-Speed Dynamics, Ernst-Mach-Institute (EMI); and Jeffrey Swab, Eric Ngo, and Corydon Hilton of the U.S. Army Research Laboratory.

Executive Summary

Current threat requirements have led to increasingly thicker and heavier transparent armor being installed onto U.S. Department of Defense (DOD) ground vehicles. It has been known for some time that the use of transparent ceramics significantly reduces the weight and thickness of the transparent armor by as much as 50%. Currently, the three major transparent ceramic materials available are magnesium aluminate spinel (MgAl_2O_4), aluminum oxynitride spinel ($\text{Al}_{23}\text{O}_{27}\text{N}_5$, or AlON), and single crystal aluminum oxide (Al_2O_3 , or sapphire). There are significant domestic programs looking at scaling up these materials to insert them into ground vehicles. The MgAl_2O_4 spinel, besides being an alternative transparent armor material, it is also a very attractive material for mid-wavelength infrared (IR) domes and sensor windows because it has a higher transmission at longer wavelengths than sapphire or AlON, thus resulting in much more sensitivity at these wavelengths for certain applications.

The Fraunhofer Institute for Ceramic Technologies and Systems (*Fraunhofer-Institut für Keramische Technologien und Systeme*, IKTS) in Dresden, Germany, under the direction of Dr. Andreas Krell, has fabricated a series of polycrystalline magnesium aluminate spinels with controlled microstructures and grain sizes that appear to have mechanical properties superior to polycrystalline spinel currently available in the United States.^{1,2} The objective of this program is to evaluate these IKTS spinels as ballistic and durable IR dome/window material. The two components of this program include acquisition of the spinel via an employment regulation order contract to IKTS and an evaluation phase conducted by the U.S. Army Research Laboratory.

These results will be compared with domestically available spinel to aid in future development. This program is highly relevant to the Army's current and future force for the development of lighter and thinner transparent armor, and for the need for durable IR windows and domes. It will also help answer one of the critical questions about the effect of grain size on the mechanical, optical, and ballistic properties of transparent ceramic materials.

Tables ES-1 and ES-2 summarize the findings of this effort in tabular form. The specific approaches, experimental techniques, and detailed information are found in subsequent sections. These findings will be compared with characterization of domestically produced spinel, which has a much larger grain size of 300–500 μm in a bimodal distribution. This characterization is ongoing under the ARL mission program. This report is the result of an extensive collaboration of many groups and is broken into sections describing the different characterizations conducted by each group.

¹ Krell, A.; Bales, A. Grain Size Dependent Hardness of Transparent Magnesium Aluminate Spinel, *Int. J. Adv. Comp. Tech.* **2010**, 8 (5), 1108–1114.

² Krell, A.; Hutzler, T.; Klimke, J. Advanced Spinel and Sub-micron Al_2O_3 for Transparent Armor Applications. *J. Europ. Ceram. Soc.* **2009**, 29, 275–281.

Table ES-1. Summary of key measured properties.

Property	Unit	Spinel 205	Spinel 200 ^a
Nominal grain size	µm	0.6	1.6
Actual grain size	nm	350	950
Johns Hopkins density on test specimens: $3.8 \times 3.8 \times 3.5$ mm	g/cm ³	3.552 (3.503–3.599)	3.539 (3.512–3.556)
Rutgers density on B-size bend-bars: $4 \times 3 \times 45$ mm	g/cm ³	3.57	3.57
Visible defects	—	Minimal	Many
Lithium fluoride (LiF) pore clusters	µm	—	0.45
Hardness Knoop (2 kg)	GPa	12.3	12.2
Hardness Vickers (2 kg)	GPa	15.0	15.0
Meyers hardness (sphere), radius = 261 µm	GPa	14.8	13.5
Indentation yield stress	GPa	12.16	11.6
Indentation radial cracking at 100 N	—	No	Yes
Indentation radial cracking at 200 N	—	Yes	Yes
Maximum depth of residual impression—all loads	—	Less	More
Onset of indentation dimpling: intercept	N	49	41
Onset of indentation dimpling: extrapolation	N	34	32
Modulus of rupture: B-size	MPa	258	262
Weibull modulus	—	8.72	8.15
Fracture toughness	MPa-m ^{1/2}	2.11	2.13
Compressive strength: quasi-static 2×10^{-4}	GPa	3.02	3.40
Compressive strength: quasi-static 1.5×10^{-2}	GPa	2.75	3.25
Compressive strength: dynamic 1×10^{-2}	GPa	3.53	4.00
Compressive strength: dynamic 1×10^{-3}	GPa	4.35	4.20
Perpendicular impact depth at 850 m/s	mm	1.2	1.1
Perpendicular impact depth at 1100 m/s	mm	16.3	15.8
Dynamic fragmentation: 850 m/s >2 mm	g	39	57.1
Dynamic fragmentation: 1100 m/s >2 mm	g	44.7	47.5
Mean velocity of radial cracks @ 850 m/s	m/s	2938	2954
Mean velocity of radial cracks @ 1100 m/s	m/s	2992	3158
Mean expansion of circular zone @ 850 m/s	m/s	926	830
Mean expansion of circular zone @ 1100 m/s	m/s	998	693
Bulk plasticity	—	10.87	11.90
Transitional velocity	m/s	1207	1219
Ballistic V 50	m/s	718 ± 4.9	700 ± 2.7

^aSome 200 samples are referred to as either 1.5 or 1.6 µm; these are the same materials.

Table ES-2. Summary of results.

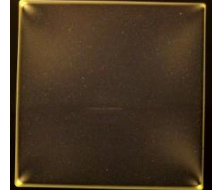
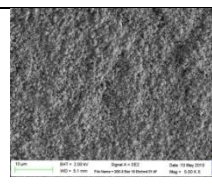
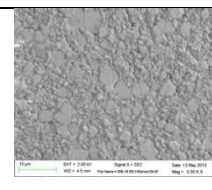
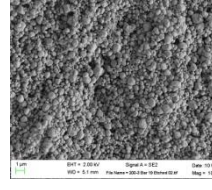
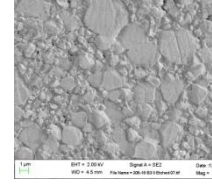
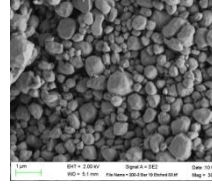
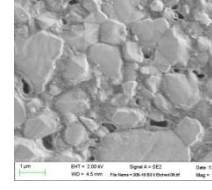
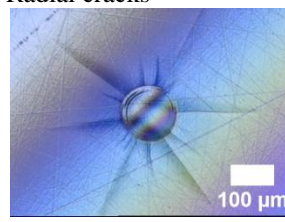
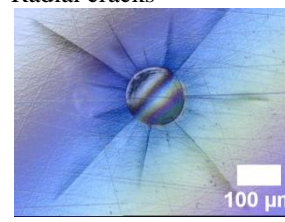
Property	Investigator	Sample 205	Sample 200^a
Nominal grain size	Krell, IKTS	0.6 μm	1.6 μm
Measured grain size	Muller and Green, Penn State	0.35 μm (0.2–1.0) Tight standard deviation	0.95 (0.2–1.6) Broad standard deviation
Plane light macrophotographs	Strassburger, EMI; Patel and McCauley, ARL		
Plane light macrophotographs	Strassburger, EMI; Patel and McCauley, ARL		
Cross-polarized light macrophotographs residual stress	Strassburger, EMI; Patel and McCauley, ARL		
Micrographs at 5000X	Slusark, Rutgers	 1 μm BHT = 2.00 kV Signal A = 1E2 Date: 13 May 2010 File Name = 205-01001.tif WID = 5.1 mm Mag = 5.00 K.X	 1 μm BHT = 2.00 kV Signal A = 1E2 Date: 13 May 2010 File Name = 200-01001.tif WID = 4.5 mm Mag = 5.00 K.X
Micrographs at 10,000X	Slusark, Rutgers	 1 μm BHT = 2.00 kV Signal A = 1E2 Date: 13 May 2010 File Name = 205-01002.tif WID = 5.1 mm Mag = 10.00 K.X	 1 μm BHT = 2.00 kV Signal A = 1E2 Date: 13 May 2010 File Name = 200-01002.tif WID = 4.5 mm Mag = 10.00 K.X
Micrographs at 30,000X	Slusark, Rutgers	 1 μm BHT = 2.00 kV Signal A = 1E2 Date: 13 May 2010 File Name = 205-01003.tif WID = 5.1 mm Mag = 30.00 K.X	 1 μm BHT = 2.00 kV Signal A = 1E2 Date: 13 May 2010 File Name = 200-01003.tif WID = 4.5 mm Mag = 30.00 K.X

Table ES-2. Summary of results (continued).

Property	Investigator	Sample 205	Sample 200
Attenuation coefficient of 200 and 205 acoustic spectroscopy	Bottiglieri, Portune, and Haber, Rutgers		
C-scan map of overall signal attenuation coefficient measured using a 20-MHz transducer; the scale used is in units of dB/cm.	Bottiglieri, Portune, and Haber, Rutgers		
Ultrasound nondestructive evaluation; attenuation coefficient spectrum of polycrystalline spinel over region showing visible yellow inclusion.	Bottiglieri, Portune, and Haber, Rutgers		Yellow: lithium fluoride inclusion/micro pore cluster (0.45 μm)
Hardness: HK2	Swab, ARL	12.7 GPa	12.6 GPa
Hardness: HK2	Domnich and Slusark, Rutgers	12.26 GPa	12.2 GPa
Hardness: HV2	Domnich and Slusark, Rutgers	15 GPa	15 GPa
Feret's grain-size diameter	Muller and Green, Penn State	0.35 μm	0.95 μm
SEM grain size by lineal intercept procedure (ASTM E112) ^b	Muller and Green, Penn State	0.27 μm Corrected = 0.36 μm	0.97 μm Corrected = 1.29 μm
Hardness: Meyers spherical indenter radius = 261 μm	Muller and Green, Penn State	14.8 GPa	13.5 GPa
Indentation yield stress	Muller and Green, Penn State	12.16 GPa	11.6 GPa
Indentation cracking at 100 N	Muller and Green, Penn State		

Table ES-2. Summary of results (continued).

Indentation cracking at 200 N	Muller and Green, Penn State		
Maximum depth for residual impression	Muller and Green, Penn State	Less for all loads	More for all loads
Elastic recovery 50 N 300 N	Muller and Green, Penn State	≈ 90% ≈ 45%	≈ 82% ≈ 40%
Onset of dimpling	Muller and Green, Penn State	49 N (x intercept) 34 N (extrapolation)	41 N 32 N
Modulus of rupture (standard)	Domnich and Slusark, Rutgers	258 MPa (37)	262 MPa (35)
Weibull modulus	Domnich and Slusark, Rutgers	8.72	8.15
Fracture toughness	Domnich and Slusark, Rutgers	2.11 MPa m ^{1/2}	2.13 MPa m ^{1/2}
Density on B-size bend-bars $4 \times 3 \times 45$ mm Percent of theoretical density	Domnich and Slusark, Rutgers; $\rho_t = 3.579 \text{ g/cm}^3$	3.57 g/cm ³ (0.01) ≈ 100%	3.57 g/cm ³ (0.01) ≈ 100%
Johns Hopkins density on test specimens (g/cm ³)	Test specimens $= 3.8 \times 3.8 \times 3.5$ mm	3.552 (3.503–3.599)	3.539 (3.512–3.556)
Compressive strength (GPa) Quasi-static Dynamic	Kimberly and Ramesh, Johns Hopkins	3.02–2.75 3.53–4.35	3.40–3.25 4.00–4.20
1100 M/S mean residual penetration	Strassburger, EMI; Patel and McCauley, ARL	16.8 mm	17.7 mm
Dynamic fragmentation (850 m/s) Fragment mass ≥ 2 mm	Strassburger, EMI; Patel and McCauley, ARL	39 g	51.1 g
Dynamic fragmentation 1100 m/s Fragment mass ≥ 2 mm	Strassburger, EMI; Patel and McCauley, ARL	44.7 g	47.5 g
Dielectric constant	Ngo, ARL	1 MHz: 9.31 10 GHz: 8.49	1 MHz: 9.31 10 GHz: 8.50
Loss tangent	Ngo ARL	0.005–0.001	0.005–0.001
Predicted transitional velocity – dwell (m/s)	Hilton, Swab, and McCauley, ARL	1207	1219
McCauley/Wilantewicz bulk plasticity parameter	Hilton, Swab, and McCauley, ARL	10.87	11.90

Notes: SEM = scanning electron microscopy.

EMI = Fraunhofer Institute for High-Speed Dynamics, Ernst-Mach-Institute (Kandern, Germany).

^aSome 200 samples are referred to as either 1.5 or 1.6 μm ; these are the same materials.

^bASTM E112. *Standard Test Methods for Determining Average Grain Size* 2012.

It is our belief that this is the first detailed study attempting to relate the ballistic performance of a transparent armor ceramic material with two significantly different grain sizes to a comprehensive set of material characteristics (phase, microstructure, and defects) and quasi-static and dynamic properties.

The fine-grain spinel material V50 was determined to be about 60 ft/s (18 m/s) better than the coarser grain material. This is close to a difference that is considered to be significant. Tables ES-1 and ES-2 depict the full set of materials characteristics and properties considered to be important in our analysis.

The key characteristics and properties we focused on consisted of the following: porosity determined indirectly from density measurements, hardness, bulk plasticity from load/Knoop hardness curves, spherical indentation, quasi-static bend-bar strength, dynamic compressive strength, and quantification of fragmentation in a ballistic impact event. Although the density determined from B-size bend-bars at 3.57 g/cm^3 for both materials is about 100% of theoretical density, densities determined from smaller Kolsky bar specimens show a much wider range and average densities of 3.552 g/cm^3 (99.5%) for the fine-grain material and 3.539 g/cm^3 (99.1%) for the coarser grain. Thus, on a finer scale, the fine-grain material has less overall porosity than the coarser grain material, which would lead to a larger V50 for the fine-grain material without considering other variations in the materials. The clearly visible yellow spots in the coarser grain material were not solid defects/inclusions that would nucleate cracks, but rather apparent clusters of very fine pores resulting from the lithium fluoride (LiF) sintering aid. Hardness determined from standard Knoop and Vickers tests showed no differences; however, using a Meyers test, the fine grain material had a hardness (14.8 GPa) slightly larger than the coarser grain material (13.5 GPa). In the spherical indentation test, the onset of observable dimpling in the fine-grain material occurred at a load of 49 N compared with the other material at 32 N, and the yield stress was, respectively, 12.16 and 11.6 GPa. These data suggest that the fine-grain material is more resistant to penetration than the coarser grain material. There were no significant differences in the bend strength, Weibull modulus, or fracture toughness.

The highest strain rate (10^3) compression test (more related to a ballistic event) resulted in a slightly larger compression strength (4.35 GPa) for the fine-grain material over the other material (4.20 GPa)—a very small difference. Two series of measurements were carried out in the ballistic tests: perpendicular impact depth into the aluminum (Al) backup plate and quantification of the fragmentation in the plates. In the former, there were very small differences, but the depth in the Al plate for the fine-grain material was slightly larger for both velocities than the coarser grain material. The total mass of the fragments greater than 2 mm was larger for both velocities in the coarse grain material. This suggests that if the Krell and Strassburger³ hypothesis is correct, then the coarser grain material should have a slower

³ Krell, A.; Strassburger, E. Hierarchy of Key Influences on the Ballistic Strength of Opaque and Transparent Armor, Advances in Ceramic Armor III. *Ceram. Eng. and Sci. Proc.* **2008**, 28 (5), 45–55.

penetration velocity after dwell than the fine-grain material. Finally, the transitional velocity was calculated using the McCauley-Wilantewicz methodology, resulting in 1207 m/s for the fine grain material and 1219 m/s for the other material.

From the current analysis of these data, it is hard to draw immediate relationships and conclusions relating to the dominant effects of the key material characteristics and properties at this point. There are ongoing investigations into domestically produced spinels that are more coarse-grained microstructures. The challenge in benchmarking these materials to the materials studied here are the differences in processing, such as powder source, concentrations of sintering/processing aids, and densification process. These differences lead to varying microstructures. However, additional systematic analysis may shed more clarity on this critical subject. It does seem to be clear that grain size can have a significant influence on ballistic performance. Further grain size reduction, i.e., further into the nanostructure range, may show even better ballistic performance for these materials.

INTENTIONALLY LEFT BLANK.

1. Background and Objectives

Current threat requirements have led to increasingly thicker and heavier transparent armor being installed onto U.S. Department of Defense (DOD) ground vehicles. It has been known for some time that the use of transparent ceramics significantly reduces the weight and thickness of the transparent armor by as much as 50%. Currently, the three major transparent ceramic materials available are magnesium aluminate spinel (MgAl_2O_4), aluminum oxynitride spinel ($\text{Al}_{23}\text{O}_{27}\text{N}_5$, or AlON), and single-crystal aluminum oxide (Al_2O_3 , or sapphire). There are significant domestic programs looking at scaled-up versions of these materials to insert them into ground vehicles. Spinel, besides being an alternative transparent armor material, it is also a very attractive material for mid-wavelength infrared domes and sensor windows because it has a higher transmission at longer wavelengths than sapphire or AlON, thus resulting in much more sensitivity at these wavelengths for certain applications.

The Fraunhofer Institute for Ceramic Technologies and Sintered Materials (*Fraunhofer-Institut für Keramische Technologien und Systeme*, IKTS) in Dresden, Germany, under the direction of Dr. Andreas Krell, has fabricated a series of polycrystalline magnesium aluminate spinels with controlled microstructures and grain sizes that appear to have mechanical properties superior to polycrystalline spinel currently available in the U.S.^{1,2} The objective of this program is to evaluate these grades of magnesium aluminate spinels produced by IKTS as ballistic and durable infrared (IR) dome/window material for use in ground vehicles. The two components of this program include acquisition of the spinel via an employment regulation contract to IKTS and an evaluation phase that will be conducted by the U.S. Army Research Laboratory (ARL).

(U) These results will be compared with domestically available spinel to aid in future development. This program is highly relevant to the U.S. Army's current and future force for the development of lighter and thinner transparent armor and for the need for durable IR windows and domes. It will also help answer one of the critical questions of the effect of grain size on the mechanical, optical, and ballistic properties of transparent ceramic materials.

Previous work at IKTS on controlled grain-size aluminum oxide (Al_2O_3) armor ceramic material has clearly demonstrated a significant increase in hardness and resulting ballistic performance with decreasing grain-size material. Material with an average grain size of $<1 \mu\text{m}$ exhibits an increase in hardness of about 70% and an increase in ballistic performance of about 30%.³

¹Krell, A.; Bales, A. Grain Size Dependent Hardness of Transparent Magnesium Aluminate Spinel, *Int. J. Adv. Comp. Tech.* **2010**, 8 (5), 1108–1114.

²Krell, A.; Hutzler, T.; Klimke, J. Advanced Spinel and Sub-micron Al_2O_3 for Transparent Armor Applications. *J. Europ. Ceram. Soc.* **2009**, 29, 275–281.

³Krell, A.; Strassburger, E. High Purity Submicron α - Al_2O_3 Armor Ceramics: Design, Manufacture and Ballistic Performance. *Ceram. Trans.* **2001**, 134 (1–2), 463–471.

2. Approach

The evaluation phase included systematic microstructural characterization of the material, quasi-static, and dynamic mechanical property measurements and nondestructive evaluation, followed by a ballistic evaluation. In addition, an analysis of the fragmentation of the spinel materials during projectile impact and penetration was carried out using a newly developed method at the Fraunhofer Institute for High-Speed Dynamics, Ernst-Mach-Institute (EMI). The fragments were collected from the target chamber and the size distribution was determined by means of a chain of sieves. The projectile penetration and the ceramic particles ejected from the crater were observed with two different high-speed cameras, and a laser light-sheet technique was used to analyze the ejected fragment size as a function of time. Krell speculated that fragment size in the rubble has significant influence on projectile penetration, with larger fragments slowing down penetration more than smaller ones.⁴

This investigation focused on developing a materials characteristics and mechanical and ballistic properties database of transparent polycrystalline spinel materials produced by IKTS. In addition, the spatial microstructural and defect distribution homogeneity of the two sets of materials were evaluated by newly developed ultrasonic nondestructive evaluation techniques and physical sectioning of the plates for density and mechanical property measurements. The extensive characterization efforts were conducted by several researchers in several organizations listed in table 1.

Table 1. List of characterization techniques utilized to evaluate the IKTS spinel.

Characterization Techniques	Researchers	Organization
Hardness load curves	Jeffrey Swab, Corydon Hilton	ARL
Quasi-static Hertzian indentation	Andrea Muller David Green	Penn State University
Spatial quasi-static mechanical properties and density	V. Domnich, D. Slusark, Rich Haber	Rutgers University
Nondestructive evaluation characterization	S. Bottigieri Andrew Portune, Rich Haber	ARL Rutgers University
Microstructure analysis	Buyang Cao	The Johns Hopkins University
Dynamic mechanical properties	Jamie Kimberly, K. T. Ramesh	The Johns Hopkins University
Ballistic fragmentation analysis	Elmar Strassburger, Parimal Patel, James McCauley	EMI
Ballistic performance	Parimal Patel	ARL

⁴Krell, A.; Strassburger, E. Hierarchy of Key Influences on the Ballistic Strength of Opaque and Transparent Armor, Advances in Ceramic Armor III. *Ceram. Eng. and Sci. Proc.* **2008**, 28 (5), 45–55.

3. Samples

1. Domestic spinel suppliers: There are several domestic manufacturers developing large-area spinel plates, including Technology Assessment and Transfer (TAT), CoorsTek, and BAE Advanced Ceramics. ARL has programs to evaluate the ballistic efficiencies of all of these materials. There is a manufacture-dependent variation in microstructure. For example, the microstructure of spinel produced by TAT has an average grain size upward of 300–500 μm in a bimodal distribution. This program analyzed 0.6- and 1.6- μm -grain spinel material to determine the properties of two fine-grain spinel materials.
2. IKTS spinel materials: IKTS has developed a processing methodology enabling the production of fine-grained material down to the nanostructure scale. For this program, they delivered two distinct sets of spinel plates with a nominal average grain size of 0.6 μm (205 series) and 1.6 μm (200 series). Forty parts were supplied that were nominally $100 \times 100 \times 6 \text{ mm}$; 36 plates were in the ground state and 4 were polished to transparency. The ground plates were polished by Nutek (Aberdeen, MD) to an 80/50 scratch/dig finish. The thickness was reduced by the polishing process to a 5.72–5.75-mm nominal thickness. The parts were all polished at the same time to reduce the variability in the surface quality.
 - Nomenclature:
 - (U) Series 200 \approx 1.5–2.0 μm (nominal 1.6 μm) average grain size
 - (U) Series 205 \approx 0.6 μm (600 nm) average grain size

4. Results

4.1 General Characterization

As shown in the macrophotographs in figures 1 and 2, the clarity of the 0.6- μm plate in plane light is qualitatively superior to the 1.6- μm material. Spinel is a cubic material, which means that it is optically isotropic, exhibiting no birefringence. In crossed polarized light, cubic materials will appear completely dark unless there are significant birefringent inclusions or defects or they have retained residual stress from the processing. It can be seen in both materials that there is a faint clover-like region indicative of residual stress. In the 1.6- μm material, the presence of yellowish spots suggests birefringent inclusions or defect clusters. In addition, it can be seen in both plane and polarized light that there are many smaller spots in the 200-series material compared with the 205-series material.

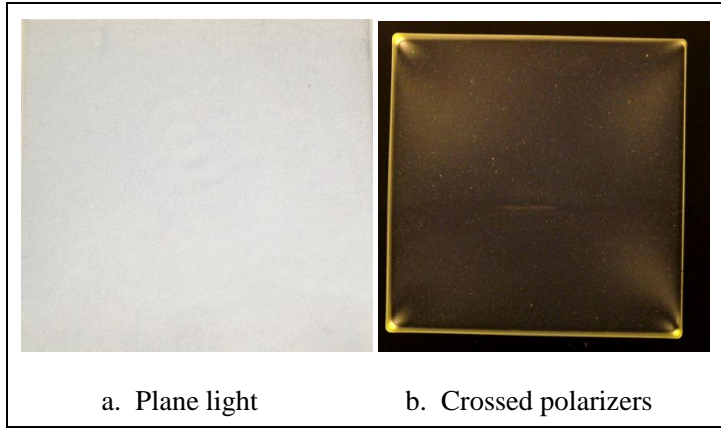


Figure 1. The 0.6- μm spinel (205 series).

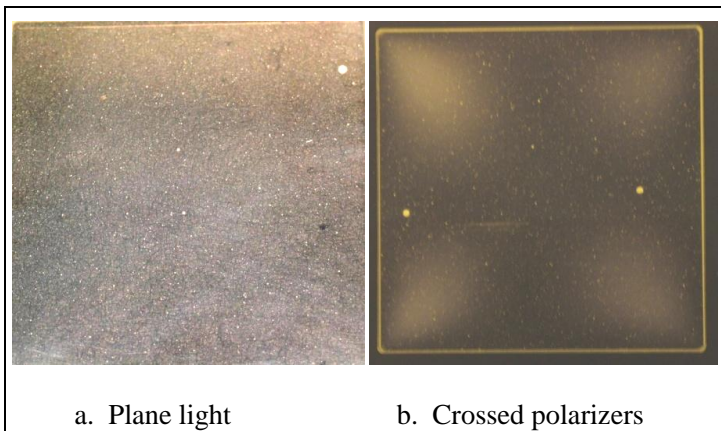


Figure 2. The 1.6–2.0- μm spinel (200 series).

4.2 Microstructures

It also can be seen in figure 3 that the 205-series material's microstructure is qualitatively more uniform than the 200-series material, which had grain sizes predominantly below 1.0 μm but also some bimodal characteristics of grains larger than 1.0 μm . Etching of the 200-series material proved to be more difficult, but it is clear that the microstructure is clearly much more bimodal than the 205 series, with more grains greater than 1.0 μm . This will be dealt with more quantitatively in section 4.5.

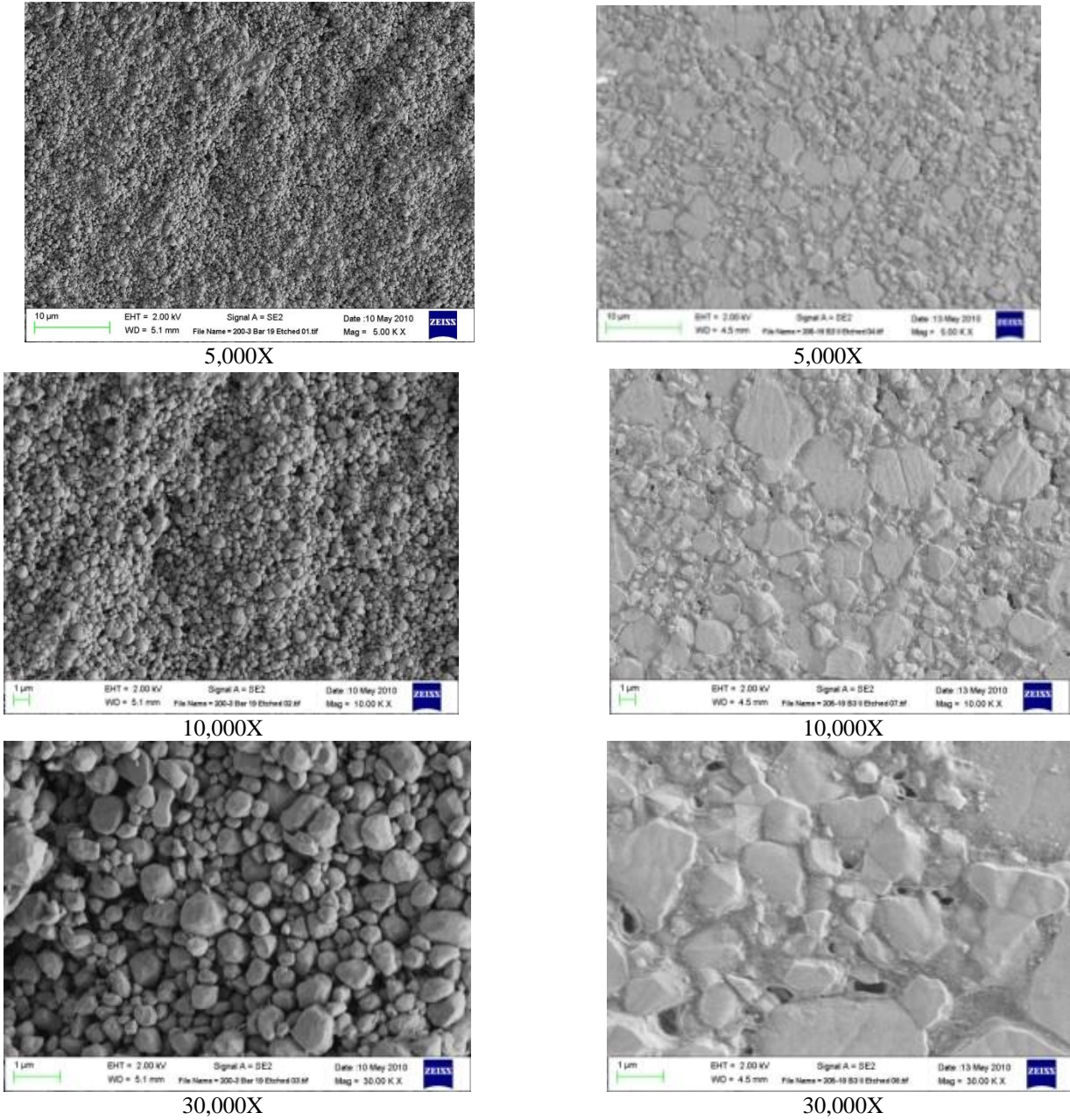


Figure 3. Various magnification SEM images of spinels etched in boiling phosphoric acid: left column, sample 205 (0.6 μm); right column, sample 200 (1.6 μm).

4.3 Advanced Nondestructive Ultrasound Characterization

S. Bottiglieri, A. R. Portune, and R. A. Haber – Rutgers University, Piscataway, NJ

4.3.1 Introduction

Magnesium aluminate spinel (MgAl_2O_4) is a leading candidate for lightweight transparent armor due to its superior optical and mechanical properties (1–3). Spinel has been developed since the early 1960s to enhance its intrinsic transparency and strength through advanced processing techniques and control of powder purity (4, 5). With average pore sizes under 50 nm, this material has shown transparency from the ultraviolet to the mid-infrared (IR) in the 0.2–5.5- μm range (2). Hot pressing and controlled heat treatments can achieve exceptionally fine microstructures with mean grain size as low as 0.6 μm . Novel processing methods such as spark plasma sintering are also being investigated to achieve the best mechanical strength and hardness without sacrificing optical transparency (6).

(U) Sintering additives are added to spinel to control kinetic processes during formation of the material and to reduce undesirable impurities. The most common additive used to achieve low heterogeneity concentration is lithium fluoride (LiF) (3). Adding 1.0-weight-percent LiF enhances late-stage sintering of spinel through the formation of oxygen vacancies (3). This additive also promotes the coalescence of pores into cylindrical cavities that sit along the grain boundaries, where they are less detrimental to optical transparency (2). However, the precipitation or clustering of sintering additives can cause spinel to appear hazy or foggy instead of transparent (5). The compositional homogeneity of this material is critical to achieving its superior optical and mechanical properties.

Nondestructive evaluation characterization of microstructural uniformity can be undertaken using ultrasound techniques (7). Ultrasound introduces oscillating elastic waves into the material that interact with microstructural features as they propagate. Measurements of the amplitude and time of flight (TOF) of reflected signal peaks can be used to calculate volumetric properties of the material over large sample areas (8). Elastic properties such as Young's modulus and the longitudinal speed of sound are determined from TOF measurements of longitudinal and shear wave reflections. Attenuation of acoustic energy is determined from the reduction in peak amplitude for successive back surface reflections. Previous studies have shown attenuation measurements to be more sensitive to minute changes in composition compared with elastic property measurements (9). Acoustic spectroscopy, the measurement of the frequency dependency of the attenuation coefficient, has been shown to correlate with minute microstructural variations in solid materials (10).

4.3.2 Acoustic Spectroscopy Theory

Acoustic spectroscopy has been used to correlate ultrasound results with microstructural features since early testing of metals was conducted in the 1950s (11). By performing a fast Fourier transform (FFT) on back surface reflections, it is possible to measure the strength of individual frequencies in each signal. The Beer-Lambert law is then used to calculate the attenuation coefficient at each frequency, using the first bottom surface reflection as the initial intensity and the second bottom surface reflection as the intensity after propagation. This law is stated as:

$$I = I_o e^{-\alpha x}, \quad (1)$$

where I is the transmitted intensity, α is the attenuation coefficient, I_o is the initial intensity, and x is the path length. If testing is performed in pulse-echo configuration, the path length is defined as twice the thickness of the sample. Figure 4 illustrates an oscilloscope view of labeled peak reflections showing the width of the time window used when performing the FFT on reflected signals. Note that the waveform in figure 4 is meant for instructive purposes only, and does not represent peak reflections from the spinel samples examined in this study.

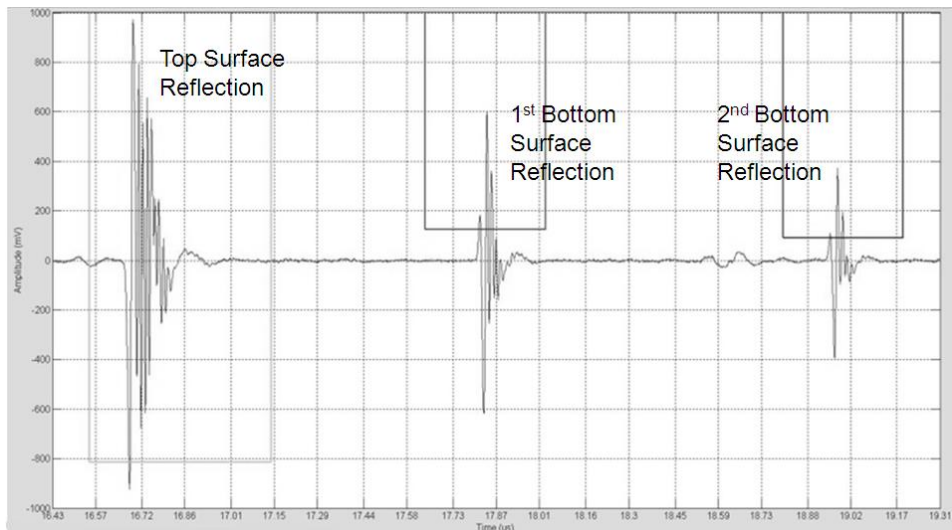


Figure 4. An oscilloscope view illustrating top and bottom surface reflections. The gates surrounding the bottom surface reflections correlate with the window used to perform the FFT on the reflected signal.

The attenuation coefficient measures the loss resulting from interactions with the bulk microstructure. Two mechanisms are responsible for energy loss in propagating waves—scattering and absorption. Scattering follows either Rayleigh or stochastic laws, depending on the relationship between the size of the scatterer and the acoustic wavelength. For fine-grained spinel, acoustic frequencies in excess of 100 MHz would be necessary to render the Rayleigh approximation inadequate. Scattering in the Rayleigh range can be expressed as follows (12):

$$\alpha_{Grain\ Scattering} = A D^3 f^4, \quad (2)$$

where A is a constant, D is the grain diameter, and f is the ultrasound frequency. Significant changes in mean grain size throughout a sample area will result in large attenuation coefficient variations due to the cubic dependency on grain diameter.

Absorption of ultrasonic energy occurs from multiple sources, some intrinsic to the material and some reliant on the presence of heterogeneous phases. Intrinsic absorption occurs as a fraction of the ordered particle motion in the acoustic wave converts to disordered motion, or heat (13). Extrinsic absorption has been best described in colloidal systems, which are analogous to heterogeneous solid materials. Thermoelastic absorption occurs at thermal or elastic property interfaces as a result of field continuity (14). Work in colloids has shown absorption phenomenon to dominate attenuation at lower frequencies, where contributions from scattering are roughly negligible (15). Absorption curves can be modeled as roughly Gaussian, whose behavior is defined as

$$A e^{-\frac{(x-B)^2}{2C}}, \quad (3)$$

where A defines the amplitude of the curve, B defines the central position, and C defines the full width at half maximum. These can be correlated with the size distribution and concentration of heterogeneities within the bulk microstructure. If analogous to colloids, the A parameter would relate to the concentration of heterogeneities, the B parameter would relate to the mean size of the heterogeneity as well as its thermal and elastic mismatch with the bulk material, and the C parameter would relate to the width of the size distribution of heterogeneities within the volume of the bulk that the acoustic wave interacted with (15).

4.3.3 Experimental Procedure

Two MgAl₂O₄ spinel samples with nominal 0.6- and 1.6-μm mean grain sizes were tested using advanced nondestructive ultrasound methods. The thickness of each spinel tile was measured to be ~6 mm by taking the average of 10 digital caliper readings. The mean grain size value for each sample was provided by the manufacturer. C-scan mapping using a 20-MHz central frequency planar transducer produced images of attenuation coefficient variations throughout the material. Figure 5 shows an FFT of the transducer output, demonstrating its -6-dB bandwidth to be 16–32 MHz. High signal strength suitable for acoustic spectroscopy is achieved in the 10–34-MHz range. C-scan maps found several large variations that correlated with visible yellow discolorations in the samples. These variations were further examined using acoustic spectroscopy in the 10–30-MHz range. Due to the grain size of the samples, acoustic

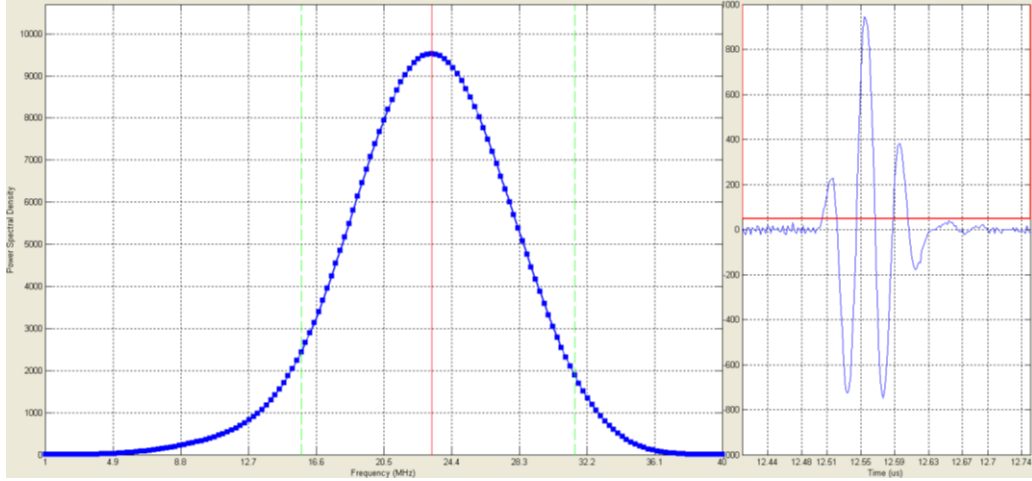


Figure 5. The signal output of the 20-MHz planar transducer used in this study. The FFT taken was of the top surface reflection of a polished silicon carbide mirror.

spectroscopy results would be entirely in the absorption regime. Attenuation coefficient spectra were curve fit to a single Gaussian to determine the A , B , and C parameters of the curve. Analysis of variations within these parameters indicated relative changes in the concentration, mean size, and size distributions of precipitates within the spinel microstructure.

4.3.4 Results

A C-scan map of the overall signal attenuation coefficient for the 1.6- μm -grain spinel sample is shown in figure 6. While most of the material displayed homogeneous results, several circular regions were seen with significantly higher attenuation coefficients. Three of these were more closely examined using acoustic spectroscopy, noted by numbers 1–3 in figure 6. Region 1 centers on a large deviation from the mean behavior; region 2 centers on a small deviation from mean; and region 3 represents the mean acoustic response of the material.

Acoustic spectroscopy results for the three chosen regions of the 1.6- μm -grain size spinel are shown in figure 7. The approximately Gaussian shape of the measured curves confirms that the dominating attenuation mechanism in the frequency range examined is absorption. The results of curve fitting a single Gaussian to each attenuation coefficient spectra can be seen visually in figure 7 as the dashed lines. Table 2 contains statistical information on the A , B , C , and R^2 values for each curve. A single Gaussian fits these attenuation coefficient spectra quite well, with the lowest R^2 value greater than 0.94. Analyzing changes in the Gaussian coefficients provides insight into changes in the microstructural homogeneity between different regions of the material.

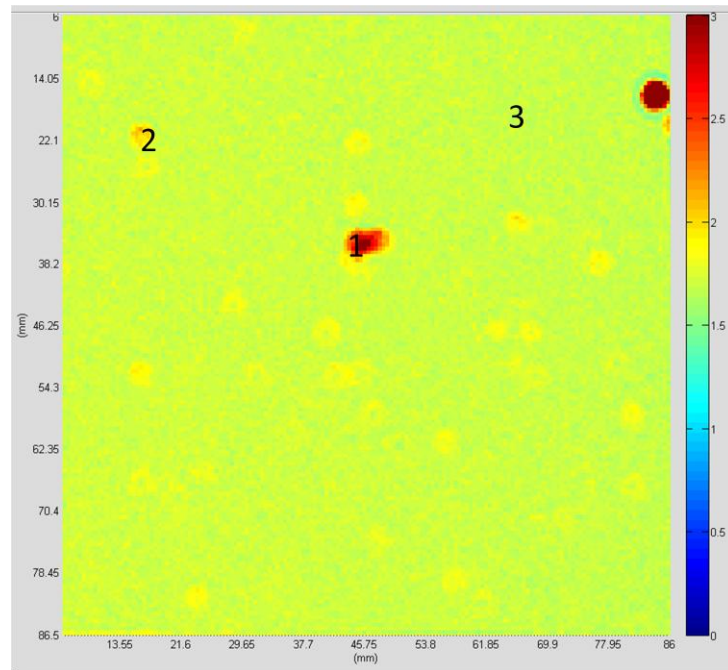


Figure 6. The C-scan map of overall signal attenuation coefficient measured using a 20-MHz transducer on the spinel sample with 1.6- μm mean grain size. The scale used is in units of dB/cm.

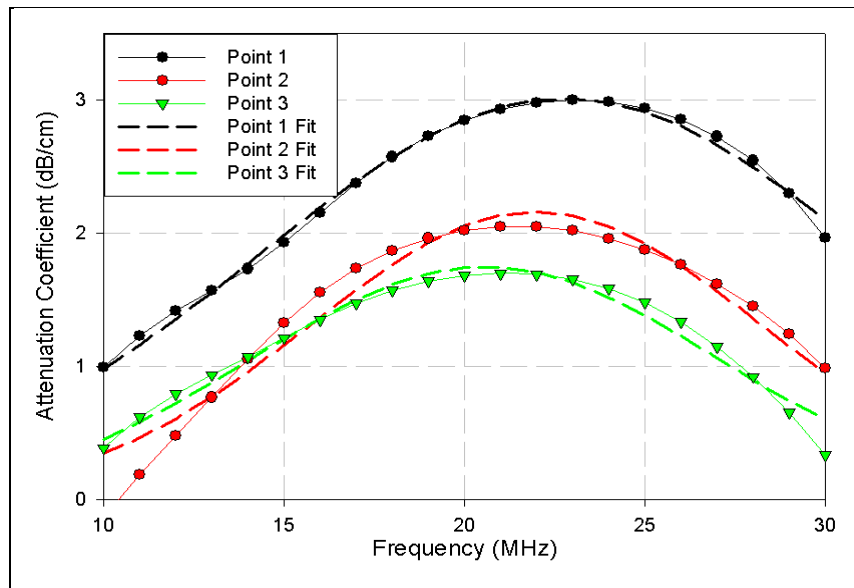


Figure 7. Acoustic spectroscopy results for three regions in the 1.6- μm -grain spinel with single Gaussian curve fitting.

Table 2. Curve fitting parameters for attenuation coefficient spectra from the 1.6- μm -grain spinel.

Value	Point 1	Point 2	Point 3
A	3.010	2.163	1.751
B	22.78	21.97	20.56
C	12.05	8.835	9.099
R^2	0.9945	0.9412	0.9651

Regions 1 and 2 show a significantly higher A coefficient relative to region 3, which is used as a baseline for the average microstructure. This indicates that the concentration of heterogeneities such as precipitates is increased in these regions. The B coefficient for region 1 has been shifted toward higher frequencies, indicating that the mean size of heterogeneities is likely smaller compared with the average microstructure. However, the C coefficient for this region is also significantly higher, which could indicate a wider sized distribution of heterogeneities present within the bulk microstructure at this location. Similar behavior is seen for region 2, although to a lesser extent. Acoustic spectroscopy results suggest that the regions of higher attenuation seen in figure 7 are, therefore, due to a clustering of smaller heterogeneities rather than from large anomalous inclusions.

A C-scan map of the overall signal attenuation coefficient for the 0.6- μm -grain spinel sample is shown in figure 8. Three regions were chosen for this material for more detailed analysis using acoustic spectroscopy, denoted by numbers 1–3 in figure 8. This material displayed far greater homogeneity in acoustic response relative to the 1.6- μm -grain material. Only one high attenuation region was located, denoted as region 1. A second region, which was slightly higher than the mean response, was chosen as region 2. Region 3 represents the mean microstructure of the material, and can be viewed as a baseline for comparing results. Note that a slightly wider scale is used in figure 9 relative to figure 7. This accounts for the higher attenuation coefficient values seen in region 1, due to the large and visible precipitate located there.

Acoustic spectroscopy results for the three chosen regions of the 0.6- μm -grain spinel are shown in figure 9. Like the 1.6- μm -grain spinel, attenuation spectra from this material are approximately Gaussian in shape. The results of curve fitting a single Gaussian to each attenuation coefficient spectra can be seen in figure 9 as the dashed lines. Table 3 contains statistical information on the A, B, C, and R^2 values for each curve. These curve fits produce R^2 values greater than 0.97, indicating that a single Gaussian is an appropriate choice for describing curve behavior. An analysis of changes in the Gaussian parameters provides insight into microstructural changes between regions of this material. The vertical scale used in figure 9 is wider than that used for the previous sample in figure 7 to account for the higher attenuation coefficient values measured.

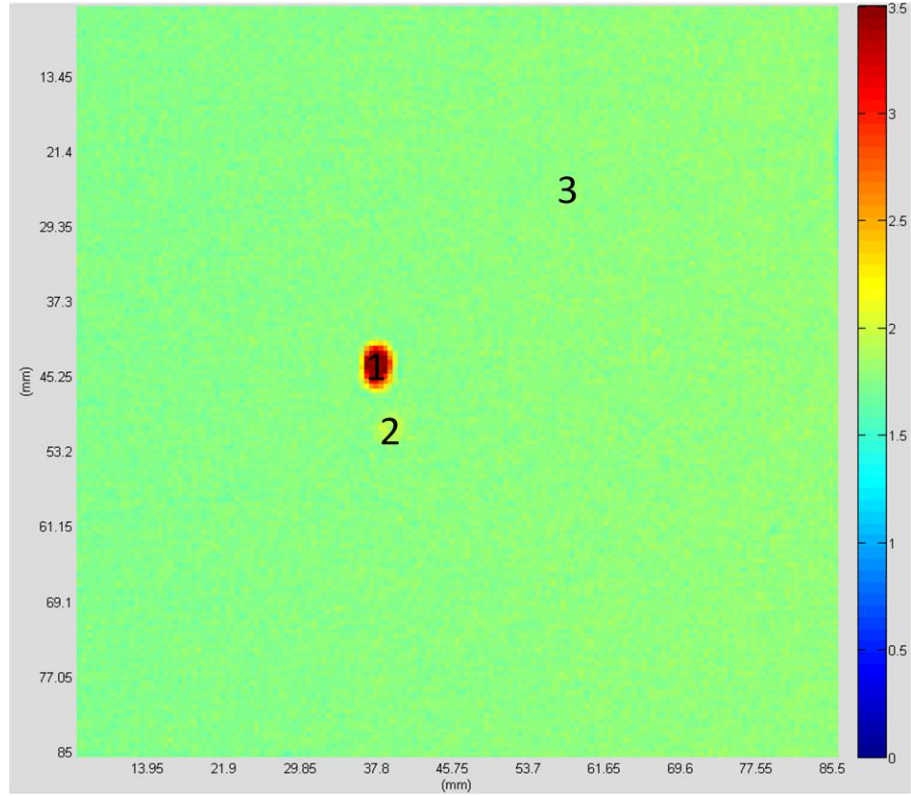


Figure 8. The C-scan map of overall signal attenuation coefficient measured using a 20-MHz transducer on the spinel sample with 0.6- μm mean grain size. The scale used is in units of dB/cm.

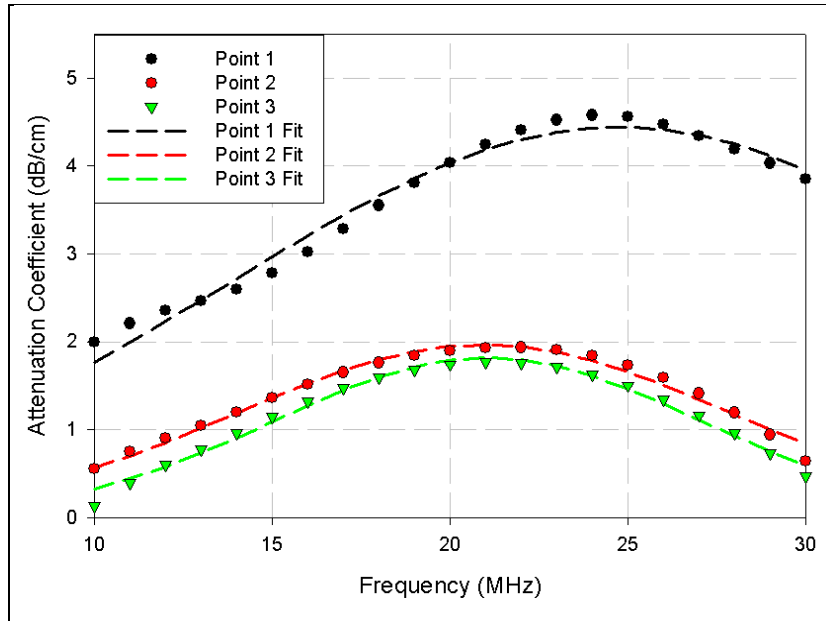


Figure 9. The attenuation coefficient spectra from the 0.6- μm -grain spinel with single Gaussian curve fitting.

Table 3. Curve fitting parameters for attenuation coefficient spectra from the 0.6- μm -grain spinel.

Value	Point 1	Point 2	Point 3
A	4.446	1.968	1.820
B	24.76	20.95	21.05
C	15.30	9.802	8.458
R ²	0.9786	0.9814	0.9841

Region 1 shows a significant increase in the A parameter relative to the other two regions of this material, indicating a marked rise in the concentration of heterogeneities present within this part of the microstructure. The B parameter shows a shift towards higher frequencies relative to the other two regions, indicating that the mean size of heterogeneities is likely smaller relative to the mean microstructure of the material. The C parameter for region 1 is almost double that of other regions, indicating that the width of the size distribution of heterogeneities is also increased for this part of the material. Region 2 shows very similar behavior to the baseline region 3 except for a small increase in the A parameter. This indicates a minor increase in the concentration of heterogeneities present within the bulk without a significant change in their mean size or size distribution.

A study was also conducted on a transparent spinel tile with 1.6- μm mean grain diameter that showed visible yellow inclusions throughout the material. The manufacturer reported that microscopy showed these inclusions to be clusters of submicron sintering additives that precipitated during heat treatment. The most common sintering additive in transparent polycrystalline spinel is LiF.

Acoustic spectroscopy was performed over the region of the sample, which showed strong visible inclusions. The resulting attenuation coefficient spectrum is shown in figure 10. The spectrum shows a single absorption peak centered at 23 MHz. By using the physical properties of LiF and using 23 MHz as f_0 , it is possible to calculate the mean particle diameter using the modified equation:

$$a = \sqrt{\frac{\pi D}{2 \rho f_0}}.$$

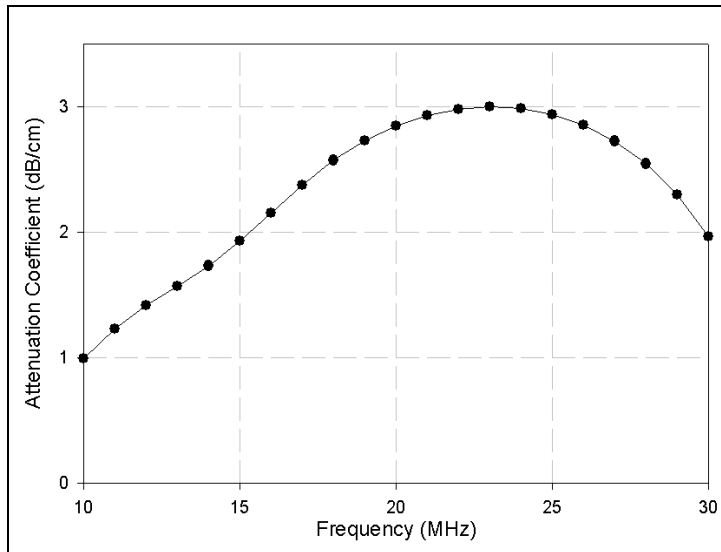


Figure 10. Attenuation coefficient spectrum of polycrystalline spinel over region showing visible yellow inclusion.

This yields a mean particle diameter of $0.45\text{ }\mu\text{m}$ for LiF inclusions. Particles of this size would cause preferential scattering of green and blue light, causing the inclusions to look visibly yellow. The estimated size also closely matches that reported by the manufacturer as measured through microscopy.

Figure 11 illustrates the overall signal attenuations of both series of spinel materials. It is clear that the $0.6\text{-}\mu\text{m}$ materials are more homogeneous than the $1.06\text{-}\mu\text{m}$ materials, but exhibit a little more average overall attenuation, as shown in the acoustic spectroscopy spectra in figure 12.

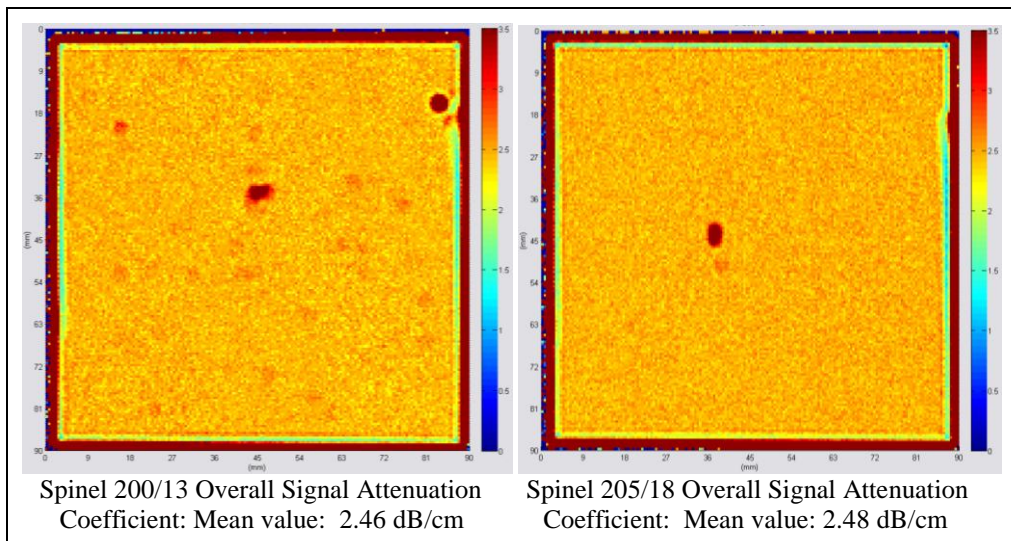


Figure 11. Overall signal attenuations of 200- and 205-series spinel samples.

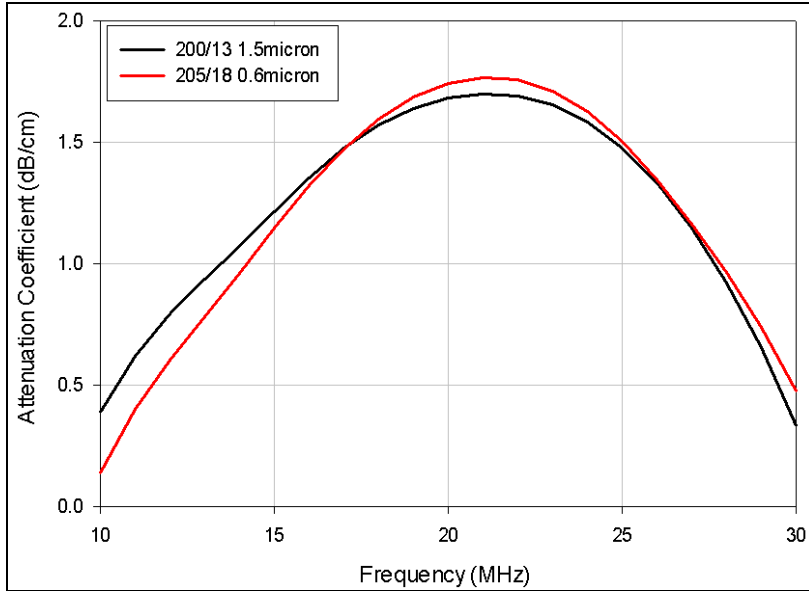


Figure 12. Attenuation coefficient spectra comparison between spinel samples after correction factors have been taken to account for reflective and diffractive losses.

4.3.5 Conclusions

The Gaussian nature of frequency-dependent attenuation coefficient measurements confirms that absorption is the dominating loss mechanism in both samples. This is not surprising since the average grain size is two orders of magnitude smaller than the acoustic wavelength in the 10–30-MHz range. Acoustic spectroscopy results from both materials show that clustering of small heterogeneities is typically the cause of high attenuation coefficient regions seen in C-scan maps. Fewer clusters were seen in the 0.6- μm -grain spinel than to the 1.6- μm sample. As the magnitude of attenuation ranks with the concentration of bulk features, it is likely that the cluster seen in the 0.6- μm -grain spinel contained a higher concentration of precipitates compared with features seen in the 1.6- μm material.

While acoustic spectroscopy can measure changes in the relative concentration and size distribution of these features, it is unable to make specific quantitative predictions at this time. Due to the nature of the experimental process, this technique is suitable only for materials with relatively smooth and parallel surfaces. Roughness becomes increasingly deleterious to attenuation coefficient measurements as frequency increases. Acoustic spectroscopy is applicable to all ceramic materials, whether single crystal or polycrystalline. As active loss mechanisms will vary from one material to the next, accurate interpretation of spectra results requires some a priori knowledge of the system under interrogation.

Advanced ultrasound characterization techniques have been demonstrated to be successful in rapidly identifying microstructural variations within transparent armor ceramics. Comparing acoustic spectroscopy results from multiple sample regions allows us to understand how the concentration and size distribution of heterogeneities within the bulk microstructure varies within the material. Gaussian curve fitting supplies three coefficients that correlate with changes in the size distribution and concentrations of heterogeneities within the bulk microstructure. A thorough study incorporating mechanical sectioning and imaging could provide more specific predictions about these microstructural factors. Since clusters of elastic heterogeneities could potentially reduce the mechanical and optical properties of transparent armor ceramics, determining the location and concentration of these microstructural features is crucial to accurate predictions of material performance in its application.

References

1. Fountzoulas, C. G.; Sands, J. M.; Gilde, G. A.; Patel, P. J. Modeling of Defects in Transparent Ceramics for Improving Armor. *Proceedings of the 24th International Symposium on Ballistics*, New Orleans, LA, 22–26 September 2008; National Defense Industrial Association: Arlington, VA.; Vol. 2, pp 760–767.
2. Riemanis, I. E.; Kleebe, H.; Cook, R.; DiGiovanni, A. Transparent Spinel Fabricated From Novel Powders: Synthesis, Microstructure, and Optical Properties. Presented at the 10th DOD Electromagnetic Windows Symposium, Norfolk, VA, 19 May 2004.
3. Rozenburg, K.; Riemanis, I.; Kleebe, H.; Cook, R. Sintering Kinetics of a MgAl₂O₄ Spinel Doped with LiF. *J. Am. Ceram. Soc.* **2008**, *91* (2), 444–450.
4. Palmour, H. *Development of Polycrystalline Spinel for Transparent Armor Applications*; Final Technical Report; U.S. Army Materials and Mechanics Research Center: Watertown, MA, 1972.
5. Cook, R.; Kochis, M.; Riemanis, I.; Kleebe, H. A New Powder Production Route for Transparent Spinel Windows: Powder Synthesis and Window Properties. *Proceedings of the SPIE Defense and Security Symposium 2005*, 28 March–1 April 2005; International Society for Optical Engineering: Bellingham, Washington, June 2005; Vol. 5786, pp 41–47.
6. Frage, N.; Cohen, S.; Meir, S.; Kalabukhov, S.; Dariel, M. P. Spark Plasma Sintering (SPS) of Transparent Magnesium-Aluminate Spinel. *J. Mater. Sci.* **2007**, *42*, 3273–3275.
7. Brennan, R. Ultrasonic Nondestructive Evaluation of Armor Ceramics. Thesis dissertation, Rutgers University, 2007.
8. Brennan, R.; Haber, R.; Niesz, D.; Sigel, G.; McCauley, J. Elastic Property Mapping Using Ultrasonic. *Ceram. Eng. and Sci. Proc.* **2008**, *28* (5), 213–222.
9. Bottiglieri, S.; Haber, R. High Frequency Ultrasound of Armor-Grade Alumina Ceramics. *Proceedings of the 35th Annual Review of Progress in Quantitative Nondestructive Evaluation*, Chicago, IL, 20–25 July 2008; American Institute of Physics: Melville, NY, 2009; Vol. 1096, pp 1301–1308.
10. Vary, A.; Kautz, H. Transfer Function Concept for Ultrasonic Characterization of Material Microstructures. *Materials Analysis by Ultrasonics – Metals, Ceramics, Composites*. Noyes Data Corporation: Park Ridge, NJ, 1987; 249–289.
11. Mason, W.; McSkimin, H. Attenuation and Scattering of High Frequency Sound Waves in Metals and Glasses. *The Journal of the Acoustical Society of America* **1947**, *19* (3), 464–473.

12. Nicoletti, D.; Bilgutay, N. B. Onaral. *Ultrasonics Symposium, 1990, Proceedings*, Honolulu, HI, 4–7 December 1997; IEEE: New York, NY; pp 1119–1122.
13. Luo, L.; Molnar, J. Ultrasound Absorption and Entropy Production in Biological Tissue: A Novel Approach to Anticancer Therapy. *Diagnostic Pathology* **2006**, *1* (35).
14. Lucke, K. Ultrasonic Attenuation Caused by Thermoelastic Heat Flow. *J. of Appl. Phys.* **1956**, *27* (12), 1433–1438.
15. Dukhin, A.; Goetz, P. *Ultrasound for Characterizing Colloids – Particle Sizing, Zeta Potential Energy*; Elsevier Science B. V.: Amsterdam, Netherlands, 2002.

4.4 Quasi-Static Mechanical Properties and Raman Spectroscopy Characterization

V. Domnich and D. Slusark, Rutgers University, and J. Swab, ARL

4.4.1 Mechanical Properties and Density

Two spinel tile numbers, 205/18 (0.6 μm) and 200/3 (1.6 μm), from the Fraunhofer Institute for Ceramic Technologies and Systems (*Fraunhofer-Institut für Keramische Technologien und Systeme*, IKTS), were sectioned into modulus of rupture (MOR) and fracture toughness bars for mechanical testing. Fourteen B-type MOR bars^{*} and eight D-configuration chevron-notch (C-N)[†] bars were machined from each tile. The spatial position of each bar in relation to the original tile can be seen in figure 13. MOR bars 15, 16, 17, and 18 and C-N bars 4 and 5 were destroyed upon machining. The Archimedes density of each MOR bar was measured before fracture testing, the results of which can be seen in tables 4 and 5. For both tiles, the average bend-bar density was found to be 3.57 g/cm^3 , with a standard deviation of 0.01 g/cm^3 . The average MOR of the bars from tile 205/18 was found to be 258 MPa, with a standard deviation of 37 MPa. For the bend-bars from tile 200/3, the average MOR was 262 MPa, with a standard deviation of 35 MPa. The density of the C-N bars was not measured to avoid the risk of breaking the bars because of their fragile nature; six of the eight bars from tile 205/18 were broken during testing. The two surviving bars had measured K_{IC} values of 1.76 and 2.46 $\text{MPa}\cdot\text{m}^{1/2}$. One of the 200/3 bars was broken during testing; the remaining seven bars had an average K_{IC} value of 2.13 $\text{MPa}\cdot\text{m}^{1/2}$, with a standard deviation of 0.32 $\text{MPa}\cdot\text{m}^{1/2}$.

The Weibull plots from B-type MOR bars for these two series of spinel materials are shown in figure 14. The Weibull moduli for the 205 series is 8.72 and 8.15 for the 200 series, again suggesting that the 0.6- μm material is more uniform and less variable than the 1.6- μm material.

^{*} ASTM C-1161-94(1996). Standard Test Method for Flexural Strength in Ambient Temperatures **1996**.

[†] ASTM C-1421-99. Standard Test Method for Determination of Fracture Toughness of Advanced Ceramics at Ambient Temperatures **1999**.

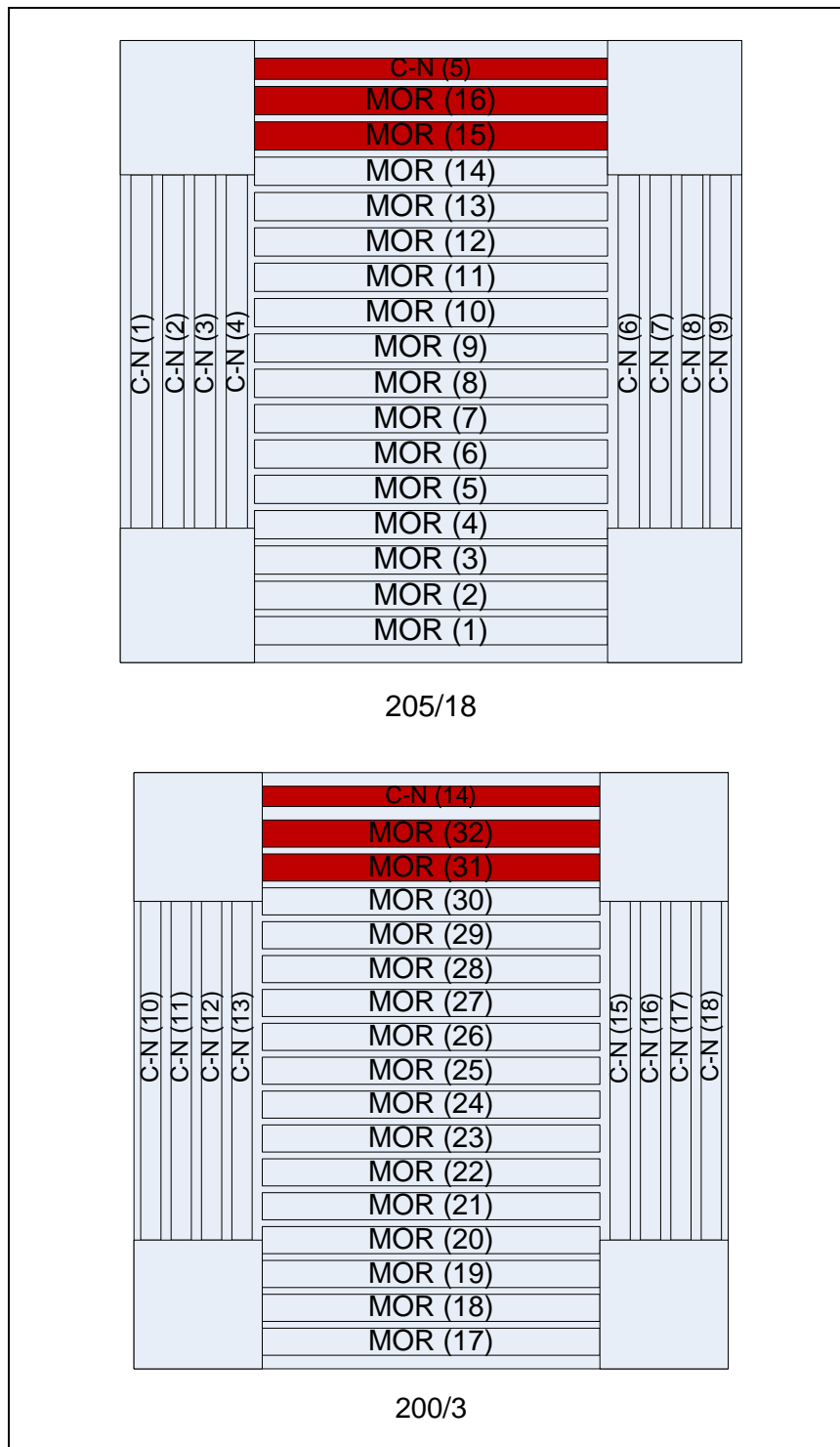


Figure 13. Spatial position of each MOR/C-N bar in relation to the original spinel tile.

Table 4. MOR and density.

Tile No.	205/18 Bulk Density (g/cm ³)	S _(4,40) (MPa)	Tile No.	200/3 Bulk Density (g/cm ³)	S _(4,40) (MPa)
1	3.57	262	17	3.56	284
2	3.57	308	18	3.58	272
3	3.57	268	19	3.57	256
4	3.58	282	20	3.55	186
5	3.58	266	21	3.55	242
6	3.58	319	22	3.57	249
7	3.57	209	23	3.56	217
8	3.58	275	24	3.58	287
9	3.59	241	25	3.58	277
10	3.56	208	26	3.57	233
11	3.56	203	27	3.57	303
12	3.57	239	28	3.58	315
13	3.57	299	29	3.58	275
14	3.56	238	30	3.57	278
Average	3.57	258	Average	3.57	262
Maximum	3.59	319	Maximum	3.58	315
Minimum	3.56	203	Minimum	3.55	186
Std. Dev.	0.01	37	Std. Dev.	0.01	35

Table 5. Fracture toughness.

Tile No.	205/18 K _{IC} (MPa·m ^{1/2})	Tile No.	SP 200/3 K _{IC} (MPa·m ^{1/2})
1	1.76	10	—
2	—	11	2.49
3	2.46	12	1.96
4	—	13	2.07
5	—	14	1.86
6	—	15	2.66
7	—	16	1.84
8	—	17	2.04
9	—	18	—
Average	2.11	Average	2.13

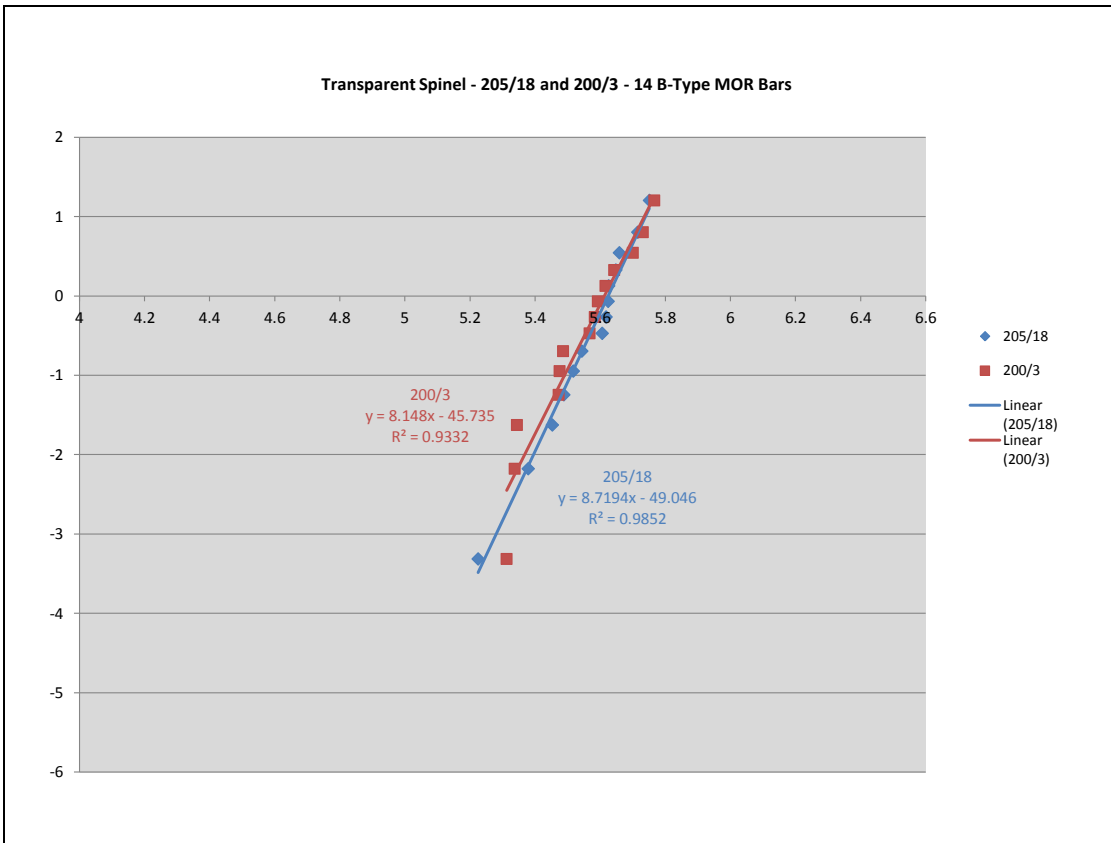


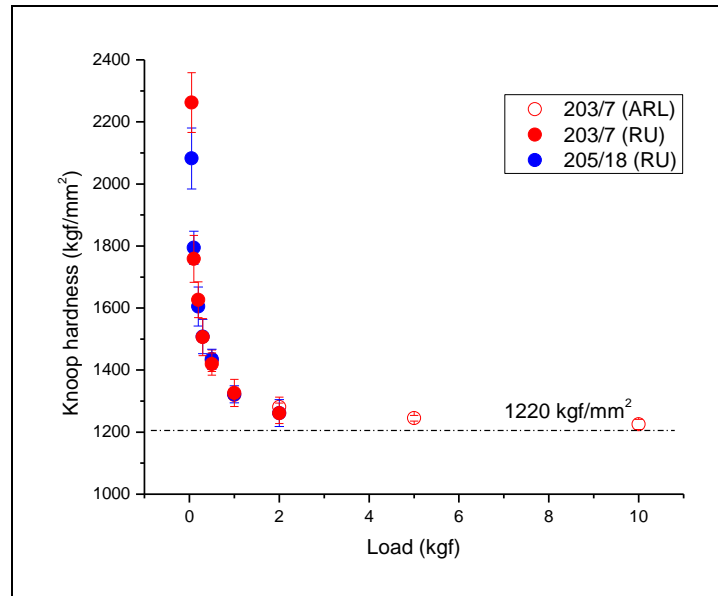
Figure 14. Weibull plots of two series of spinel materials.

4.4.2 Hardness Measurements

The hardness of spinels 205/18 and 200/3 was measured using Knoop (HK) and Vickers (HV) indentation methods. Five indentations at each of the applied loads of 0.05, 0.1, 0.2, 0.3, 0.5, 1, and 2 kgf (20 N) were produced on each sample. Figures 15 and 16 show Knoop and Vickers hardness of 205/18 vs. 200/3 samples. For the 200/3 sample, hardness data at higher loads provided by ARL is also included.

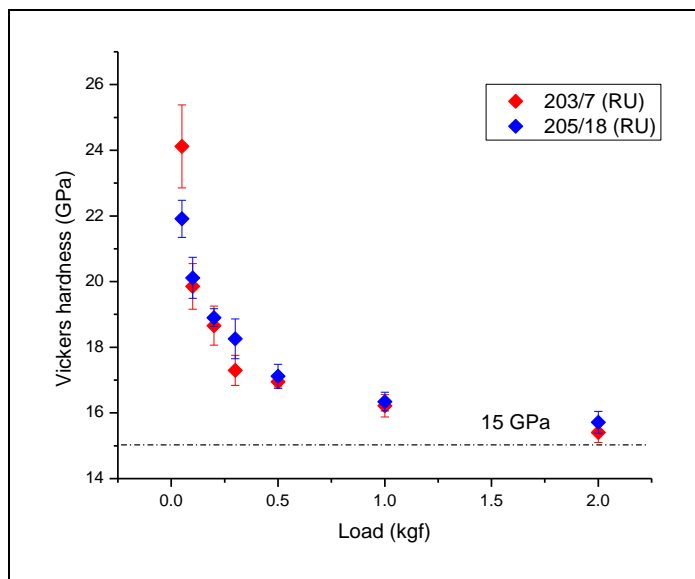
Both Vickers and Knoop hardness plots show an evident indentation size effect, with hardness values increasing toward lower applied loads. The stable hardness values (at loads >2 kgf) were measured as follows: HK = 1220 kgf/mm²; HV = 15 GPa. Only an insignificant difference in hardness between samples 200/3 and 205/18 was observed.

Knoop and Vickers hardness plots for samples 200/3 and 205/18 are shown in figures 17 and 18. HK was found to be lower than HV by about 3 GPa for each sample.



Note: 203 = 200.

Figure 15. Knoop hardness for spinel 200 and 205.



Note: 203 = 200.

Figure 16. Vickers hardness for spinel 200 and 205.

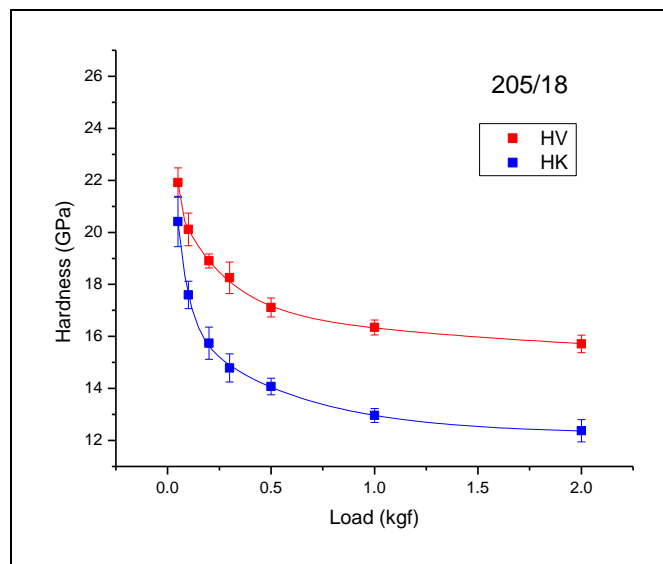


Figure 17. Knoop vs. Vickers hardness for spinel 205.

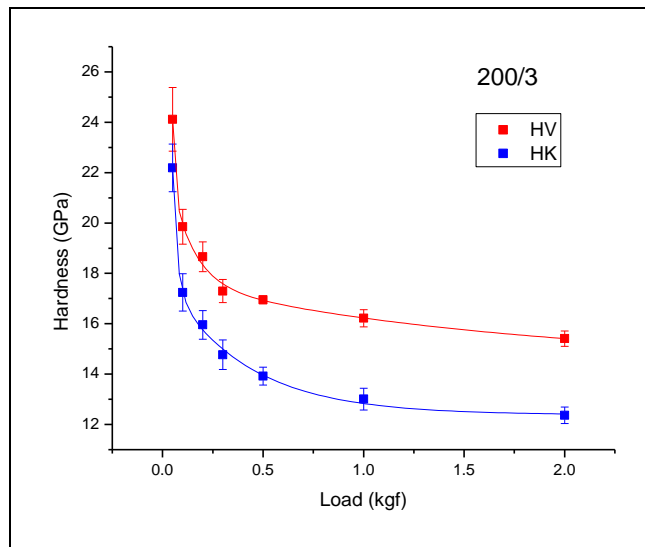


Figure 18. Knoop vs. Vickers hardness for spinel 200.

4.5 Bulk Plasticity and Transitional Velocity from Load/Hardness Curves

C. Hilton, J. Swab, and J. McCauley, ARL

In general, it has long been known that the hardness of ceramics correlates with gross impact performance; however, not to a degree useful for materials development. Wilkins et al. (1) were the first to point out the apparent importance of ceramic “plasticity” or inelastic deformation mechanisms in beryllium oxide (BeO) and aluminum nitride (AlN) in impact performance. More recently, Lundberg et al. (2) have made compelling arguments that the compressive yield strength (related to hardness) augmented by the amount of “plasticity” in ceramics correlates well to transitional velocities (dwell), i.e., the velocity (or impact pressure) where penetration begins.

However, a direct measure of plasticity has not been determined. Hardness comparisons between materials are problematic because the values vary with the applied load; however, the full hardness-load curve can provide much more information on material behavior than hardness alone measured at a single load. A plot of \log_{10} (Knoop hardness [HK]) vs. \log_{10} (force/indentation load [N]) yielded easily comparable straight lines, whose slope and intercept data might be useful parameters to characterize the materials. The absolute value of the reciprocal of the slope is a measure of plasticity, and the sum of this value and the calculated Knoop hardness at 1 N is a useful parameter to predict impact transitional velocity using the following equation (3):

$$(U) \text{ Trans. Vel.} = \text{HK}(1\text{N}) + [- (1/c)], \quad (1)$$

the results of which are shown in table 6.

Table 6. Bulk plasticity and predicted transitional velocities.

Material	Tester	Absolute Value of c From Power Equation	R ²	Plasticity M&W [- (1/c)]	HK ₁₀₀ (GPa)	T _v Calculated (m/s) - HK ₁₀₀
Krell Spinel – 200/7 (1.6 μm)	JS	0.0661	—	15.13	14.2	1277
	GS	0.0750	0.8969	13.33	15.8	1272
	CH	0.0840	0.9613	11.90	15.4	1219
Krell Spinel – 205/18 (0.6 μm)	DD	0.0523	—	19.11	14.8	1406
	GS	0.0730	0.9598	13.70	15.0	1259
	CH	0.0920	0.9780	10.87	16.0	1207

Notes: $[-(1/c)]$ = bulk plasticity.

HK₁₀₀ = Knoop hardness at 100 g.

T_v = predicted transitional velocity.

R² = correlation coefficient

M&W = McCauley and Wilantewicz (3)

4.5.1 Raman Spectroscopy Analysis

For Raman spectroscopy analysis, a Renishaw inVia instrument operating at a 633-nm wavelength was utilized. Spectra were collected using an x50 objective lens that allowed focusing the laser beam to a $\sim 2\text{-}\mu\text{m}$ spot on the sample surface. The spectra were collected at five different locations on each sample to ensure reproducibility of the results.

The typical Raman spectra of samples 200/3 and 205/18 are shown in figure 19. Using peak deconvolution procedures, seven major peaks were identified in the spectra. The peaks at 307, 408 (asymmetric), 670, and 768 cm^{-1} are characteristic to MgAl_2O_4 spinels, assigned in the literature to vibrations of such structural units as MgO_4 and AlO_4 tetrahedra (4). The peak at 710 cm^{-1} is typically not observed in perfectly crystalline natural spinels, and can be attributed to the presence of cationic disorder in the material (5). The origin of the broad peak at 575 cm^{-1} could not be readily identified. The perceived peak assignments and their respective symmetry indices are shown in figure 19.

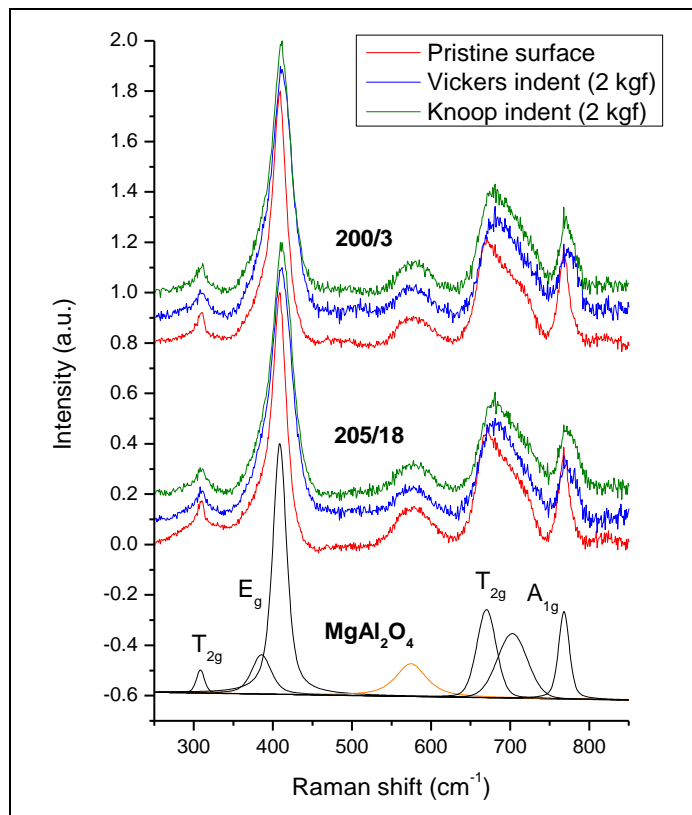


Figure 19. Raman spectra of spinel standard, 200/3 and 205/18.

To monitor structural changes in the material under indentation, Raman spectra were also collected from the inside areas of the residual Knoop and Vickers indents on both samples. Many materials exhibit phase transformations or amorphization under contact loading, such as indentation, which is revealed in the appearance of new peaks or broadening of the Raman spectra collected from the impacted areas (6). However, as illustrated in figure 19, both spinels under study (200/3 and 205/18) did not show signs of indentation-induced phase transformation/amorphization.

References

1. Wilkins, M. L.; Cline, C. F.; Honodel, C. A. *Light Armor*; UCRL-71817; Lawrence Radiation Laboratory, University of California: Livermore, CA, 1969.
2. Lundberg, P.; Renström, R.; Lundberg, B. Impact of Metallic Projectiles on Ceramic Targets – Transition Between Interface Defeat and Penetration. *International Journal of Impact Engineering* **2000**, *24*, 259–275.
3. McCauley, J. W.; Wilantewicz, T. E. *Using Plasticity Values Determined From Systematic Hardness Indentation Measurements for Predicting Dwell in Armor Ceramics: A New, Simple Screening Technique*; ARL-RP 268; U.S. Army Research Laboratory: Aberdeen Proving Ground, MD, 2009.
4. McMillan, S. P. F. Hofmeister A. M. In *Spectroscopic Methods in Mineralogy and Geology, Reviews in Mineralogy* **1988**, *18*, Hawthorne, F. C., Ed.; Mineralogical Society of America: Washington, DC; pp 99–159
5. Lazzeri, M.; Thibaudeau, P. Ab-initio Raman spectrum of the normal and disordered MgAl₂O₄ spinel. *Phys. Rev. B* **2006**, *74*, 140301(R).
6. Gogotsi, Y.; Domnick, V., Eds. *High Pressure Surface Science and Engineering*; Institute of Physics Publishing: Philadelphia, PA, 2004.

4.6 Elastic-Plastic Indentation Response of Transparent Polycrystalline Spinel

Andrea M. Muller and David J. Green, Pennsylvania State University

4.6.1 Introduction and Background

Indentation of a surface with a hard sphere, known as Hertzian indentation, can be used to examine the mechanical response of a wide range of materials. It is an extremely versatile tool, allowing investigation of both the elastic and inelastic regimes, and has been used extensively to characterize hardness, elastic modulus, and contact damage in brittle ceramics (1). For the special case of a frictionless elastic contact of a sphere with a flat surface, the projected contact area is circular with radius, a . That radius increases with increasing force as given by

$$a^3 = \frac{3PR}{4E^*}, \quad (1)$$

where P is the applied compressive force, R is the indenter radius, and E^* is the composite modulus given by

$$\frac{1}{E^*} = \frac{(1-v_s^2)}{E_s} + \frac{(1-v_I^2)}{E_I} = \frac{1}{E_{RS}} + \frac{1}{E_{RI}}, \quad (2)$$

where E is Young's modulus, v is Poisson's ratio, E_R is the reduced elastic modulus, and the subscripts I and S refer to the indenter and surface, respectively (2). This quasi-static indentation test is capable of producing loading conditions under the indenter resembling the early stages of a ballistic impact. Outside the contact area, the surface stresses are tensile, with the maximum tensile stress occurring immediately outside of the contact area. These tensile surface stresses are the driving force for the ring or cone-crack formation that can occur during indentation of brittle materials (3). The cracking morphologies observed during indentation show similarities to a ballistic impact site, particularly with the formation of cone-cracks at the contact site (4). Based on these observations, information gathered using this indentation technique could potentially be used to aid in the evaluation of ceramic armor materials.

Full-scale ballistic tests, such as V50 and depth-of-penetration, are ultimately the best evaluators of armor performance. These tests are, however, often too costly and time consuming to conduct on materials in the early stage of development due to small initial material size and limited availability. Previous attempts at linking the quasi-static and dynamic mechanical properties have been met with limited success because there is really no more than a basic understanding of exactly how (or which combinations of) material properties can account for ballistic behavior (5). This lack of understanding is mainly due to the complex behavior and failure of the various material systems during impact. Clearly, there is a need to develop an economical test methodology or analysis techniques that can be used to reliably correlate quasi-static laboratory-scale tests to dynamic ballistic behavior. Such a methodology or analysis technique

will aid in the development of new ceramic armor materials, the enhancement of models used to predict ballistic performance, and, ultimately, the final selection of ceramic armor materials.

The recent advent of nanoindentation has led to the introduction and use of continuous depth-sensing indentation to measure the mechanical properties of small volumes of material (6). The ability to capture both the loading and unloading response during indentation on a force–displacement curve and, consequently, the indentation contact area, has produced a new way of gathering data during the indentation process. Traditionally, indentation data has only been gathered after the load has been removed. While nanoindentation has allowed for the investigation of reduced modulus and hardness at low loads (<1 mN) and shallow depths, typically in the range of 10–500 nm, there is difficulty in relating nanoindentation data to ballistic behavior because the maximum indentation forces and sample volumes tested are very small compared to typical ballistic impact zones.

To overcome the size limitations of nanoindentation, an instrumented indentation system was built to extend the depth-sensing capability to the microscopic scale, as shown in figure 20. This system is capable of continuous force–displacement measurement, allowing for greater depths (>1 μ m) and larger volumes of material to be probed at forces up to 1 kN, and is equipped with an acoustic emission system to detect the onset of crack initiation (7). These features offer the possibility of studying not only the elastic and inelastic response, but also the fracture processes that occur at loads exceeding those associated with nanoindentation.

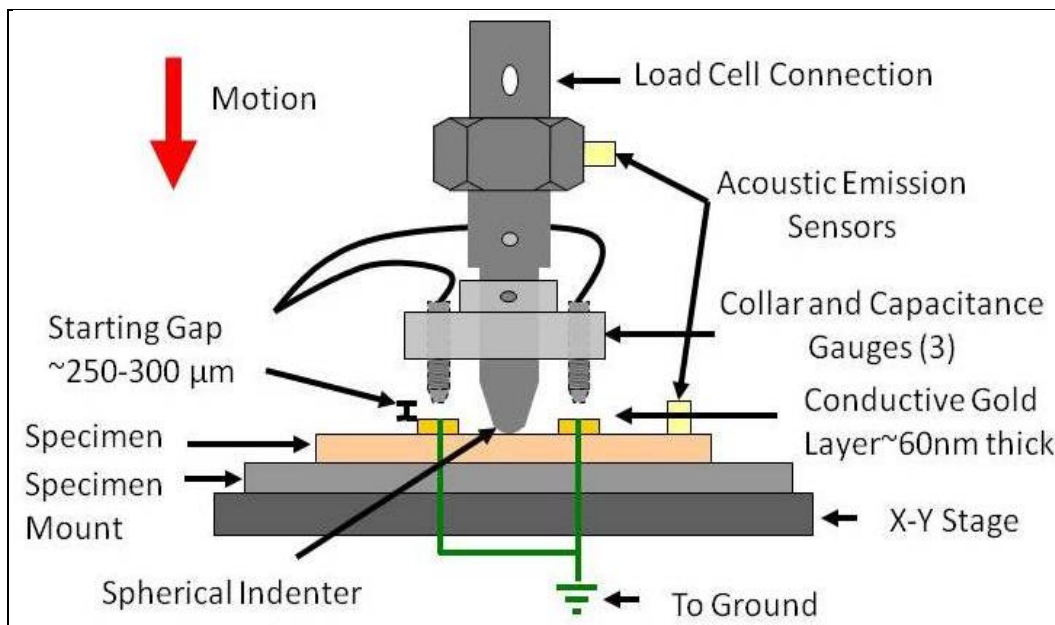


Figure 20. Schematic of the instrumented indentation test setup.

A second indentation system was constructed to examine the indentation process in transparent materials, as there is a renewed interest in transparent ceramics and glasses for armor applications. There is also the scientific advantage of being able to view the contact region using

optical microscopy. The direct contact area measurement indentation system, shown in figure 21, has a 2.2-kN load capacity and is controlled by a variable-rate stepping motor (7). This custom-built device, similar to that reported previously (8), is designed to measure the contact area between the sphere and the surface of the transparent material throughout the loading and unloading cycle using an inverted optical microscope. This equipment also allows the fracture loads and cracking sequence to be studied in-situ.

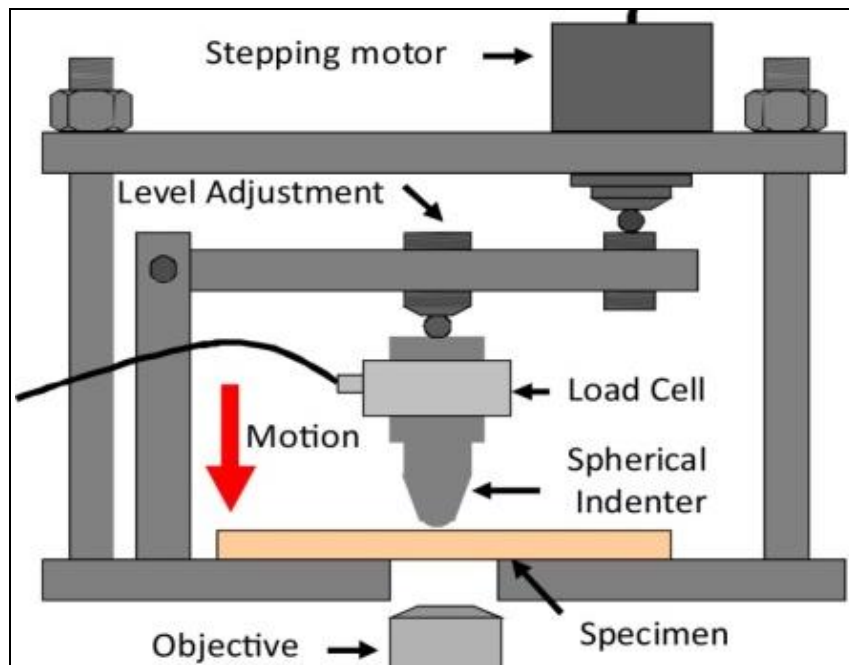


Figure 21. Schematic of the direct contact area measurement test system.

One noteworthy aspect of instrumented spherical indentation is that by varying the indenter radius, situations can be studied in which elastic or inelastic deformation occurs prior to fracture. As the indenter size decreases, there is a critical load below which inelastic deformation occurs prior to fracture (9). Thus, the indenter radius can be selected to either promote or prevent yielding prior to fracture. Yielding may also take place after fracture has been initiated, if loading is continued, due to increasing contact stresses.

The failure process in ballistic impact of armor ceramics entails the production of an inelastic zone that expands and stresses the surrounding elastic material below the impact site as penetration into the surface proceeds (10). The deformation mechanisms involved in the formation of this zone are also not very well understood (11). Consequently, the transitions and interactions among the elastic zone, inelastic deformation zone, and the fracture zone are of great interest. Use of a spherical indenter would allow the elastic–inelastic transition to be evaluated. Furthermore, it would allow the influences of elastic recovery to be studied.

Major challenges exist in making the link between tests performed at low strain rates and those of dynamic ballistic impacts. One such challenge is in relating the information obtained from traditional hardness tests. Hardness is, in general, thought to play a role in governing ballistic performance because it represents a resistance to penetration and plays a role in penetrator fragmentation and erosion. Simply making comparisons between traditional hardness tests can be quite difficult because the deformation and fracture processes vary due to geometrical differences between the various indenter tips. Further complications arise due to a phenomenon known as indentation size effect (ISE), which is described as a change in hardness with increasing indentation load. This leads one to question whether a force–hardness function or single hardness value is more representative, since hardness often varies significantly at low loads yet appears to approach a single value at higher indentation loads (12–14). Fracture, especially at higher indentation loads, can make interpretation of the indentation behavior difficult.

There are several theories about why ISE occurs in brittle materials. One suggests that ISE is related to the ratio of elastic to inelastic deformation during indentation and, subsequently, the degree of elastic recovery (15). Another theory suggests that ISE is related to the fracture process (13, 14). Conventional hardness tests measure only the area of the permanent impression left by the indenting body *after* unloading, and are typically only concerned with visible fracture when it impedes measurement of the impression (16–19). Therefore, the procedures do not take into account the mechanical or fracture response of the material during the actual deformation process. The impression area at maximum load may be different than the plastic impression left after unloading due to the elastic recovery of the indented surface. Thus, the maximum indentation hardness could be different from that measured using the remnant impression. The degree and type of fracture formed during indentation around and under the indent surface, which may not be easily characterized though surface inspection alone, is also load-dependent. Different crack morphologies may also initiate at different stages of the indentation process, affecting the total depth of penetration or the indentation size. Thus, it is important to characterize not only the surface of the resulting indentations, but also area underneath the indentation. For these reasons, it is of interest to measure the in-situ indentation hardness as well as characterize the development and onset of fracture during the indentation process.

The most commonly used empirical equation to describe the ISE is Meyer's law (10, 21):

$$P = Kd^n, \quad (3)$$

where P is the load, d is the diameter of the impression, K is material constants, and n is often referred to as the Meyers index. Upon relating Meyer's law to the standard definition of hardness, it can be seen that hardness is load-invariant when n is equal to 2. Thus, any deviation of n from 2 is a measure of the ISE (21).

Yet another significant challenge in interpreting the indentation behavior is how to relate the force–displacement behavior of the indentation process to the stress–strain constitutive behavior of the material. In brittle materials, it is difficult to measure the uniaxial compressive behavior, and the deformation mechanisms can be sensitive to stress state. Tabor (20) first described this relationship for a spherical indenter contacting a metal, defining the indentation stress σ_I and indentation strain ε_I as follows:

$$\sigma_I = \frac{P}{\pi a^2}; \varepsilon_I = \frac{a}{R}. \quad (4)$$

The indentation stress relationship takes the same forms as the Meyer’s hardness, $H_M = P/\pi a^2$, but is measured in-situ as opposed to the traditional approach, which measures the area of the remnant impression. Previous studies attempting to link indentation stress–strain, gathered from indentation force–displacement curves, to uniaxial compression stress–strain behavior have been met with limited success (22, 23). The next challenge becomes relating indentation stress–strain behavior to the stress–strain behavior in more conventional loading geometries, such as uniaxial compression. In the elastic regime, the indentation stress–strain behavior can be expressed in a linear fashion:

$$\sigma_I = \left(\frac{4E^*}{3\pi} \right) \varepsilon_I. \quad (5)$$

Any deviation of the stress–strain curve from linearity is indicative of yielding. To describe the strain hardening behavior after yielding, an empirical description can be used (21):

$$\sigma_I = A\varepsilon_I^x, \quad (6)$$

where σ_I is the stress, ε_I is the strain, A is a material constants, and x is the strain hardening coefficient, all of which range between 0 and 1. Evaluation of the indentation stress–strain response, using the force–displacement curve, allows for the yield point to be defined and for any strain hardening behavior to be identified, as both are common inputs parameters in ballistic simulations.

4.6.2 Inelastic Deformation of Transparent Fine-Grained Spinel

Indentation tests were performed on two transparent spinel materials produced by Andreas Krell (Fraunhofer Institute for Ceramic Technologies and Sintered Materials, Dresden, Germany) using a sintering and hot isostatic pressing process. The nominal grain sizes of the two spinels supplied were nominally 0.6 μm (ID 205-2 small) and 1.6 μm (ID 200-11 large), henceforth referred to as “small” and “large” for simplicity. The small- and large-grain spinel had nominal thicknesses of 5.95 and 5.97 mm, respectively. The average bulk density of the spinel plates was 3.57 g/cm^3 and the nominal peak-to-valley surface roughness was 250 to 400 nm. Optically, the small-grain spinel appeared cloudy or milky, and the large-grain had a slight yellow hue. While

both samples contained small opaque heterogeneities, the opaque heterogeneities are more prevalent and greater in magnitude in the large-grain spinel.

To verify the reported grain size of the two spinels, specimens were polished to a $0.25\text{-}\mu\text{m}$ finish and then chemically etched by immersing them in boiling phosphoric acid—30 s for the small-grained spinel and 40 s for the large. Upon removal from the etchant, samples were immersed in boiling water to stop the etching process and then rinsed in an ultrasonic cleaner. Specimens were then cleaned and sputter-coated with gold for observation on a scanning electron microscope (Model 6700F FESEM, JOEL USA Inc., Peabody, MA). Shown in figure 22 are representative scanning electron microscopy (SEM) micrographs, and the accompanying binary images created from the same micrographs using the image processing tools (Image J, version 1.42, National Institute of Mental Health, Bethesda, MD) to enhance the appearance of grain boundaries. Micrographs of the small-grained spinel are representative of the overall grain size and morphology; however, those taken of the large-grained spinel should be taken at a lower magnification to give a more accurate representation of the grain size and morphology since there appears to be a bimodal grain-size distribution in this specimen.

The binary images shown in figure 23 were used to determine the Feret's diameter, which is the longest distance between any two points along the selection boundary. Figure 23 shows all the grains that were included in the automated evaluation; grains that intersected the edge were excluded from the analysis. Analysis of the small-grain spinel showed an average Feret's diameter of $0.35\text{ }\mu\text{m}$ for the 129 gr counted, and an average Feret's diameter of $0.95\text{ }\mu\text{m}$ for 36 gr counted for the large-grained spinel. A histogram showing the Feret's diameter distribution for both spinels is shown in figure 24. One micrograph was analyzed for each spinel using this method. Grain size was also determined from several scanning electron microscopy (SEM) micrographs via the lineal intercept procedure described in ASTM E112 (24). Three separate SEM micrographs were analyzed for the small-grained spinel and two for the large-grained. The average grain size of the small- and large-grain spinel were 0.27 and $0.97\text{ }\mu\text{m}$, respectively. The “true” grain size is actually greater than what is found using the lineal intercept method because all grains are not bisected through their largest cross-section, thus these methods would only give a mean intercept length equal to two-thirds of the grain diameter (25) at best. Therefore, the “true” grain size for the small- and large-grain spinel would 0.36 and $1.29\text{ }\mu\text{m}$, respectively, for the lineal intercept method.

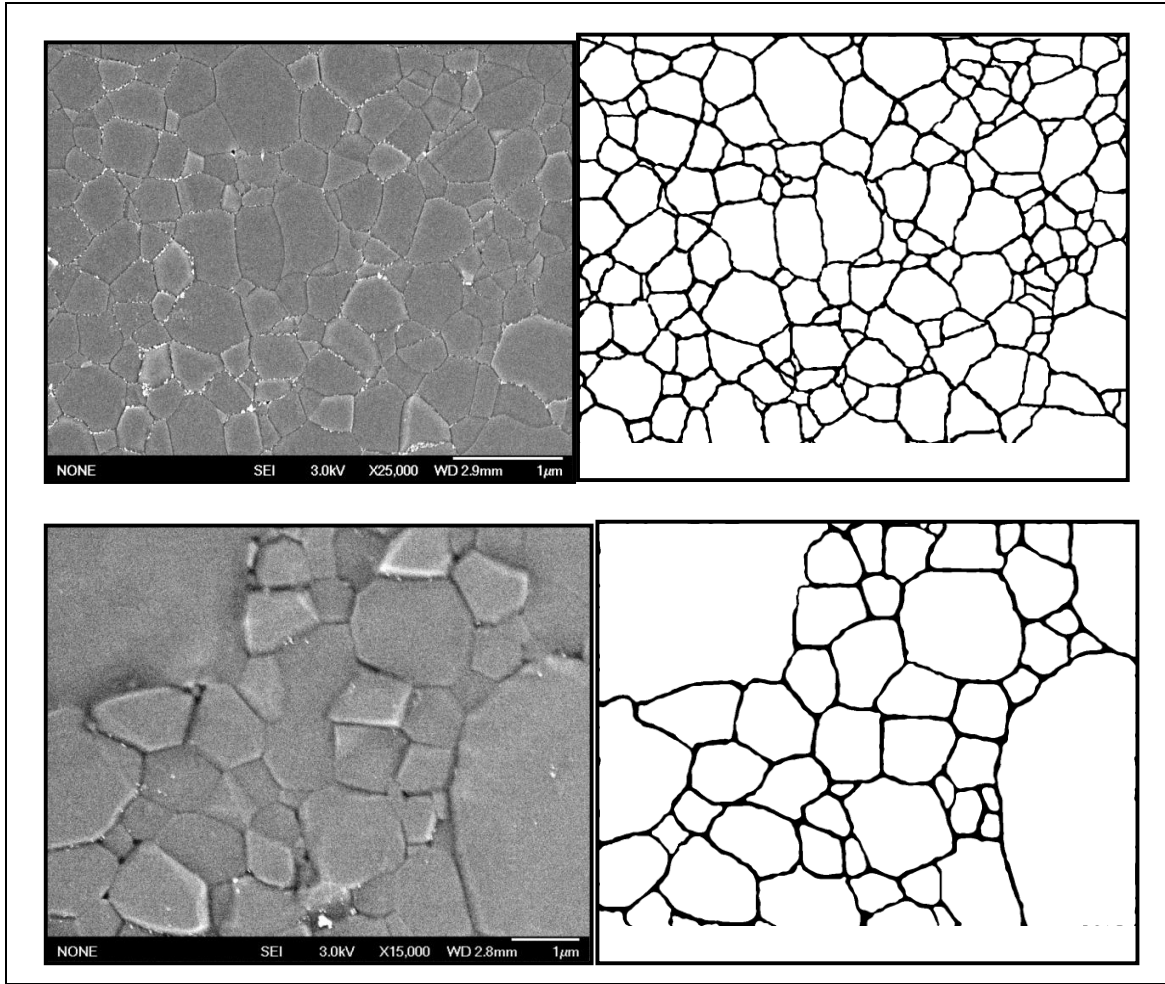


Figure 22. SEM micrograph depicting grain size and morphology, and accompanying binary images created using Image J to enhance the grain boundaries. Top images correspond to the small-grain spinel and bottom images to the large-grain spinel.

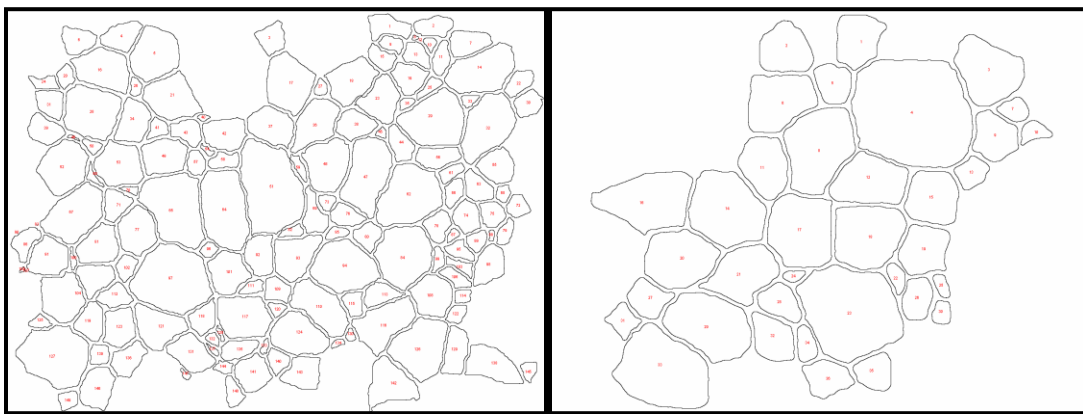


Figure 23. Binary images depicting the grains that were used to determine the Feret's diameter. The left image corresponds to the small-grain spinel and the right to the large-grain spinel (see figure 3).

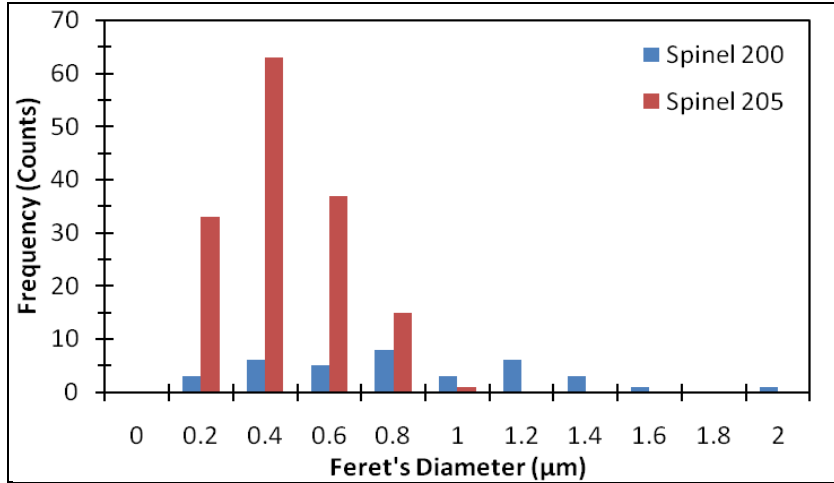


Figure 24. Histogram of Feret's diameter distribution for small-grained and large-grained spinel depicted in figure 3.

Energy-dispersive x-ray spectroscopy (EDS) and x-ray diffraction (XRD) analyses were also preformed on the two spinels that were polished to a $0.25\text{-}\mu\text{m}$ finish. The EDS spectra were collected from 0–10 keV on an FEI Quanta 200 Environmental SEM (ESEM) for both spinels and are shown in figure 25. There was no discernable difference between the two grain-size samples, and aluminum (Al), manganese (Mg), and oxygen (O) were the confirmed elements. The XRD pattern was collected from 5° – 70° 2θ using Cu-K α radiation (Panalytical Xpert Pro Mpd Theta-Theta Diffractometer), as shown in figure 26. Both XRD patterns were matched to International Centre for Diffraction Data card number 00-021-1152 for spinel MgAl_2O_4 . Close inspection of the XRD pattern shows what appears to be a small degree of peak broadening for the small-grain spinel (figure 27); this peak broadening is within instrument error and thus cannot be attributed to differences in crystallite size. The two peaks seen in figure 27 relate to the K $\alpha 1$ and K $\alpha 2$ peaks.

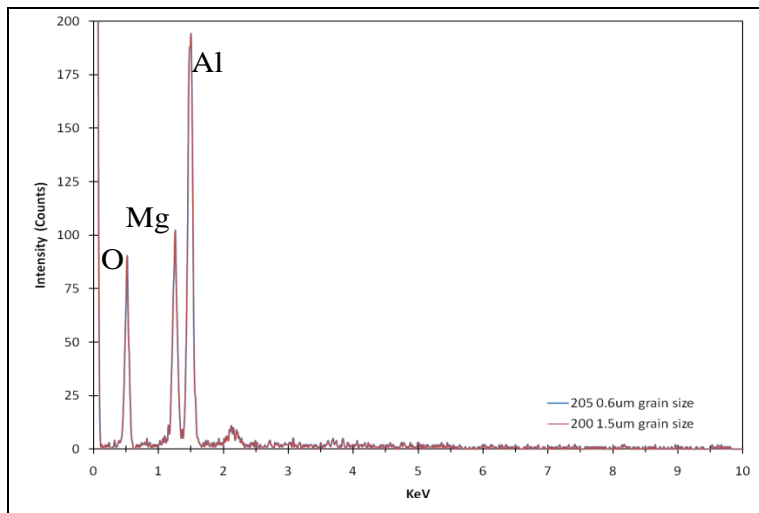


Figure 25. EDS spectrum for the small- and large-grained spinel.

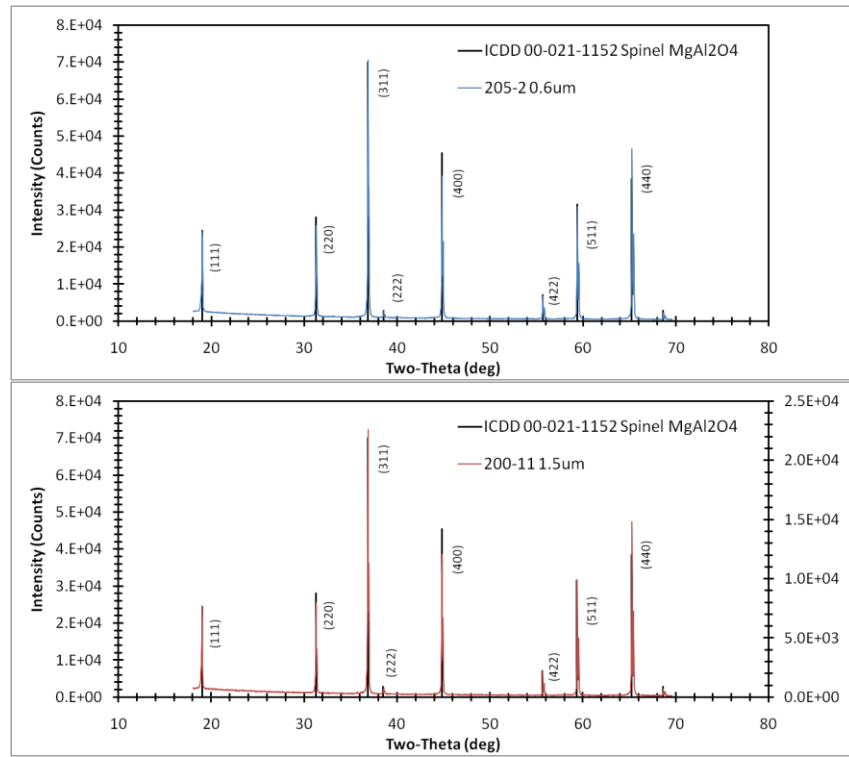


Figure 26. XRD pattern for small- and large-grain spinel matched to ICDD card 00-021-1152 spinel MgAl₂O₄.

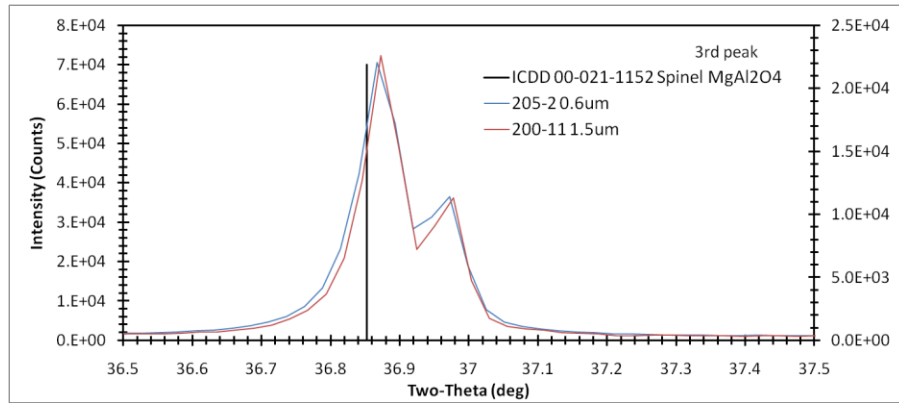


Figure 27. Enlarged view of the largest peak in the XRD pattern for the small- and large-grain spinel, illustrating the larger degree of peak broadening seen in the small-grain spinel.

A diamond indenter, radius 261 μm , was selected to assess the elastic-plastic and fracture behavior of the two transparent spinels. For this set of indentation experiments, samples were loaded using a force-controlled, triangular waveform at a constant rate to several selected maximum compressive forces. Samples were then unloaded at a constant rate. Maximum indentation forces of 50, 60, 80, 100, 130, 160, 200, 250, and 300 N were chosen to produce a comprehensive data set. A minimum of two indentations were performed at each load. After indentation, all indents were examined using the differential interference contrast (DIC) imaging techniques in an optical microscope. This imaging technique provides an enhanced view of the surface topography, illuminating not only the residual impression but any fracture patterns. Figure 28 shows the fracture behavior for the small- and large-grain spinels at three selected maximum indentation loads: 50, 100, and 200 N. Cracking was not observed at 50 N in the small-grain spinel; however, occasional ring cracking did occur in the large-grain spinel at the same load. Damage was initiated at lower loads in the large-grain spinel; therefore, the severity of the cracking was perceptively worse in the large-grain spinel than in the small. Ring and radial cracking were the primary cracking modes observed at higher loads for both spinels. SEM micrographs in figure 29 show multiple concentric ring-cracks and numerous radial cracks occurring at 250 N in both spinels.

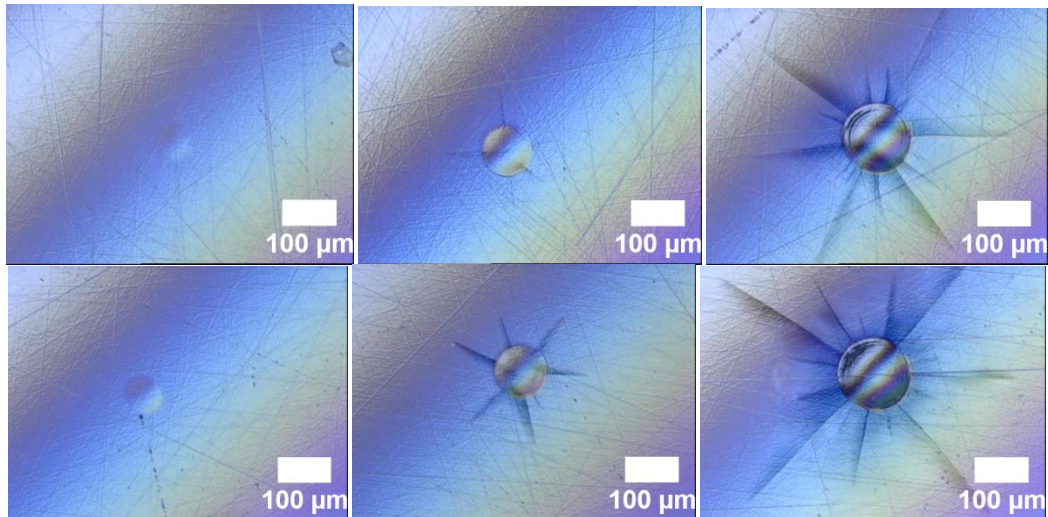


Figure 28. Differential interference contrast (DIC) images showing the typically observed cracking modes in spinel after the application of 50-, 100-, and 200-N maximum compressive forces, using a 261- μm -radius diamond indenter. Top images correspond to the small-grain spinel and the bottom to the large.

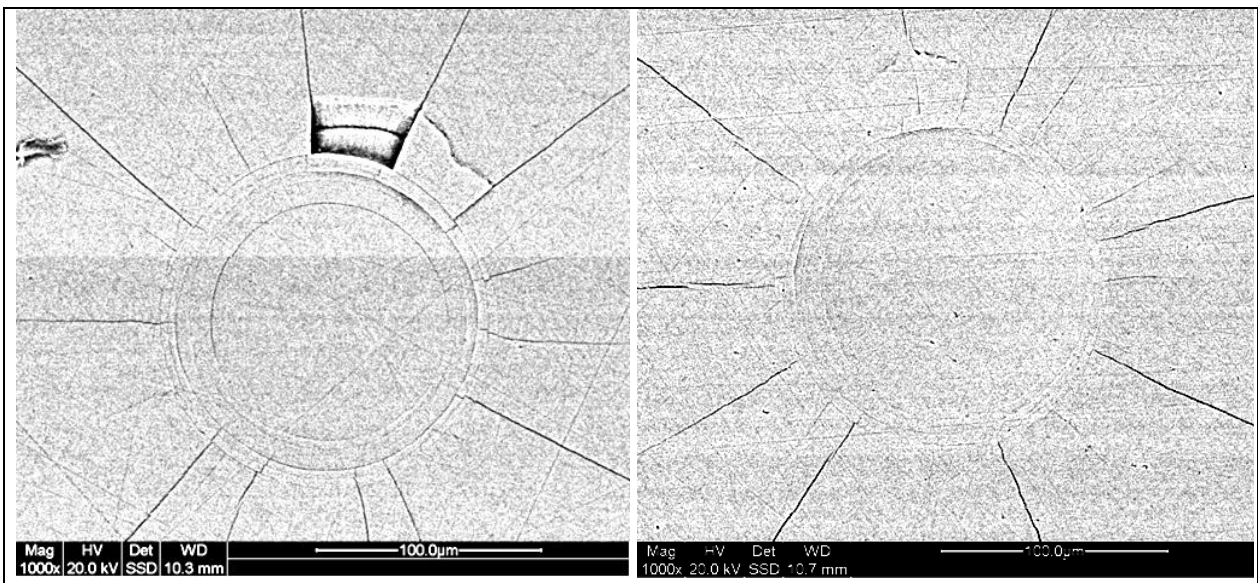


Figure 29. SEM micrograph showing the typically observed cracking modes in spinel after the application of 250-N maximum compressive forces, using a 261- μm -radius diamond indenter. Left image corresponds to the small-grain spinel and the right to the large.

The ESEM was used to characterize the subsurface cracking of several indented bend-bars, which were fractured through an indentation placed in the center of the bend-bar using a 300-N maximum compressive force on the same indenter described previously. The indented bend-bars were fractured using a three-point bend fixture. SEM micrographs of the fractured surfaces of the bend-bars are shown in figure 30. Inspection of the top surface of the indented bend-bar revealed that the fracture resulting from the three-point bend followed a radial crack until it met a ring-crack, at which point it followed the perimeter of the ring-crack and then followed another radial-crack, from right to left, for both spinels. The top surface of the micrographs shows the residual impression created during indentation for both spinels. Directly underneath the indentation site, a region of intergranular fracture can be seen for both spinels. The fracture path outside the contact region is transgranular. It is therefore postulated that the intergranular fracture is evidence that the contact-caused grain-boundary fracture that was later revealed by the cracks formed in the subsequent bend failure.

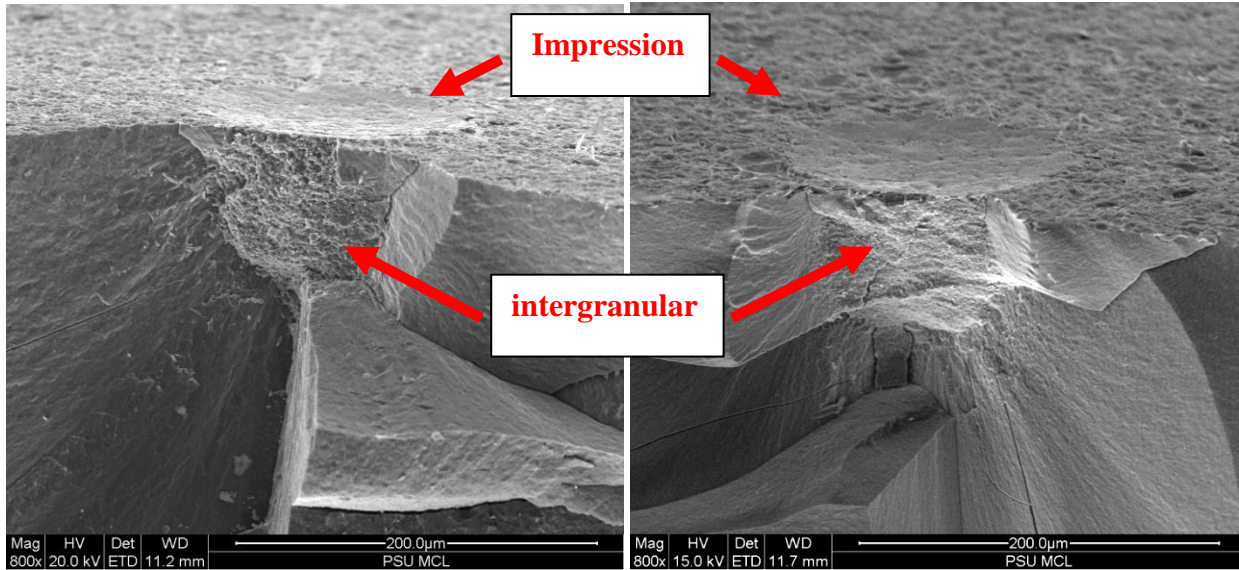


Figure 30. SEM micrograph showing the fractured surface of a three-point bend-bar in which an indentation of 300 N was placed. The left image corresponds to the small-grain spinel and the right image to the large. Note the remnant indenter impression and the intergranular fracture regions below them.

An optical profilometer (Wyko NT1100, Vecco, Tuscon, AZ) was also used to examine the surface topography to measure the diameter and depth of the plastic impression. This was determined to be more precise than optical microscopy. Additionally, these measurements could be made to quantify the pile-up of the indented surface. Figure 31 shows typical surface profiles as a function of the applied force. As can be observed, the pile-up becomes increasingly more significant with increasing indentation force in both spinels. Note that the maximum depth of the residual impression is less for the small-grain spinel than the large at all indentation loads, which suggests the apparent hardness of the small-grain spinel is higher. Additionally, when the residual impression shape was compared to that at maximum load, as shown in figure 32, it was seen that the elastic recovery was large in the loading direction for both spinels. Indeed, the elastic recovery is virtually zero in the horizontal direction, as the indenter contact diameter at maximum load is the same as the diameter of the remnant impression.

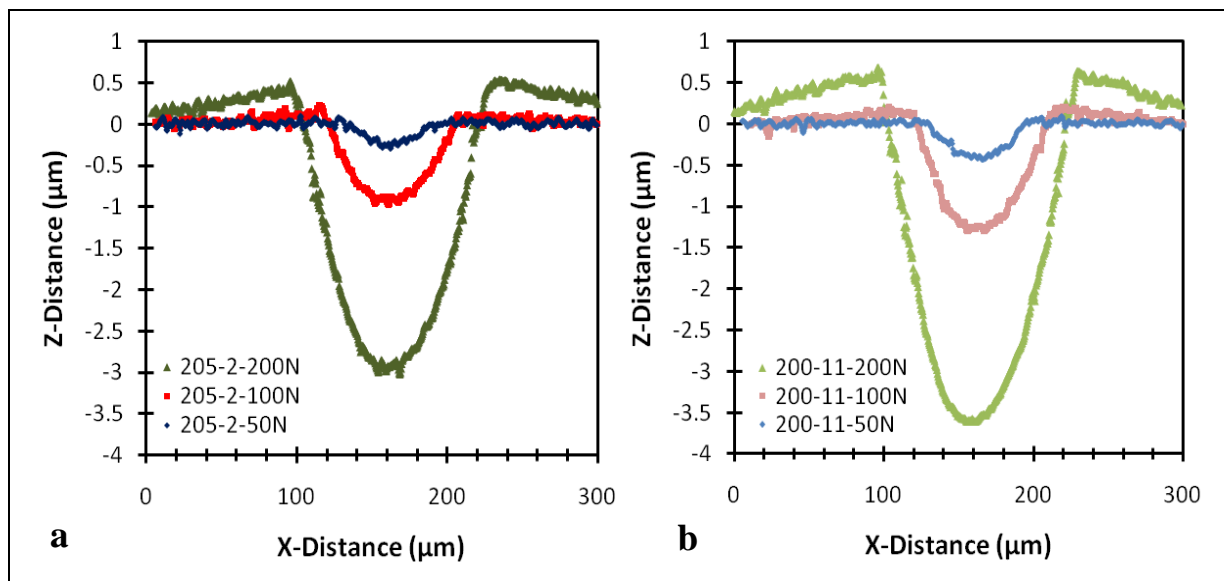


Figure 31. Optical profilometer line scans showing the typical surface profiles of the (a) small-(205-2) and (b) large-grain (200-11) spinel as a function of the applied force. Note that the pile-up increases with increasing indentation force.

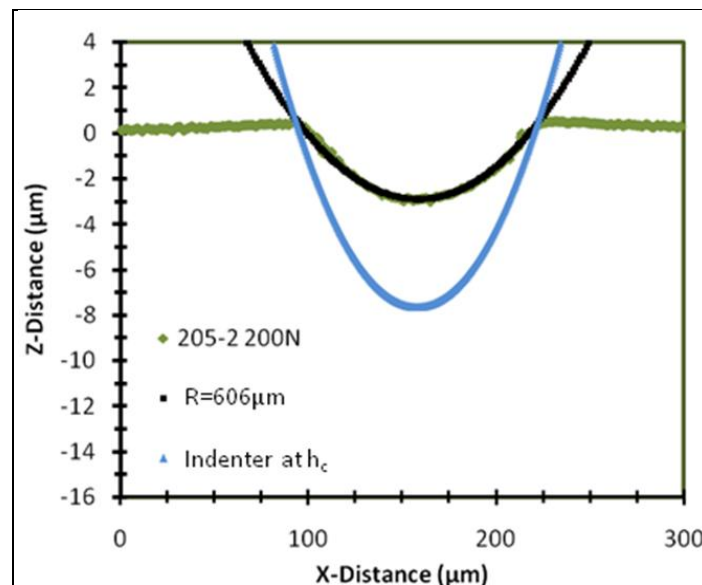


Figure 32. Comparison of impression shape in the small-grain spinel after loading to 200 N with the indenter tip shape. The profilometer scan is shown in green and the impression radius (black) was determined to be 606 μm. The contact area shape (indenter radius, 261 μm) at maximum load is shown in blue. The contact diameter at maximum load is the same as the remnant impression diameter.

Data collected for each maximum indentation load using the residual indent areas were used to calculate the Meyer's hardness, as shown in figure 33. Measurements were made to include pileup. Initial inspection of the force–hardness curve confirms that the small-grain spinel has a slightly higher apparent hardness than the large-grain spinel, as predicted from the surface profile scans. Further examination of the resulting force–hardness curve revealed a slight load dependency for each spinel. The hardness shows a decrease at small forces but this is followed by a gradual increase. Although the hardness measurements can be seen as relatively precise due to small standard error bars, there is difficulty in identifying the exact contact diameter, especially at low loads, which is not represented in the error bars. This fact could lead to significant errors in the hardness values reported at low forces. The load dependency in the force–hardness curve is very different from what is observed in the Knoop and Vickers indentation force–hardness curves of these same spinels, which depict a decrease of hardness with increasing load (26). This interesting difference could be attributed to a number of possible factors, which may include indenter geometry, fracture, elastic recovery, or simply measurement error, and should be explored further.

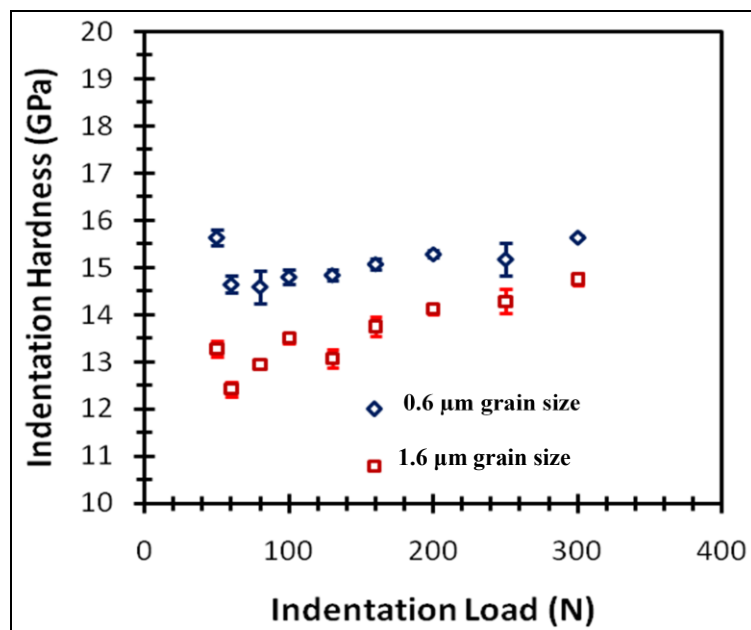


Figure 33. Meyer's hardness values measured using optical profilometer scans on the small- (205/2) and large-grain (200/11) spinel. Error bars correspond to the standard error of the mean within each given test condition.

Figure 34 shows several representative raw force–displacement curves for the small-grain spinel at maximum loads of 50, 100, and 200 N. These force–displacement curves are indicative of elastic-plastic material behavior, as it can be seen that the contact depth includes both elastic and plastic contributions to the total displacement. There is also a permanent displacement associated with the surface impression after unloading, indicated by the hysteresis.

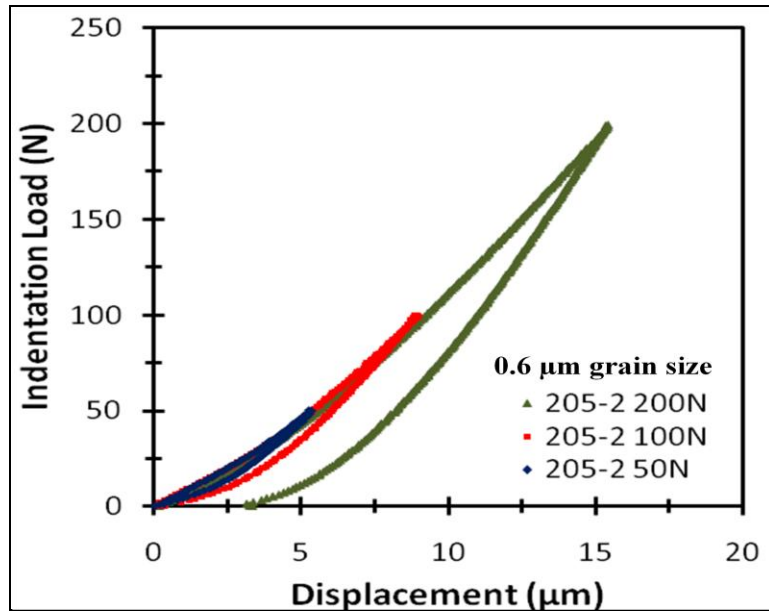


Figure 34. Representative raw force–displacement curves at maximum loads of 50 N (blue), 100 N (red), and 200 N (green), showing the full loading and unloading sequence for the small-grain spinel using a 261- μm radius spherical diamond indenter.

Through examination of the force–displacement data, it became apparent that a compliance correction was needed to analyze the elastic-plastic response. The machine compliance C is usually considered linearly elastic and, therefore, linearly dependent on indenter force P , which gives

$$h = h_t - CP, \quad (7)$$

where h is displacement associated with the contact event and h_t is the total measured displacement. For the current study, the machine compliance was determined by assuming the elastic constants of the surface are known. The single crystal elastic constants of spinel have been measured previously (27, 28) and have been used to calculate the elastic constants for randomly oriented, dense, polycrystalline spinel: $E = 275 \text{ GPa}$, $\nu = 0.267$ (29).

Two different approaches were used to relate the elastic constants to the elastic-plastic indentation behavior and determine the compliance: modified Bushby method (BS) and the Oliver-Pharr method (OP). Both methods rely on the fact that during an elastic-plastic indentation test, the loading curve progresses from elastic to inelastic. Meanwhile, the unloading curve is elastic. For an elastic-plastic case, the indented surface retains a residual curvature after unloading. Both methods make use of the following relationships for the elastic unloading displacement h_e of an elastic-plastic material:

$$h_e = h_{\max} - h_r = h_{t\max} - CP_{\max} - h_r, \quad (8)$$

where h_r is the permanent displacement associated with the surface impression after unloading. Therefore, if the elastic displacement is assumed to be equally distributed above and below the contact circle, the contact depth, h_c , becomes

$$h_e = \frac{h_{\max} + h_r}{2}. \quad (9)$$

The contact radius at maximum force is given by (6)

$$a_{\max}^2 = 2Rh_c - h_c^2. \quad (10)$$

The BS method utilizes the Hertzian elastic contact solution, but makes the assumption that a residual impression with a radius of R' is being reloaded to determine the elastic constants. Therefore, the relationship for the elastic displacement into the surface becomes (30)

$$h_e = \left(\frac{3P_{\max}}{4E^*} \right)^{2/3} \left(\frac{1}{R} - \frac{1}{R'} \right)^{1/3}, \quad (11)$$

and if one assumes the elastic recovery is only in the indenter force direction, then

$$R' = \frac{a^2 + h_r^2}{2h_r}, \quad (12)$$

where h_r is the depth of the residual impression.

The OP method (31) uses the unloading slope S at maximum load to determine the elastic constants:

$$S_{P=P_{\max}} = 2E^*a = 2E^*\sqrt{2Rh_c - h_c^2}, \quad (13)$$

where the depth of contact h_c is defined as

$$h_c = h_{\max} - \frac{3P_{\max}}{4S_{S=S_{\max}}}. \quad (14)$$

As previously discussed, the process for determining the compliance used in the current study involved numerically finding a compliance value C , which gave the correct E^* value using either the OP method or the BS method. The OP approach allows E^* and h_c to be determined without the need to measure h_r . The BS approach, however, can be performed in two ways: h_r and R' can be determined from the force–displacement or profilometer data. The latter data was considered to be more accurate, so this process was chosen and is termed the modified BS method, for which the machine compliance was determined to be 11.6 ± 0.3 nm/N. Using the OP approach, the machine compliance was determined to be 10.9 ± 0.6 nm/N. Clearly, there is only a very small difference between the modified BS and OP approaches. The source of this difference is believed to result from the lack of a pile-up correction to the OP data set; pile-up is included in the modified BS data set. Figure 35 shows an example of a load–displacement data and the correction for machine stiffness using the modified BS method. Both the maximum contact displacement and the unloading slope are changed significantly by the data correction.

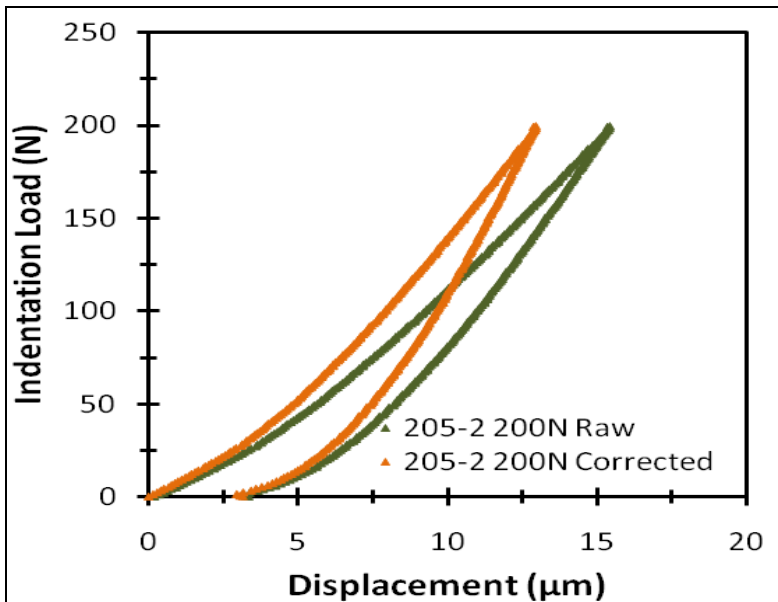


Figure 35. Comparison of a raw (green) and a machine stiffness-corrected (orange) force-displacement curve showing the full loading and unloading sequence for the small-grain (205/2) spinel using a 261- μm -radius spherical diamond indenter.

The experimental data gathered was also used to measure hardness and indentation stress–strain curves. The aim was to produce a better understanding of the difference between in-situ hardness measurements and those determined from the impression size after unloading. Figure 36 compares the stress–strain values for the two spinel materials using both the modified BS and OP compliance correction methods. As can be seen, these two analysis methods produced slightly different results; the percent difference is less than 2%. Consequently, the contact areas determined at maximum load differ slightly for each method.

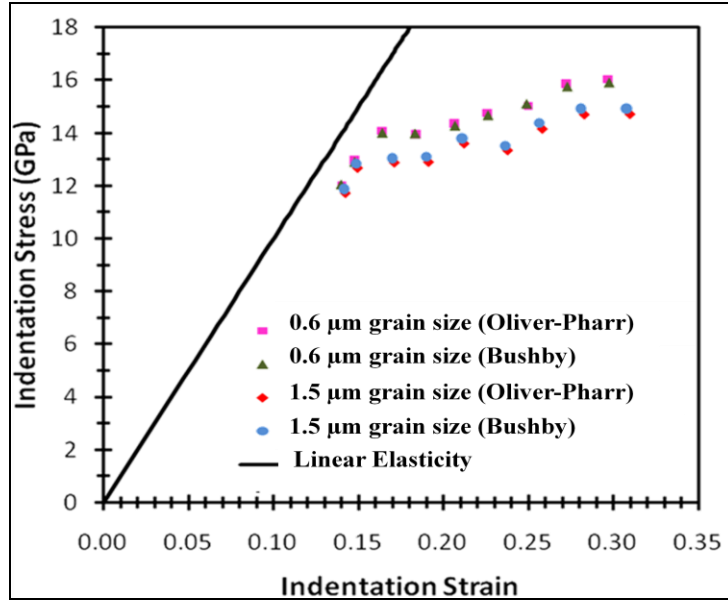


Figure 36. Comparison of indentation stress–strain curves obtained using the Oliver-Pharr and Modified Bushby methods on small- (205/2) and large-grain (200/11) spinel using a 261- μm -radius spherical diamond indenter. Error bars corresponding to the standard error of the mean are contained within the marker.

The finer grain-size spinel exhibits slightly higher stress values for given strains and higher yield stress—a 1%–10% difference, depending on the load, for both correction methods. The percent difference is the smallest at the lowest forces, and increases with increasing force. Based on the slope of the indentation stress–strain curves for the two materials, it appears that the strain hardening rates also differ somewhat between the different grain sizes, with the fine-grain spinel having the higher strain hardening coefficient. Figure 37 shows the stress–strain behavior corrected via only the BS method for both the small- and large-grain spinel for simplicity. A power law fit of the data sets revealed strain hardening coefficients of ~0.32 and 0.26 for the small- and large-grain spinel, respectively.

Extrapolation of these power law fits to the linear elastic stress–strain solution, also plotted in figure 37, revealed similar apparent yield stresses of ~12.1 and 11.6 GPa for the small- and large-grain spinel, respectively.

Finally, straight line fits on a plot of load-residual depth found the x-intercepts to be 49 and 41 N for the fine- (205) and coarse-grain (200) spinels, respectively. This x-intercept corresponds to the approximate onset of dimpling. Extrapolation of the stress-strain curves found the onset of dimpling to occur at 34 and 32 N for the fine- (205) and coarse-grain (200) spinels, respectively.

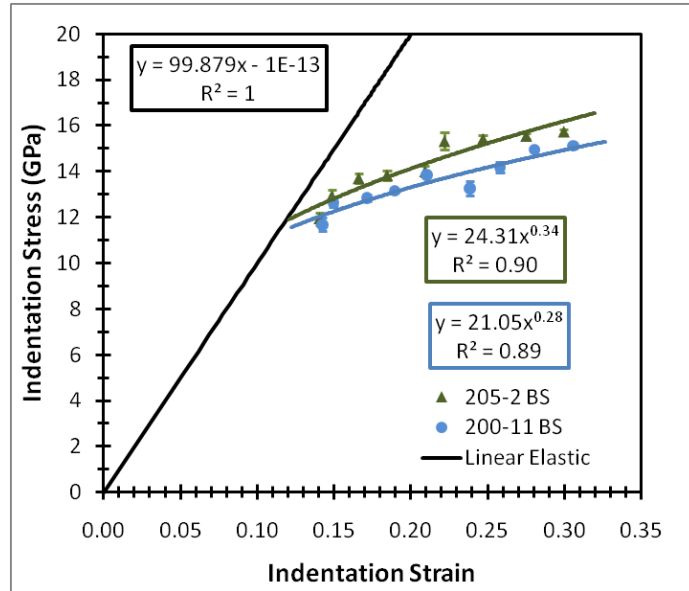


Figure 37. Comparison of indentation stress–strain curves obtained using the Modified Bushby methods on small- (205/2) and large-grain (200/11) spinel using a 261- μm -radius spherical diamond indenter. Error bars correspond to the standard error of the mean are contained within the marker. Equations are power law fits to the data.

References

1. Lawn, B. R.; Wilshaw, T. R. Indentation of Ceramics with Spheres: A Century After Hertz. *J. of the Amer. Ceram. Soc.* **1998**, *81* (8), 1977–1994.
2. Huber, M. T. On the Theory of Contacting Solid Elastic Bodies. *Ann. of Phys.* **1904**, *43* (61), 153–163.
3. Lawn, B. R.; Wilshaw, T. R. *Fracture of Brittle Solids, Cambridge Solid State Science Series*, 2nd ed.; Cambridge University Press: London, 1975.
4. LaSalvia, J., Campbell, J.; Swab, J.; McCauley, J. Beyond Hardness: Ceramics and Ceramic-Based Composites for Protection. *JOM Journal of the Minerals, Metals and Materials Society* **2010**, *62* (1), 16–23.
5. Persson, J.; Breder, K.; Rowcliffe, D. J. Loading Rate Effects During Indentation and Impact on Glass With Small Spheres. *J. of Mater. Sci.* **1993**, *28* (23), 6484–6489.
6. Fischer-Cripps, A. C., Ed. Nanoindentation. In *Mechanical Engineering Series*, 2nd ed.; Ling, F. F., Ed.; Springer-Verlag: New York, 2004; pp 1–263.
7. Muller, A. M.; Green, D. J. Elastic Indentation Response of Float Glass Surfaces. *J. of the Amer. Ceram. Soc.* **2009**, *93* (1), 209–216.
8. Chaudhri, M. M.; Yoffe, E. H. The Area of Contact Between a Small Sphere and a Flat Surface. *Philosophical Magazine A* **1981**, *44* (3), 667–675.
9. Auerbach, F. Measurement of Hardness. *Annu. Phys. Chem.* **1891**, *43*, 61.
10. Lankford, J. The Role of Dynamic Material Properties in the Performance of Ceramic Armor. *Int. J. of Appl. Ceram. Tech.* **2004**, *1* (3), 205–210.
11. McCauley, J. Inelastic Nano- and Micro- Deformation Mechanisms in Structural Ceramics at High Strain Rates and High Stress. Oral presentation at the 15th International Symposium on Plasticity and Its Current Applications, St. Thomas, V.I., 3–8 January 2009.
12. Patel, P., Swab, J.; Staley, M.; Quinn, G. *Indentation Size Effect (ISE) of Transparent AlON and MgAl₂O₄*; ARL-TR-3852; U.S. Army Research Laboratory: Aberdeen Proving Ground, MD, 2006,
13. Quinn, J.; Quinn, G. Indentation Brittleness of Ceramics: A Fresh Approach. *J. of Mater. Sci.* **1997**, *32* (16), 4331–4346.
14. Swab, J. Recommendations for Determining the Hardness of Armor Ceramics. *Int. J. of Appl. Ceram. Tech.* **2004**, *1* (3), 219–225.

15. Ren, X. J., Hooper, R. M.; Griffiths, C.; Henshall, J. L. Indentation size effect in ceramics: Correlation with H/E. *J. of Mater. Sci. Letters* **2003**, 22 (15), 1105–1106.
16. ASTM C1326-08. Standard Test Method for Knoop Indentation Hardness of Advanced Ceramics. *Annu. Book ASTM Stand.* **2008**.
17. ASTM C1327-08. Standard Test Method for Vickers Indentation Hardness of Advanced Ceramics. *Annu. Book ASTM Stand.* **2008**.
18. ASTM E384-08a. Standard Test Method for Microindentation Hardness of Materials. *Annu. Book ASTM Stand.* **2008**.
19. ASTM E10-08. Standard Test Method for Brinell Hardness of Metallic Materials. *Annu. Book ASTM Stand.* **2008**.
20. Tabor, D. The Hardness of Metals. In *Monographs on the Physics and Chemistry of Materials*; Jackson, W., Frohlich, H., Mott, N. F., Eds.; Oxford University Press: New York, 1951.
21. McColm, I. J. *Ceramic Hardness*; Plenum Press: New York, 2000.
22. Hebert, E. G., Pharr, G. M.; Oliver, W. C.; Lucas, B. N.; Hay, J. L. On the Measurement of Stress-Strain Curves by Spherical Indentation. In *Proceedings of the 28th International Conference on Metallurgic Coatings and Thin Films*, San Diego, CA, 30 April–4 May 2001; Materials Research Society: Warrendale, PA, 2001; Vol. 398–399, pp 331–335.
23. Juliano, T. F.; VanLandingham, M.R.; Weerasooriya, T.; Moy, P. *Extracting Stress-Strain and Compressive Yield Stress Information From Spherical Indentation*; ARL-TR-4229; U.S. Army Research Laboratory: Aberdeen Proving Ground, MD, 2007.
24. ASTM E112. Standard Test Methods for Determining Average Grain Size **2012**.
25. Underwood, E. E., Ed. *Quantitative Stereology*; Addison-Wesley Publishing Co.: Boston, MA, 1970.
26. McCauley, J. W. Personal conversation with V. Domnich and D. Slusark re: *Transparent Spinel Data Report*; Rutgers University: New Brunswick, NJ, 2009.
27. Hilbert, E. G. *Ultrasonic Measurements of the Elastic Properties of Single-Crystal Magnesium Aluminate Spinel, MgAl₂O₄*; Doctoral dissertation; Pennsylvania State University: University Park, PA, 1984.
28. Suzuki, I.; Anderson, O. L. Elasticity and Thermal Expansion of A Natural Garnet Up to 1000 K. *J. Phys. Earth* **1983**, 31, 125–138.

29. Graham, E. K.; Munly, W. C.; McCauley, J. W.; Corbin, N. D. Elastic Properties of Polycrystalline Aluminum Oxynitride Spinel and Their Dependence on Pressure, Temperature, and Composition. *J. of the Amer. Ceram. Soc.* **1988**, 71 (10), 807–812.
30. Bushby, A. Nanoindentation Using Spherical Indenters. *Non-Destructive Testing Evaluation* **2001**, 17, 213–234.
31. Oliver, W. C.; Pharr, G. M. Improved Technique for Determining Hardness and Elastic Modulus Using Load and Displacement Sensing Indentation Experiments. *J. of Mater. Res.* **1992**, 7 (6), 1564–1580.

4.7 Dynamic Compressive Strength of Micron and Sub-Micron Grain Polycrystalline Spinel (MgAl_2O_4)

J. Kimberly and K. T. Ramesh, The Johns Hopkins University

4.7.1 Introduction

The compressive strengths of polycrystalline spinel specimens with micron ($1.6 \mu\text{m}$) and sub-micron ($0.6 \mu\text{m}$) mean grain size are measured under dynamic uniaxial compression. A modified Kolsky bar is used to subject specimens to dynamic compressive loading at strain rates up to 2000 1/s . High-speed imaging is used to identify the locations of failure initiation as well as track the propagation of failure in the specimen during the dynamic compression experiments. This provides insight to the nature of the failure process. The dynamic strength measurements are compared with quasi-static strength measurements to identify any rate sensitivity in the compressive strength of either the micron- or submicron-grained spinel specimens.

4.7.2 Specimen Details

Specimens were cut and polished (service provided by Prematech, Worcester, MA) from two plates of polycrystalline spinel (MgAl_2O_4) of different grain sizes produced by the Fraunhofer Institute for Ceramic Technologies and Systems (*Fraunhofer-Institut für Keramische Technologien und Systeme*, IKTS). Plate 205/04 had an average grain size of $0.65 \mu\text{m}$, and plate 200/14 had an average grain size of $1.6 \mu\text{m}$. Specimen geometry is a rectangular prism whose cross-section is nominally a square with chamfered edges, as shown in figure 38. The h dimension is the thickness direction of the plate and was the axis of which the specimens were compressed during testing. The loading faces were lapped and polished to ensure that the faces were parallel to within $5 \mu\text{m}$ across the loading faces. Nominal dimensions of the specimen are $b, w = 3.8 \text{ mm}$, $h = 3.4 \text{ mm}$, and $k = 425 \mu\text{m}$, while exact measures of b , w , and h can be found in table 7.

Also listed in table 7 are the mass densities of each specimen that were calculated based on the mass of each specimen. The values of density show that there are no significant differences between the two plates, and they compare well with the theoretical density of 3580 kg/m^3 . Specimens are expected to have the following nominal properties: Young's modulus 275 GPa , Poisson's ratio 0.2 , and fracture toughness $1.7 \text{ MPa m}^{1/2}$.

Specimens from both plates were optically transparent but have flaws that are visible to the unaided eye. Specimens from each plate imaged with transmitted light can be seen in figure 39.

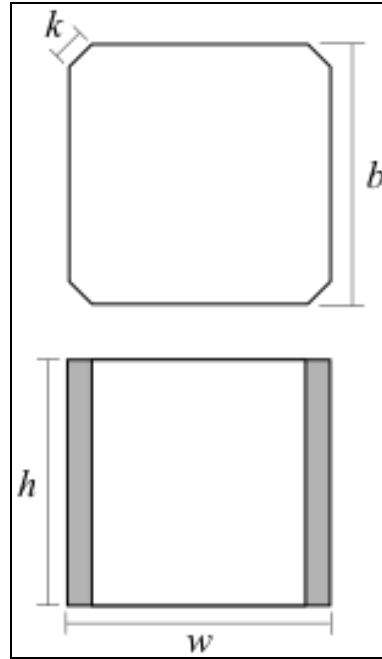


Figure 38. Specimen Geometry.
Specimens are loaded
along the h dimension.
Nominal dimensions:
 $b, w = 3.8$ mm, $h = 3.4$
mm, and $k = 425$ μm .

Table 7. Details of specimen dimensions and density.

Specimen ID	b (mm)	w (mm)	h (mm)	Mass density (kg/mm ³)
SP_205/04-04	3.818	3.818	3.478	3549
SP_205/04-05	3.819	3.821	3.374	3575
SP_205/04-06	3.816	3.816	3.339	3599
SP_205/04-07	3.815	3.801	3.428	3503
SP_205/04-08	3.816	3.822	3.378	3555
SP_205/04-09	3.822	3.817	3.419	3530
SP_200/14-06	3.816	3.806	3.430	3512
SP_200/14-07	3.814	3.804	3.446	3539
SP_200/14-08	3.82	3.809	3.449	3548
SP_200/14-09	3.817	3.789	3.501	3556

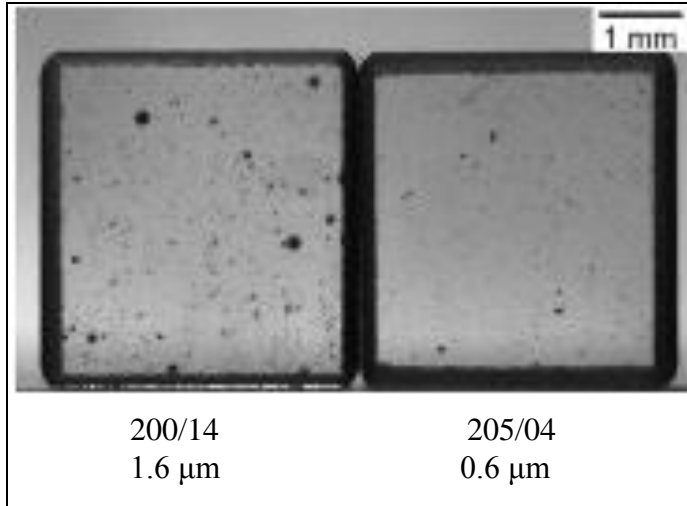


Figure 39. Comparison of optically visible defects in specimens cut from plates 200/14 and 205/04.

The dark specks visible in each specimen are yellow to white (when viewed with reflected light), and may be color centers or clusters of very small pores. In general, the specimens cut from plate 200/14 with the larger ($1.6 \mu\text{m}$) grain size appear to have larger flaws than the specimens from plate 205/04 with the smaller grain size ($0.6 \mu\text{m}$), as shown in figure 39.

4.7.3 Experimental Procedures

1. Quasi-static compression: Quasistatic uniaxial compression tests were performed under displacement control using a servo-hydraulic load frame. The crosshead displacement rate was chosen so that specimens would be tested at nominal strain rates of 10^{-4} s^{-1} and 10^{-2} s^{-1} . The compression platens of the load frame were protected from damage (from specimen indentation) by placing titanium-jacketed tungsten-carbide platens between the specimen and the machine platens. The specimen ends were lubricated with molybdenum grease to minimize frictional effects at the specimen/platen interface.

A digital charge-coupled device camera was used to capture images of the specimen during testing, providing detailed information on the evolution of damage in the specimens. The camera system recorded images at a rate of 28 Hz. Data collection software recorded load and displacement data at times corresponding to the images. Images were captured using transmitted light so that flaws and cracks would show up as dark features in the images.

2. Dynamic compression: Dynamic uniaxial compression experiments were performed using a Kolsky bar (Kolsky, 1949) that has since been modified for use in characterizing brittle materials (Chen and Ravichandran, 1997) (Frew et al., 2001). A schematic of the compression Kolsky bar used in these experiments is shown in figure 40.

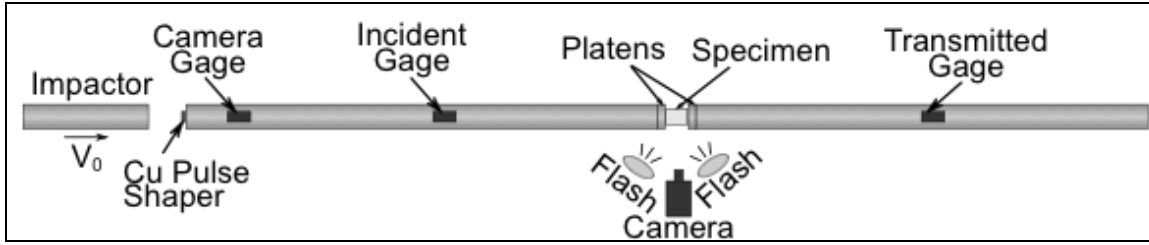


Figure 40. Schematic of the Kolsky bar set-up.

Consisting of three cylindrical bars (the projectile, the input bar, and the output bar), of equal cross-section and identical material, the bars were manufactured from 12.7-mm-diameter C-350 maraging steel hardened to a yield stress of ~ 2 GPa so that the bars remained elastic during the test. The bars were long and slender; the input and output bars were 1046 mm and 984 mm in length, respectively. A specimen was placed between the input and output bars (as in the quasi-static case, titanium-jacketed tungsten carbide platens were used together with lubrication), and the projectile was launched into the input bar at a velocity in the range of 5–30 m/s using a gas gun. To ensure that the stress in brittle specimens equilibrated before failure, a pulse shaper was used to extend the rise time of the incident pulse (Frew et al., 2002). For our experiments, the pulse shaper was a 500- μm -thick annealed copper disk that was placed between the striker and incident bar, as shown in figure 40. By changing the diameter of the pulse shaper and the impact velocity, compressive strain rates in the range of 10^2 – 10^3 s^{-1} could be achieved.

In addition to measuring the stress, strain rate, and strain in the specimen during the test (using the signals from the strain gages mounted on the bars), a high-speed camera (Hadland DRS Ultra-8) was used to record eight images detailing the spatial and temporal evolution of failure in the specimen at the microsecond time scale. Two high intensity flash sources (triggered by strain gage 1) were used to illuminate the specimen during compression. An exposure time of 200 ns was used to minimize motion blur in the images. Since the flashes were on the same side of the specimen as the camera, only light reflected by the specimen and bars was imaged, causing the specimen initially to appear dark (since it is transparent). As cracks grew in the specimen, light from the flashes was scattered by the newly created crack surfaces. The camera captured some of this scattered light, and cracks appeared as bright features against the nominally black background.

4.7.4 Experimental Results

1. Quasi-static results: A total of four quasi-static compression tests were conducted. Specimens from each plate were tested at nominal strain rates of 2×10^{-4} and 2×10^{-2} s^{-1} . Details of the individual tests follow, and a summary of all experiments is shown in table 8.

Table 8. Summary of experimental results.

Specimen ID	Grain Size (μm)	Stress Rate (MPa/ μs)	Strain Rate (s^{-1})	Compressive Strength (GPa)
SP_205/04-04	0.6	5.4×10^{-5}	2×10^{-4}	3.02
SP_205/04-05	0.6	180	650	3.52
SP_205/04-06	0.6	200	700	3.55
SP_205/04-07	0.6	350	1300	4.70
SP_205/04-08	0.6	400	1500	4.00
SP_205/04-09	0.6	4.2×10^{-3}	1.5×10^{-2}	2.75
SP_200/14-06	1.6	4.4×10^{-3}	1.6×10^{-2}	3.25
SP_200/14-07	1.6	4.2×10^{-5}	1.4×10^{-4}	3.4
SP_200/14-08	1.6	225	800	4.00
SP_200/14-09	1.6	400	1500	4.2

A plot of compressive stress as a function of time for a 1.6- μm -grain size specimen (SP_200/14-07) compressed to failure is shown in figure 41, which also includes six images corresponding to different times during the loading history. The stress–time plot shows that after an initial settling period (~55 s), stress increases linearly with time corresponding to a stress rate of 5.4×10^{-5} MPa/ μs . The corresponding strain rate, $1.4 \times 10^{-4} \text{ s}^{-1}$, for the test is calculated by dividing the stress rate by the elastic modulus of the specimen (275 GPa). Frame 1 shows the specimen in its initial stress-free state. Several large apparent flaws (dark specks) can be seen in the specimen, and the wavy borders at the top and bottom of the specimen are the result of the lubricating grease being squeezed out of the specimen/platen interface. As the specimen is compressed in the vertical direction little change is observed in frame 2. As loading continued, a crack initiated from the lower boundary and propagated into the specimen, which is visible in frame 3. After the initial growth, the crack stabilized and did not extend further in frames 4 or 5. Frame 5 was taken just before the peak stress (3.4 GPa) in the specimen was attained in the specimen. A thin line, indicating a surface flaw was activated, appeared in the lower right of the specimen. Immediately after frame 5, the specimen underwent catastrophic failure and crushed into a fine powder, some of which can be seen between the platens of frame 6.

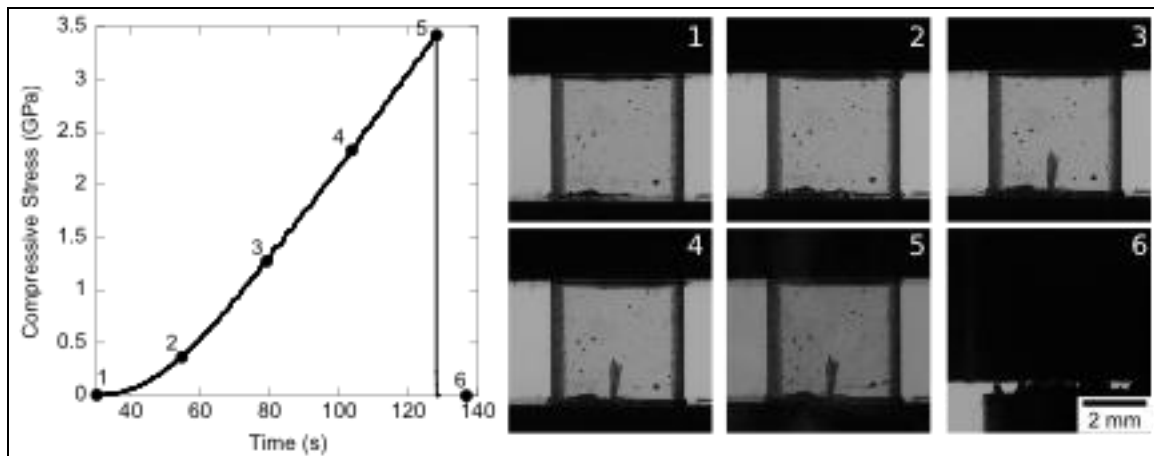


Figure 41. Specimen SP_200/14-07: 5.4×10^{-5} MPa/ μs ; strain rate $1.4 \times 10^{-4} \text{ s}^{-1}$; 1.6- μm grain size.

A specimen with 1.6- μm grain size (SP_200/14-06) was compressed to failure at a stress rate of 4.4×10^{-3} MPa/ μs , and corresponding strain rate 1.6×10^{-2} s $^{-1}$. A plot of the stress history and corresponding images of the specimen are shown in figure 42. Note that the time scale of the stress–time plot is two orders of magnitude lower than the previous experiment (SP_200/14-07). After an initial settling of the specimen (between frames 1 and 2, the stress time plot follows a linear trend up until failure (frame 5). The images of the specimen show no cracking as the stress increased from zero to peak (3.25 GPa). Directly after the peak stress was reached the specimen pulverized into a fine powder.

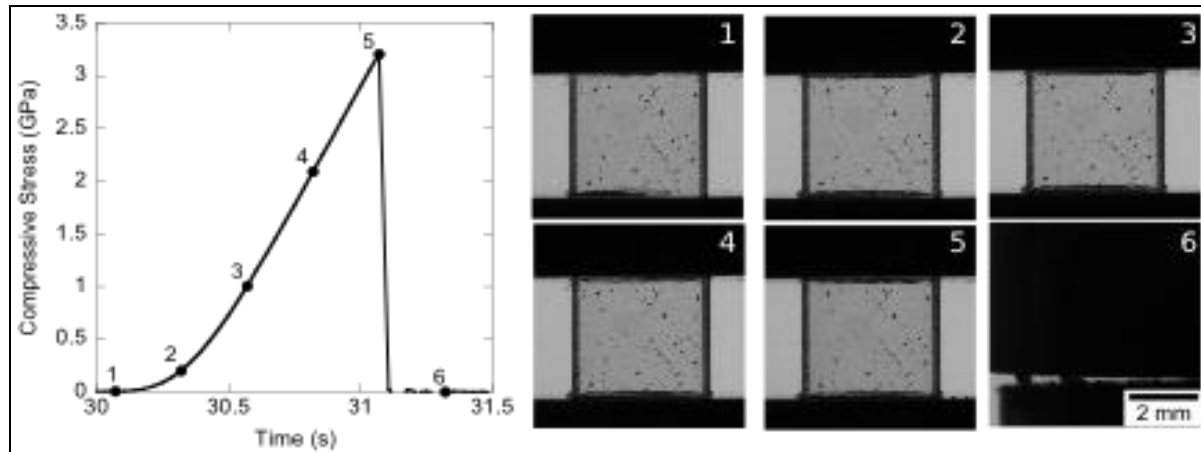


Figure 42. Specimen SP_200/14-06: stress rate 4.4×10^{-3} MPa/ μs ; strain rate 1.6×10^{-2} s $^{-1}$; 1.6- μm grain size.

Similar quasi-static compression experiments were conducted on specimens from the 0.6- μm grain-size plate. The stress–time plot and corresponding images of a specimen (SP_205/04-04) compressed at a stress rate of 5.4×10^{-5} MPa/ μs and corresponding strain rate 2×10^{-4} s $^{-1}$ are shown in figure 43. In this experiment no cracking was observed before catastrophic failure occurred at a stress of 3.02 GPa.

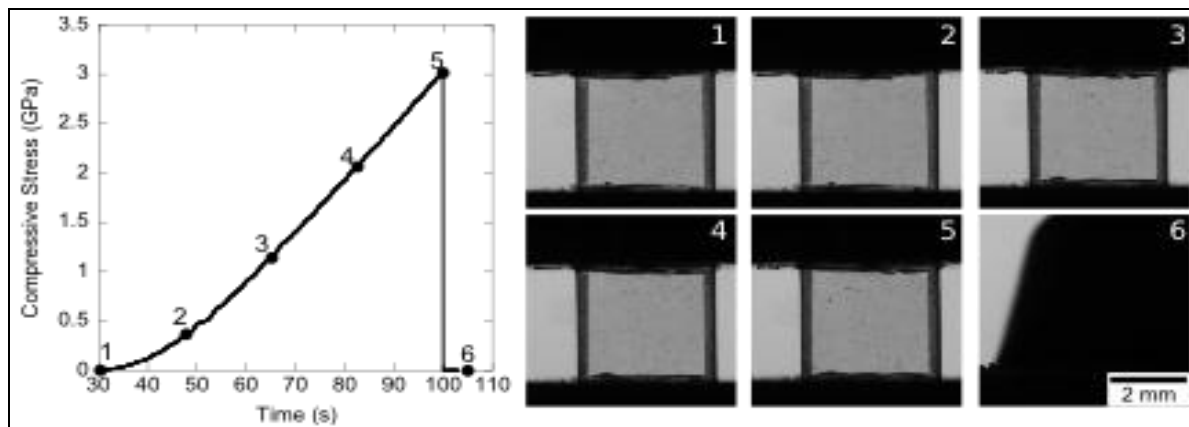


Figure 43. Specimen SP_205/04-04: stress rate 5.4×10^{-5} MPa/ μs ; strain rate 2×10^{-4} s $^{-1}$; 0.6- μm grain size.

The results from a specimen with 0.6- μm grain size (SP_205/04-09) that was compressed to failure at a stress rate of 4.2×10^{-3} MPa/ μs (strain rate $1.5 \times 10^{-2} \text{ s}^{-1}$) are shown in figure 44. During the loading, one large crack propagated into the specimen, which is visible in frame 3. This crack remained stationary as the load was increased to failure (frames 4 and 5). Immediately after the peak stress (2.75 GPa) was reached, the specimen crushed into a fine powder.

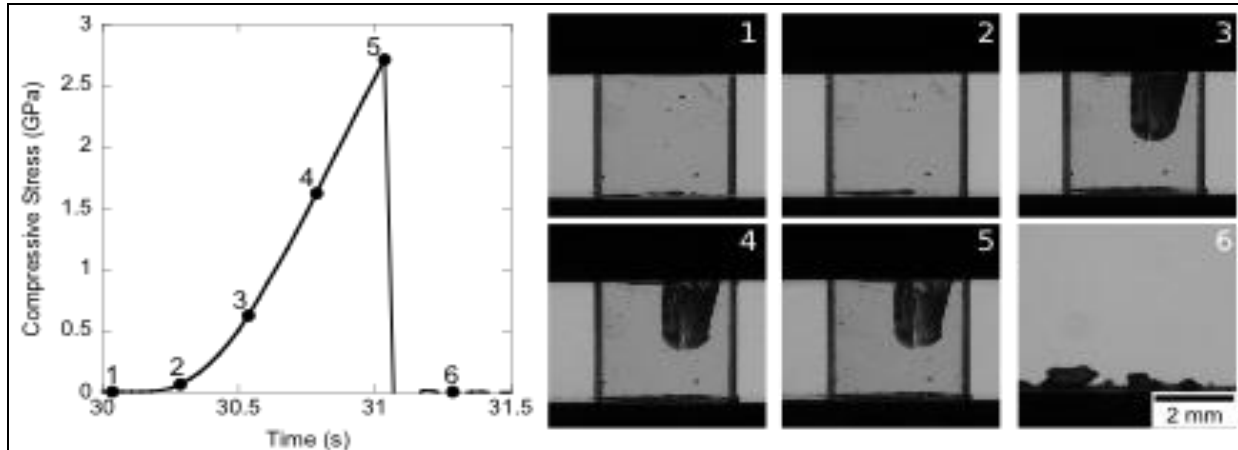


Figure 44. Specimen SP_205/04-09: stress rate 4.2×10^{-3} MPa/ μs ; strain rate $1.5 \times 10^{-2} \text{ s}^{-1}$; 0.6- μm grain size.

Comparing the results from the quasi-static experiments, it appears that the 1.6- μm -grain specimens are slightly stronger than the 0.65- μm grain specimens. This is in spite of the fact that the 1.6- μm -grain specimens have larger apparent flaws that are optically visible. Furthermore, in none of the experiments did we observe cracks growing from any of the visible flaws. This may indicate that despite their size, these visible flaws may not serve as large stress concentrations, and smaller flaws (e.g., sharp microcracks) may dominate the failure process.

2. Dynamic Compression Results:

Six dynamic compression experiments on 1.6- and 0.6- μm -grain specimens were performed using the Kolsky bar. Details of each experiment are shown in the remainder of this section, while a summary of all test results (including quasi-static results) is provided in table 8.

The stress–time plot and corresponding images of 1.6- μm -grain specimen SP_200/14-08 are shown in figure 45. Note that the timescale is now in units of microseconds and the corresponding rates are several orders of magnitude higher than the quasi-static compression experiments. After an initial ramp-up, the specimen was compressed at a nearly constant stress rate of 225 MPa/ μs (corresponding to a strain rate 800 s^{-1}) up until failure, which occurred at 4.0 GPa. The corresponding images were captured with 2 μs between frames (interframe time), allowing for details of the failure process to be captured. The specimen was compressed

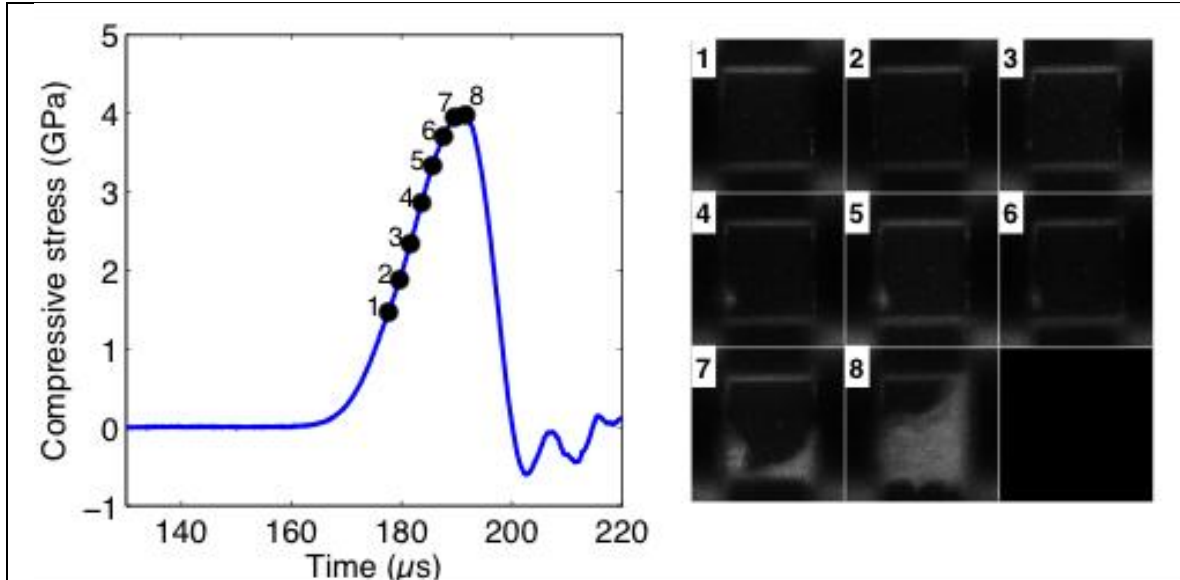


Figure 45. Specimen SP_200/14-08: stress rate 225 MPa/μs; strain rate 800 s⁻¹; 1.6-μm grain size; 2-μs interframe time.

horizontally, and the bright features at the specimen/platen interface correspond to grease being squeezed from the interface (see arrows in frames 2 and 3). In frame 4, a bright spot in the lower left corner of the specimen appears; this may be a small crack that has grown in the specimen. In the following two frames (5 and 6), this crack appears to be stationary, which is similar to observations in the quasi-static experiments. Frame 7 was taken just before the peak compressive stress in the specimen was reached. Two bright failure zones can be seen in the lower portion of the specimen. By frame 8, the cracks have propagated completely across the specimen length and have traversed almost the entire specimen. These cracks were traveling at a minimum of 1500 m/s between frames 7 and 8. This is a significant fraction of the Rayleigh wave speed $c_R=5200$ m/s, which is the theoretical limit of crack speed.

Another 1.6-μm-grain specimen plate (SP_200/14-09) was compressed at a higher stress rate—400 MPa/μs (equivalent strain rate 1500 s⁻¹)—to a peak compressive strength of 4.2 GPa. A plot of the stress history and high-speed images are shown in figure 46. We see a similar failure process, with small cracks being generated near the time corresponding to the peak stress (frames 3 and 4), and rapid crack growth just as the peak stress is attained (frames 4 and 5). Between frames 4 and 5, the cracks grew at a minimum speed of ~1500 m/s. In subsequent frames (6–8), the pulverized specimen is seen expanding in the transverse direction.

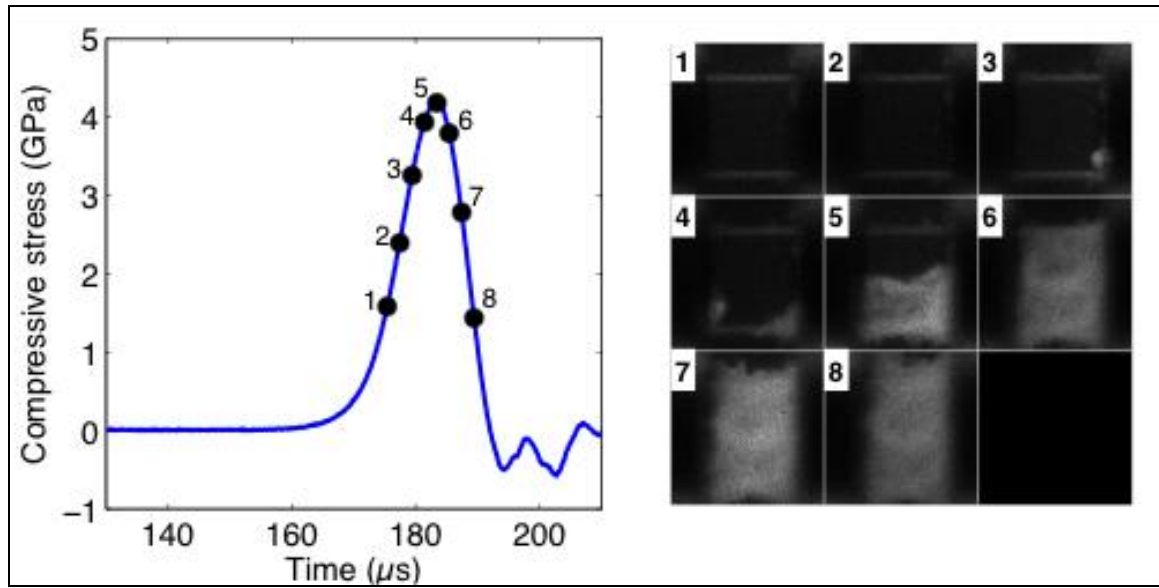


Figure 46. Specimen SP_200/14-09: strain rate 1500 s^{-1} ; 1.6- μm grain size; 2- μs interframe time.

Four dynamic compression tests were conducted on specimens from the 0.6- μm -grain plate. In the first of these experiments, the specimen (SP_205/04-05) was compressed at a stress rate of 180 MPa/ μs until failure. The stress history and high-speed images of the experiment are shown in figure 47. The peak stress in the specimen (3.52) is attained between frames 1 and 2, and the majority of the specimen has fragmented during that interval. The interframe time was 5 μs , and thus the cracks were traveling at a minimum of 700 m/s. In frames 3–8, the pulverized specimen can be seen expanding laterally between the platens.

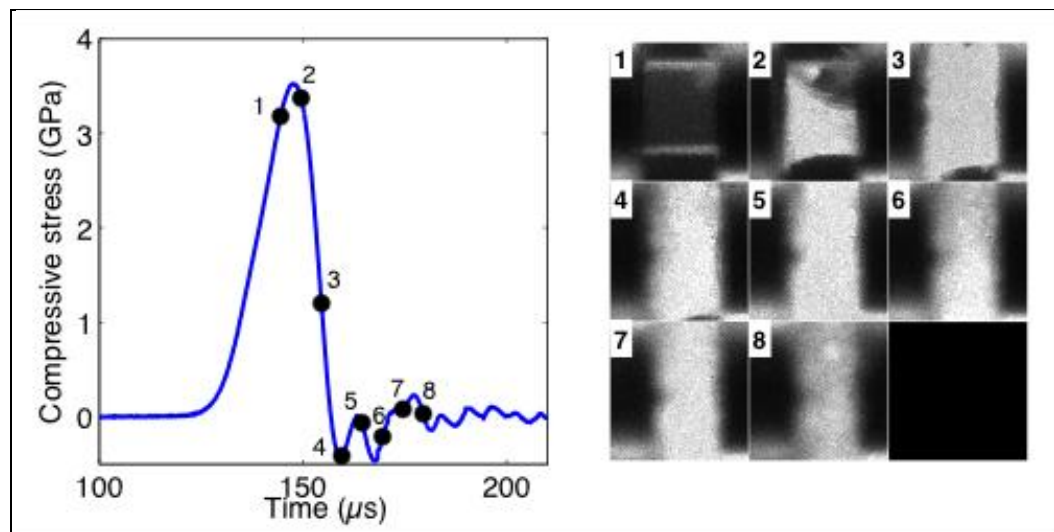


Figure 47. SP_205/04-05: stress rate $180\text{ MPa}/\mu\text{s}$; strain rate 650 s^{-1} ; 0.6- μm grain size; 5- μs interframe time.

Figure 48 shows a 0.6- μm -grain specimen compressed at a stress rate of 200 MPa/ μs (strain rate 700 s^{-1}). In frames 1–4, a surface flaw in the lower left of the specimen can be seen. This flaw appears to brighten and thicken as the stress in the specimen increases, indicating that it could be growing. At the time of frame 5, the specimen stress reached its peak value (3.55 GPa), and a small amount of cracking can be seen in the lower left of the specimen. By the time frame 6 is captured, cracks had propagated through the length of the specimen and the stress in the specimen began to drop. Since the crack crossed the entire specimen width in one interframe time (2 μs), the crack is estimated to have been traveling at a minimum of $\sim 1700 \text{ m/s}$. Frames 7 and 8 show the pulverized specimen expanding outward.

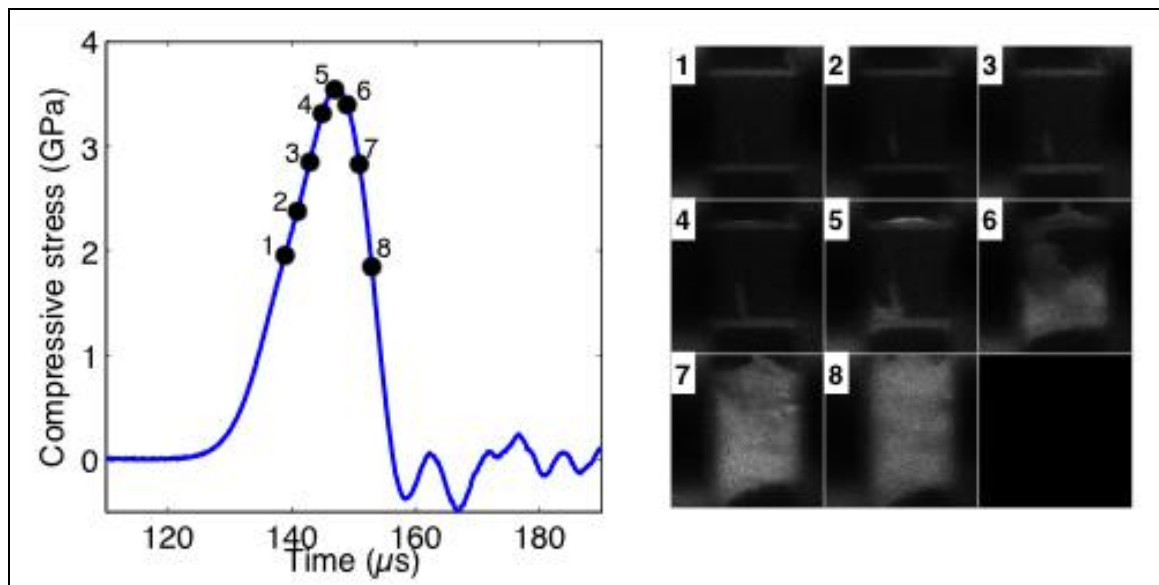


Figure 48. Specimen SP_205/04-06: stress rate 200 MPa/ μs ; strain rate 700 s^{-1} ; 0.6- μm grain size; 2- μs interframe time.

Results from an experiment in which a 0.6- μm -grain specimen was compressed at a stress rate of 350 MPa/ μs (strain rate 1300 s^{-1}) are shown in figure 49. This specimen exhibited a higher strength than expected and thus all images were captured before failure had taken place. In frame 6, a small crack appears in the lower left side of the specimen, but remains stationary as the stress increased in frames 7 and 8. Frame 8 was captured just as the peak stress (4.7 GPa) in the specimen was attained. The stress–time plot shows that after the time corresponding to frame 8, the stress in the specimen remained nearly constant for $\sim 10 \mu\text{s}$. The stress drop associated with the end of the plateau corresponds to specimen failure because the stress drop observed in the specimen happened at a time sooner than would be expected if the loading pulse ended. After the test, the fragments recovered were similar to those recovered from other dynamic compression tests that were taken to failure. (Note this interesting result: The stress attained is quite high, and the plateau in the stress near the peak may be the result of the loading pulse leveling off, or something to do with the material response.)

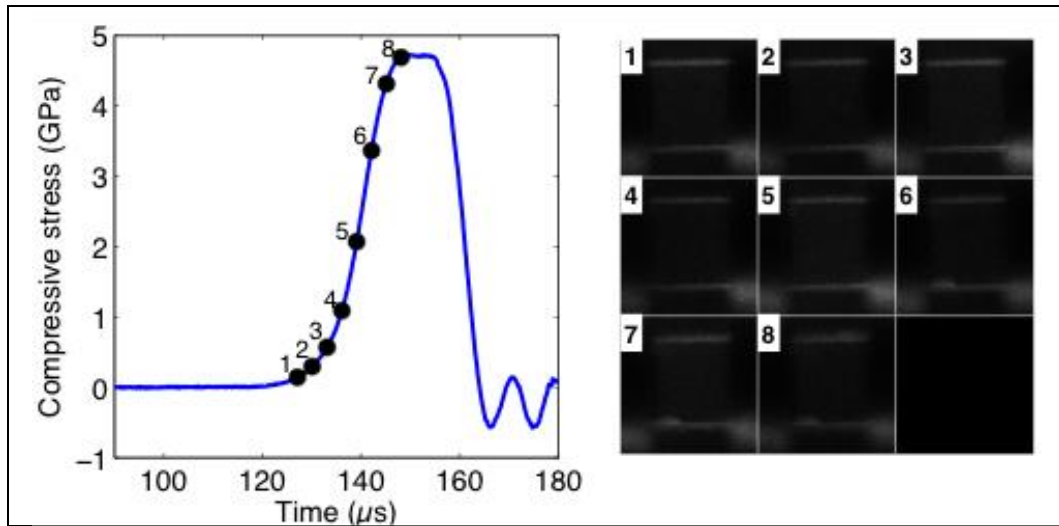


Figure 49. Specimen SP_205/04-07: stress rate $350 \text{ MPa}/\mu\text{s}$; strain rate 1300 s^{-1} ; 0.6- μm grain size; 3- μs interframe time.

The stress history and corresponding high-speed images from an experiment conducted on a 0.6- μm -grain specimen is shown in figure 50. This specimen was compressed at a stress rate of $400 \text{ MPa}/\mu\text{s}$ (strain rate of 1500 s^{-1}) until failure. After an initial nonlinear rise, the stress in the specimen rises at a nearly constant rate, and little to no change is observed in the specimen up to peak stress (frames 1–2). Just before the peak stress is reached (frame 3), bright regions corresponding to cracking are observed in the lower right and upper left corners of the specimen. By the time frame 4 was captured (3- μs interframe time), cracks have traversed the entire specimen, indicating that the cracks were travelling at least 1200 m/s . As the specimen is pulverized, the specimen stress drops to zero and the fragments of the specimen can be seen expanding in the transverse direction.

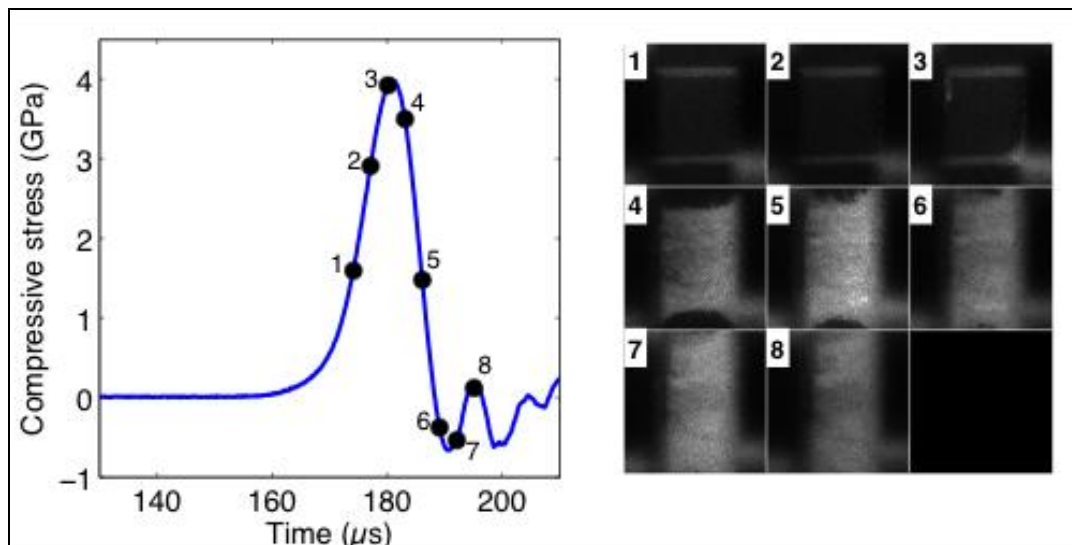


Figure 50. Specimen SP_205/04-08: stress rate $400 \text{ MPa}/\mu\text{s}$; strain rate 1500 s^{-1} ; 0.6- μm grain size; 3- μs interframe time.

4.7.5 Summary of Results

1. Compressive Strengths:

A summary of the measured compressive strengths is listed in table 8. These results are plotted as a function of stress rate (and strain rate) in figure 51.

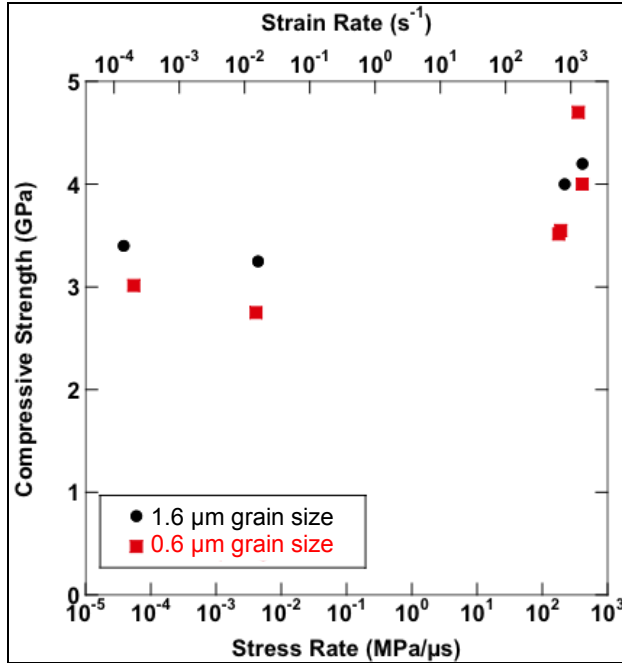


Figure 51. Summary of compressive strengths as a function of loading rate.

Both materials exhibit strain rate dependence in compressive strength, showing a ~30% increase in strength at rates above 10^2 MPa/μs compared to the quasi-static strengths (below 10^{-1} MPa/μs). Similar increases in compressive strength have been observed in the compressive failure of brittle materials. For most rates, the 1.6-μm-grain specimens seem to be stronger than the 0.6-μm-grain specimens. This result is a bit unexpected, as the specimens with 1.6-μm grains have significantly larger apparent defects compared to the specimens with 0.6-μm grains. In general, larger flaws lead to higher stress concentrations, which should result in the specimens containing the larger flaws having a lower compressive strength. For all experiments conducted here, the visible flaws in the specimen did not act as initiation sites for failure. This is in contrast to observations by Paliwal et al. (2006), where distributed microcracking was observed during the dynamic compression of AlON (another transparent ceramic) specimens. The AlON specimens had significantly larger grain size (~200 μm), and it was determined that carbon-rich inclusions on the order of 30 μm were likely the dominant flaws in the material. These carbon-rich inclusions were not visible in the specimens before testing, but distinct areas of microcracking could be observed as the stress in the specimen increased.

Since no cracks are observed to emanate from the visible flaws in the spinel specimens of this study, this may indicate that despite their large size, these flaws do not provide a strong enough stress concentration to be activated during the failure process. The visible flaws appear spherical in shape and are likely clusters of porosity. The spherical shape of these flaws would produce a lower stress concentration than an equal size sharp crack, thus it may be that smaller flaws with sharp crack geometry (e.g., microcracks, surface flaws) produce a higher stress concentration and dominate the failure process. Figure 52 shows postmortem scanning electron microscope (SEM) micrographs of a specimen fragment taken at different magnifications. These images highlight a roughly hemispherical volume of material that is protruding from the failure surface. This volume appears to be comprised of individual grains of the initial spinel powder that did not fully densify and is likely representative of the features that are optically visible in the specimens before testing (figure 39). This is a surprising result: these features “pull out” rather than get “cut” during failure. Perhaps the interface is weak enough to promote that type of failure mode. That might also explain why we don’t see these feature lighting up as we stress the specimen; essentially, these are acting as low-density inclusions.

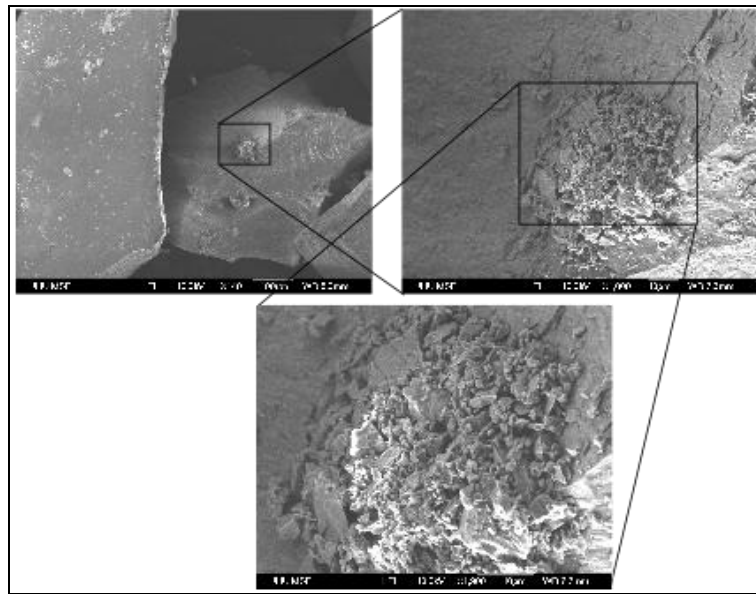


Figure 52. Postmortem SEM micrographs of a fragment from a 1.6- μm -grain specimen. The areas of higher magnification highlight an area of incomplete specimen densification. This roughly spherical cluster is likely the same type of flaw that is optically visible (see figure 39).

2. Fracture Surfaces:

Figure 53 shows an SEM micrograph of failure surfaces of a 1.6- μm -grain specimen loaded to failure under dynamic compression. We see areas of both intergranular failure (denoted by areas with smooth fracture surfaces ending at equiaxed grain boundaries) and transgranular fracture (denoted by the cleavage steps on individual grains).

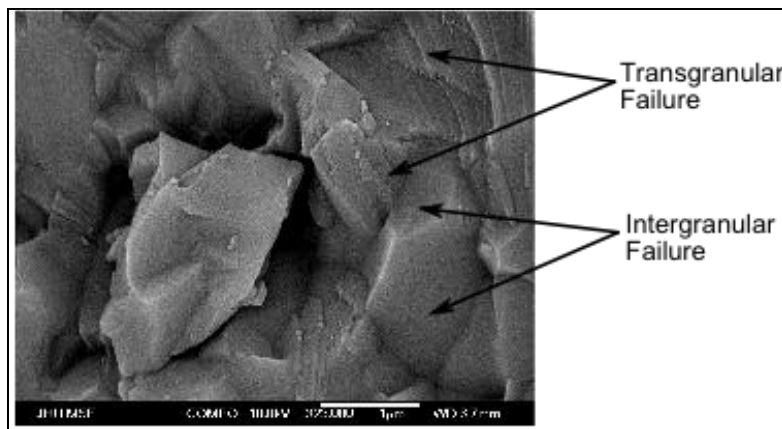


Figure 53. Postmortem SEM micrograph showing that both transgranular and intergranular fracture modes were active during failure.

References

Chen, W.; Ravichandran, G. Dynamic Compressive Failure of a Glass Ceramic Under Lateral Confinement. *Journal of the Mechanics and Physics of Solids* **1997**, *45* (8), 1303–1328.

Frew, D. J.; Forrestal, M. J.; Chen, W. A Split Hopkinson Pressure Bar Technique to Determine Compressive Stress-Strain Data for Rock Materials. *Experimental Mechanics* **2001**, *41* (1), 40–46.

Frew, D. J.; Forrestal, M. J.; Chen, W. Pulse Shaping Techniques for Testing Brittle Materials With a Split Hopkinson Pressure Bar. *Experimental Mechanics* **2002**, *42* (1), 93–106.

Kolsky, H. An Investigation of the Mechanical Properties of Materials at Very High Rates of Loading. *Proceedings of the Physical Society* **1949**, Section B, *62*, 676–700.

Paliwal, B.; Ramesh, K. T.; McCauley, J. W. Direct Observation of the Dynamic Compressive Failure of a Transparent Polycrystalline Ceramic (AlON). *Journal of the American Ceramic Society* **2006**, *89* (7), 2128–2133.

4.8 Dynamic Fragmentation of Spinel

Elmar Strassburger, M. Hunzinger, S. Bauer, Ernst Mach Institute (EMI),
Fraunhofer-Gesellschaft zur Förderung der angewandten Forschung e.V., and
P. Patel and J. W. McCauley, U.S. Army Research Laboratory (ARL)

4.8.1 Introduction

Magnesium aluminate spinel (MgAl_2O_4) is one of the candidate materials for application as a hard front layer in transparent armor. It has been demonstrated that significant weight reductions can be achieved compared to conventional glass-based armor when a transparent ceramic is used as strike face on a glass-polymer laminate (1). Due to the high number of influencing parameters, a detailed understanding of the dominant mechanisms during projectile penetration is required to improve the performance of multilayer, ceramic-faced transparent armor. On one hand, a high ballistic resistance is related to projectile deformation and erosion. On the other hand, the resistance to penetration, and therefore the ability to deform and erode the projectile, depends on the damage and failure mechanisms in the target materials. Since part of transparent armor consists of brittle materials, the fragmentation of the ceramic and glass layers plays a key role in the resistance to penetration.

Curran et al. investigated the dynamic fragmentation of brittle materials and developed models to predict fragment sizes (2). They described the fracture process in three stages: crack nucleation, crack growth, and crack coalescence. This description is based on the assumption of an inherent distribution of flaws, which are the sites of fracture nucleation, depending on the loading. Shockley et al. recently investigated the failure of glass (3) due to the penetration of steel projectiles of size and shape similar to the steel cores of armor piercing ammunition. The data derived from the post-penetration analysis of the fragmentation were used as a basis for modeling material failure and projectile penetration (4). In these models, the resistance to penetration into ceramic and glass is mainly attributed to residual strength, determined by friction and flow characteristics of the failed material.

Recently, A. Krell modified a theory of a hierachic order of influences on the wear resistance of ceramics in order to explain the variety of ballistic results observed with different ceramic target configurations (5). One main statement of this hypothesis is that the mode of fragmentation, i.e., the distribution of the fragment sizes, is playing a superior role with respect to the erosion of the projectile by the ceramic fragments.

To analyze the fragmentation of two different types of spinel, a target set-up was designed that allowed for an almost complete recovery and analysis of the ceramic fragments. Since an analysis of the recovered ceramic debris after the completed ballistic test cannot reveal which of the fragments interacted at what time with the penetrator, different visualization techniques were applied to observe the fragmentation and the ejected ceramic particles during projectile penetration.

4.8.2 Experimental Configuration and Techniques

An armor piercing (AP) projectile of caliber 7.62×51 mm with a steel core and total mass of 9.5 g was chosen for the test series. The steel core had a mass of 3.7 g and a length of 23.5 mm. The tests were conducted at two different impact velocities, nominally 850 and 1100 m/s. The complete interaction of the projectile with the target should comprise three phases: dwell, ceramic penetration, and backing penetration. Aluminum was chosen as backing material because the threshold ceramic thickness for the case of no penetration by the 7.62-mm AP projectile is very low with ceramic-steel targets. The plates of AlCuMg1 with a tensile strength 400 MPa were of the dimensions $200 \times 200 \times 25$ mm. The dimensions of the spinel specimens were $\sim 90 \times 90 \times 5.7$ mm. The ceramic tiles were glued to the aluminum backing with polyurethane glue, and the bonding layer thickness was 0.8 mm for all targets. The ceramic tiles were laterally surrounded by an aluminum frame with a small air gap of a few tenths of a millimeter between the ceramic and the frame. The aluminum frame was utilized to keep the ceramic fragments off of the interaction zone in place and not as a confinement. The target was integrated in a target box, which allowed for nearly complete recovery and analysis of the ceramic fragments, which were extracted from the target chamber through a chain of sieves and separated into size classes.

Figure 54 shows a schematic of the ballistic test configuration and the target.

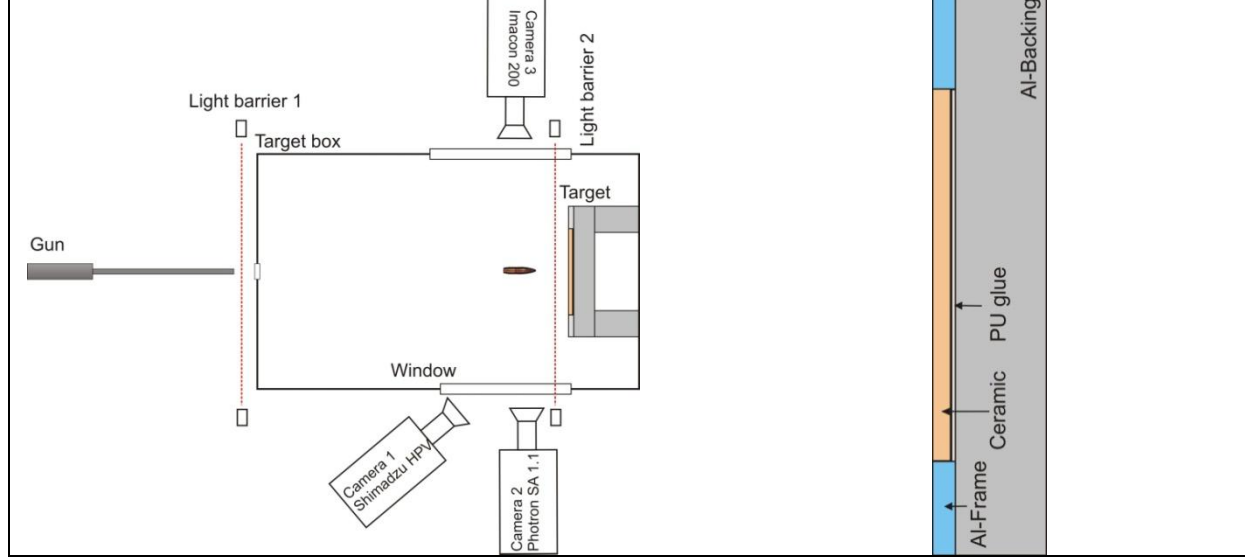


Figure 54. Schematic of ballistic test configuration (left) and target (right).

Different methods were applied to observe and analyze the fragmentation of the impacted ceramics. The first method was the recovery and size analysis of the ceramic fragments after the ballistic tests were completed. The conglomerate of projectile and ceramic fragments was extracted from the target box and collected in a sieve fabric of 25- μm mesh. Bigger parts of

the projectile jacket were sorted out manually; all ferrous particles were separated from the ceramic by means of a magnet. The ceramic fragments were separated into size classes by a chain of sieves. The mesh sizes used were 2 mm, 1 mm, 0.5 mm, 200 μm , 100 μm , 63 μm , and 25 μm . The total mass of each size fraction was determined. The dimensions and weight of the spinel specimens, as well as the weight of the complete targets before and after the impact test were measured to determine the fraction of recovered ceramic particles.

Three types of high-speed cameras were applied to visualize different phases of the fragment formation and ejection. A high-speed video camera observed the formation, development, and structure of the fragment cloud over a time period of several milliseconds. An ultra-high-speed video camera that allows recording 100 frames at a maximum rate of 10^6 frames per second recorded the beginning of the projectile target interaction with flow of projectile material at the surface of the ceramic, crack propagation in the ceramic, and the onset of the ejection of fragments. An Imacon 200 high-speed camera measured the maximum velocity of the ejected fragments.

4.8.3 Ballistic Results

The fragmentation behavior and ballistic resistance of two different types of MgAl₂O₄ spinel, manufactured by The Fraunhofer Institute for Ceramic Technologies and Sintered Materials (*Fraunhofer-Institut für Keramische Technologien und Systeme*, IKTS) in Dresden, Germany, were examined. The average grain size of the spinel type designated 205 was 0.6 μm , and the material designated spinel 200 had an average grain size of 1.6 μm . Six specimens of each spinel type were tested. The test matrix and ballistic results are shown in table 9. Both materials exhibited a good transparency. However, a high number of defects in the form of yellowish spots could be observed in spinel 200. Crossed polarizer photographs indicated only minor residual stresses in the materials.

Table 9. Test matrix and data.

Spinel Type	Impact Velocity (m/s)	EMI Test No.	Residual Penetration (mm)	Mean Residual Penetration (mm)	Residual Core Mass (g)
1.6 μm avg. grain size	846	17084	1	1.1	1.33
	842	17226	1		1.77
	839	17490	1.3		—
	1108	17085	17	15.8	2.28
	1090	17227	18.4		2.42
	1097	17492	12		1.15
0.6 μm avg. grain size	847	17087	0.7	1.2	—
	855	17228	1.5		1.37
	842	17491	1.4		—
	1114	17086	20.5	16.3	2.57
	1095	17229	13.1		2.46
	1097	17493	15.3		1.47

With respect to the ballistic resistance, no significant difference between the two spinel types was found. At 850 m/s impact velocity, nearly no penetration into the backing aluminum plate was observed with both materials. At 1100 m/s, the mean residual penetration was 15.8 mm with spinel 200 and 16.3 mm with spinel 205.

A significant difference in the erosion of the projectile steel core was observed at the two different impact velocities. Projectile erosion and fragmentation was much stronger at 850 m/s with both types of spinel. Only small pieces that could be allocated to the rear part of the steel core were found. The residual core masses given in table 1 for shots at 850 m/s are the sum of the masses of three or four bigger pieces. Most of the recovered core material consisted of tiny steel fragments. At 1100 m/s impact velocity, one big residual part of the steel core was found in each test. Figure 55 illustrates the difference in projectile erosion and fragmentation at the different impact velocities.

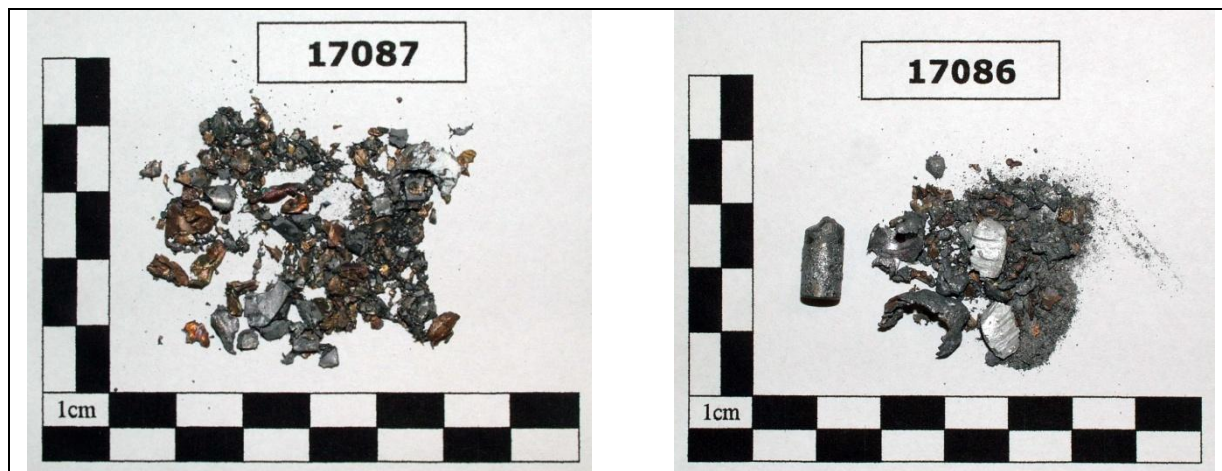


Figure 55. Residual projectile material from tests at 850 m/s (left) and 1100 m/s (right).

4.8.4 High-Speed Photography

Four tests were conducted: one test of both spinel types at 850 and 1100 m/s, respectively. Fully instrumented for high-speed photography, the tests used three types of cameras to visualize different aspects of the projectile-target interaction and the fragment formation and ejection. A Shimadzu HPV ultra-high-speed video camera, which allows recording 100 frames at a maximum rate of 10^6 frames per second, recorded the beginning of the projectile target interaction, crack propagation, and the onset of the ejection of fragments.

A selection of 12 high-speed photographs of the projectile impact on spinel 205 at 850 m/s (test no. 17087) is presented in figure 56. The frame rate was 1 MHz. The high-speed photographs show that radial cracking starts immediately with the impact of the projectile. Ring-shaped cracks can also be seen surrounding the radial crack zone during the first microseconds. The radial cracks cross the ring cracks after 3–4 μ s and propagate at a higher velocity compared to the expansion of the zone with ring cracks. The positions of crack tips were measured in four directions, and the propagation velocity was determined by linear regression. The mean value of the radial crack velocities measured was 2938 m/s. The mean expansion velocity of the circular damage zone in the center was 926 m/s. Table 10 summarizes the measured crack velocities for the two materials and impact velocities. No significant differences in the radial crack velocities could be recognized with respect to the materials and impact velocities. Different velocities were determined for the expansion velocity of the circular zone. However, the scatter in the data was much higher compared to the radial cracks.

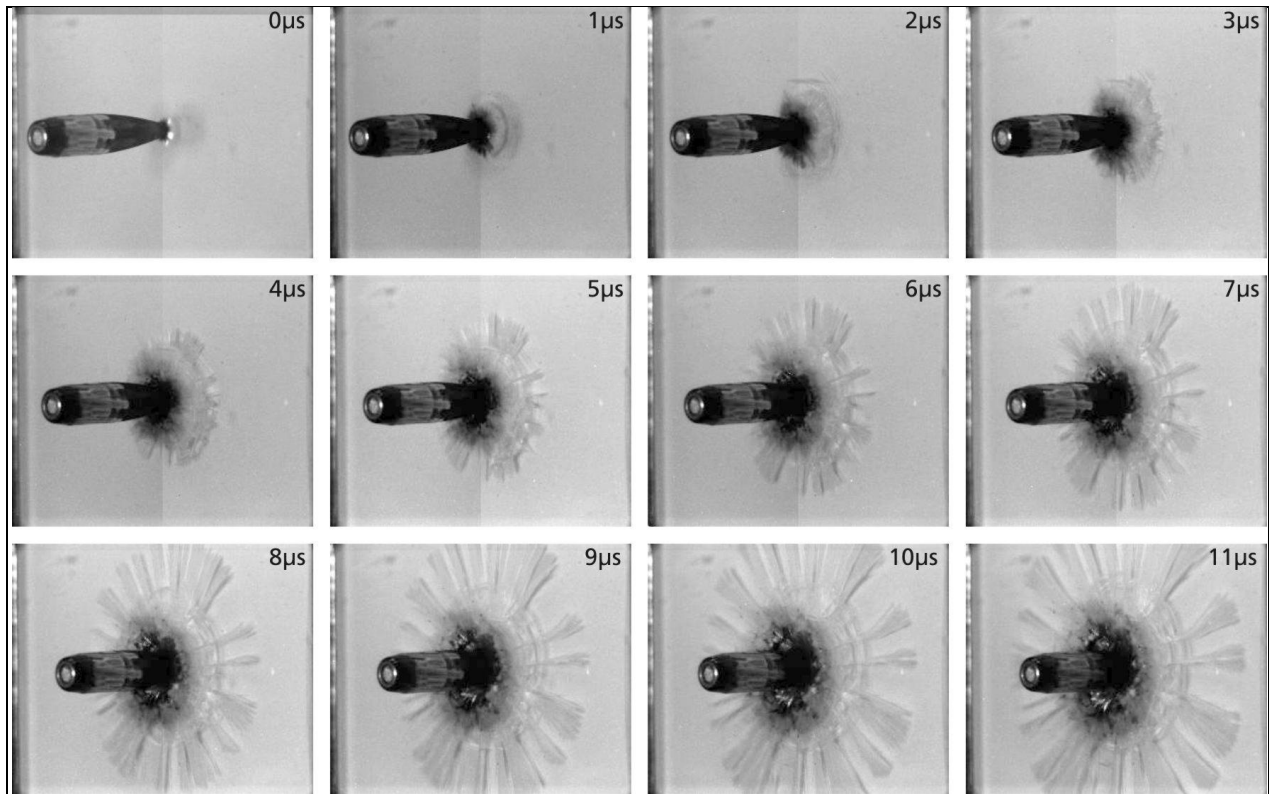


Figure 56. Selection of high-speed photographs from impact on spinel 205 at 850 m/s.

Table 9. Measured crack velocities.

Spinel	Impact Velocity (m/s)	Mean Velocity of Radial Cracks (m/s)	Mean Expansion Velocity of Circular Zone (m/s)
200	850	2954	830
	1100	3158	693
205	850	2938	926
	1100	2992	998

The ejection of ceramic fragments from the crater and the fragmented area of the ceramic specimen is illustrated in figure 57, which shows eight high-speed photographs recorded with an Imacon camera in test no. 17087 (spinel 205, 850 m/s). The width of the image section shown is about 10 cm. The ejection of fragments started shortly after the projectile impact. The surface of the ceramic specimen is close to the right edge of the photographs and the direction of the movement of the ceramic particles is from the right to the left. The average velocity of the ceramic particle front was ~500 m/s. At 1100 m/s impact velocity, the average velocity of the ejected particles was about 600 m/s during the time interval of observation.

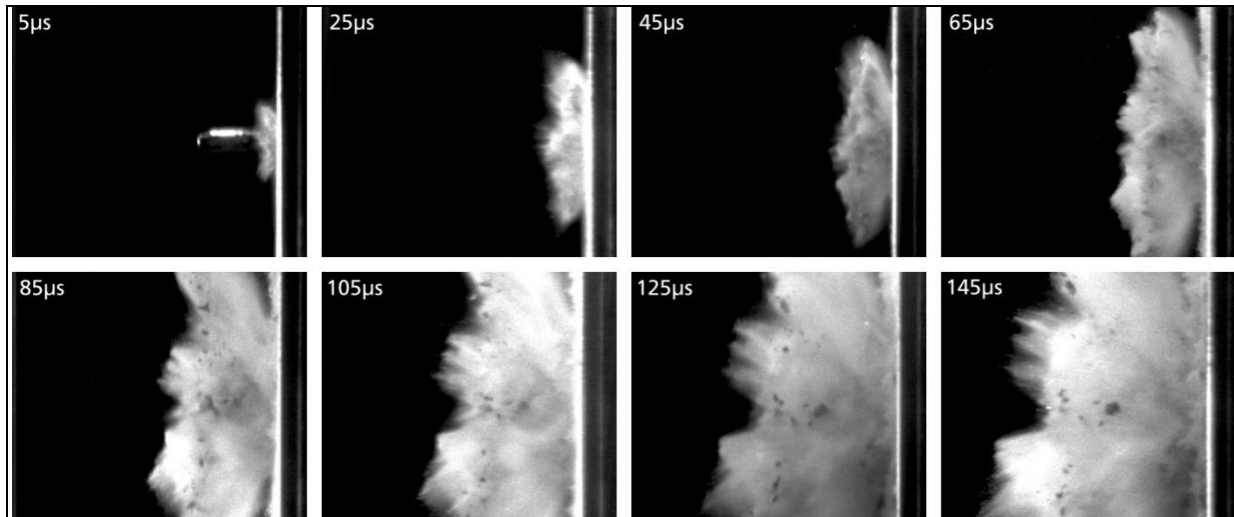


Figure 57. High-speed photographs of fragment ejection from impacted spinel ceramic (spinel 205, 850 m/s).

4.8.5 Fragmentation Analysis

4.8.5.1 Results of Sieve Analysis

The ceramic fragments were separated into size classes by a chain of sieves. The mesh sizes used were 2 mm, 1 mm, 0.5 mm, 200 μm , 100 μm , 63 μm , and 25 μm . The total mass of each size fraction was determined. Three tests were conducted with each material at two impact velocities. Table 12 lists the data for all the tests conducted. Figure 58 presents the mean values of the total fragment mass in the different size classes with the four different configurations. The variation of the fragment mass data from test to test was relatively small. The fragment size distributions appear very similar for the different materials and impact velocities. With the more fine-grained material (spinel 205), a slightly higher fragment mass was observed in the 0.5- and 0.2-mm size classes.

Table 10. Fragmentation data collected for all test conditions.

EMI Test No.	Ceramic	Total Ceramic Fragment Mass (gram) at Mesh Size (mm)						
		2 (g)	1 (g)	0.5 (g)	0.2 (g)	0.1 (g)	0.063 (g)	0.025 (g)
17084	Spinel 200/ 6 (850 m/s)	53.754	33.452	21.714	13.847	5.750	3.013	2.238
17085	Spinel 200/ 10 (1100 m/s)	48.113	30.605	18.124	10.682	4.205	2.412	2.432
17086	Spinel 205/ 10a (1100 m/s)	45.685	29.737	21.788	12.891	4.603	2.175	1.822
17087	Spinel 205/ 29 (850 m/s)	36.400	36.695	29.760	19.230	6.968	3.791	2.315
17226	Spinel 200/ 1 (850 m/s)	48.501	34.195	22.943	14.764	6.189	2.777	3.174
17227	Spinel 200/ 16 (1100 m/s)	46.831	29.121	17.627	10.063	4.045	1.83	2.283
17228	Spinel 205/ 12 (850 m/s)	41.454	30.884	22.811	14.205	5.719	2.768	3.553
17229	Spinel 205/ 15 (1100 m/s)	43.706	33.842	22.574	12.412	4.695	2.217	2.891

mean values	Spinel 200 (850 m/s)	51.128	33.824	22.329	14.306	5.970	2.895	2.706
	Spinel 200 (1100 m/s)	47.472	29.863	17.876	10.373	4.125	2.121	2.358
	Spinel 205 (850 m/s)	38.927	33.790	26.286	16.718	6.344	3.280	2.934
	Spinel 205 (1100 m/s)	44.696	31.790	22.181	12.652	4.649	2.196	2.357

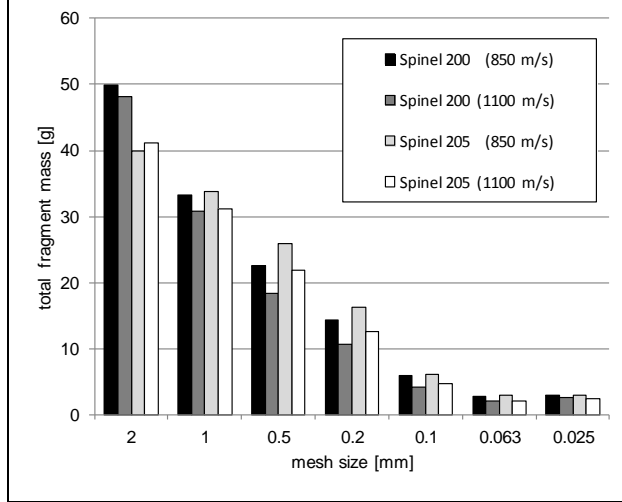


Figure 58. Fragment mass distribution; mean values from three tests with each configuration.

An order of the fragmentation behavior with respect to material and impact velocity can be recognized from the presentation of the cumulative fragment mass vs. mesh size in figure 59. A close-up of the range of small mesh sizes is displayed in figure 59b. The data in figure 59 represent the mean values of three tests for each material and impact velocity, respectively. The higher degree of fragmentation was observed with the material of smaller grain size at both impact velocities. With both materials, the higher degree of fragmentation was found at the lower impact velocity. This result is plausible, since at 850 m/s impact velocity, the residual penetration was almost zero. Thus, most of the kinetic energy of the projectile dissipated during the interaction with the spinel. At the higher impact velocity of 1100 m/s, a considerable residual penetration occurred, combined with bulging and crack formation in the backing plate.

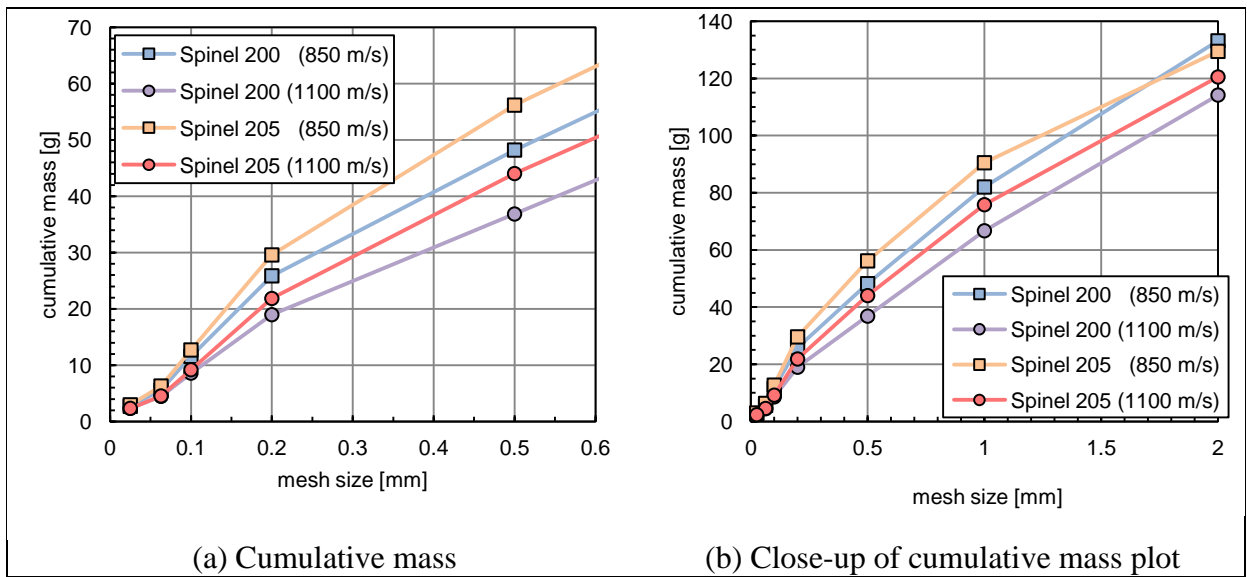


Figure 59. (a) Cumulative mass, and (b) close-up of cumulative mass plot.

4.8.5.2 Particle Tracking With Laser-Lightsheet Technique

Since the material that is in direct contact with the projectile or in the immediate vicinity cannot be visualized inside the target, an experimental method was developed that allowed observation of the fragments ejected from the crater during penetration. The key to observing single particles in the dense cloud of ejecta is the laser-lightsheet illumination technique, coupled with a high-speed video camera. With this method, it is possible to determine velocity and size of the ceramic ejecta as a function of time. The technique represents a noninvasive method to visualize single particles in a defined measuring plane with a high time-resolution rate, and allows the determination of speed, direction of motion, and size of single particles. Figure 60 shows a schematic of the experimental set-up. The punctiform laser-beam is lead into a special light-sheet-optic and converted into to a linear divergent beam. The light segment of about 1 mm thickness is led by a mirror from the top of the target box in front of the ceramic. Oriented orthogonally to the ceramic's surface, the light-sheet defines the measurement plane in which the particles are illuminated during the experiment. Particles outside the measurement plane are not, or only weakly, illuminated. Additionally, the depth of focus of the camera, which is arranged orthogonally to the lightsheet, has to be as small as possible and precisely adjusted to the illuminated plane. This way it is assured that only the light scattered from the fragments placed in the plane of the lightsheet are displayed with a clear cut to the image plane. If there is a high density of particles, illumination of the fragments out of the measurement plane is significantly weaker; the fragments appear only as a fog, clearly distinguishable from the fragments staying directly in the lightsheet. Taking into consideration the possible frame rate and the image resolution of the used complementary metal-oxide semiconductor camera, the measured area (yellow in figure 60) must be restricted to a small but significant array. Assuming a statistically symmetric distribution of the fragments within the cone of ejecta, the measurement plane was accomplished as an elongated rectangle above the line of fire.

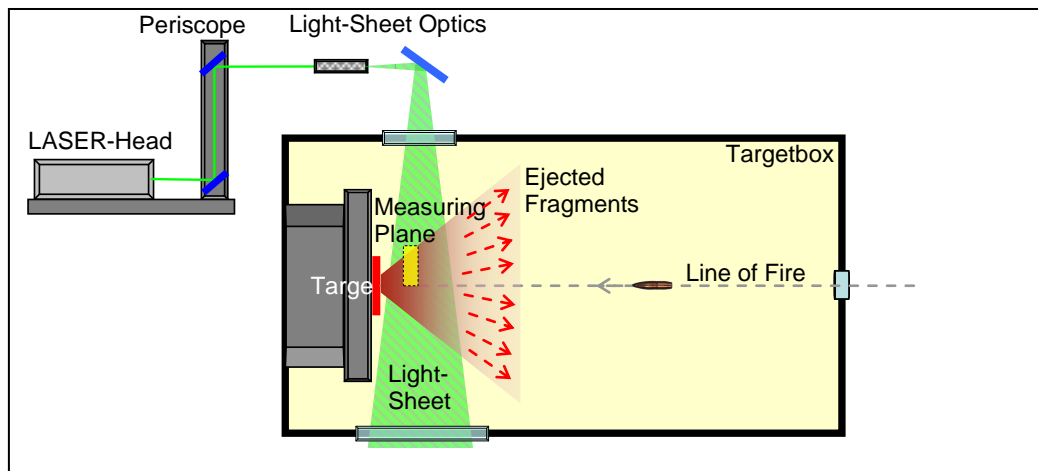


Figure 60. Schematic of the laser lightsheet illumination technique.

Figure 61 shows the average fragment size as a function of time, determined from the four tests with the two types of spinel, impacted at 850 and 1100 m/s, respectively. The data in figure 61 represent a moving average, which means that each data point is the mean value from the analysis of 50 consecutive images. The two diagrams on the left side of figure 61 compare the fragment size for the two types of spinel at 840 m/s impact velocity. For spinel 200 (1.6- μm grain size) the average fragment size was between 0.3 and 0.4 mm during the first millisecond, increased to about 0.5 mm after 2 ms, and then oscillated around 0.4 mm. For spinel 205 (0.6- μm grain size), the average fragment size oscillated mainly around 0.4 mm. With both experiments, a period of a few hundred microseconds can be recognized where the fragment size curve is flat. During these periods, no discernable fragments passed the measuring area of the lightsheet. The flat part of the fragment size curve over this time period is due to the averaging process. However, the fact that no fragments were recognized does not mean that no fragments at all passed the measuring area. Fragments smaller than 170 μm cannot be recognized with the optical set-up utilized. The average fragment sizes observed in the tests at 1100 m/s were similar to those at 840 m/s. With spinel 200, bigger fragments also appeared in the time interval between 1 and 2.5 ms.

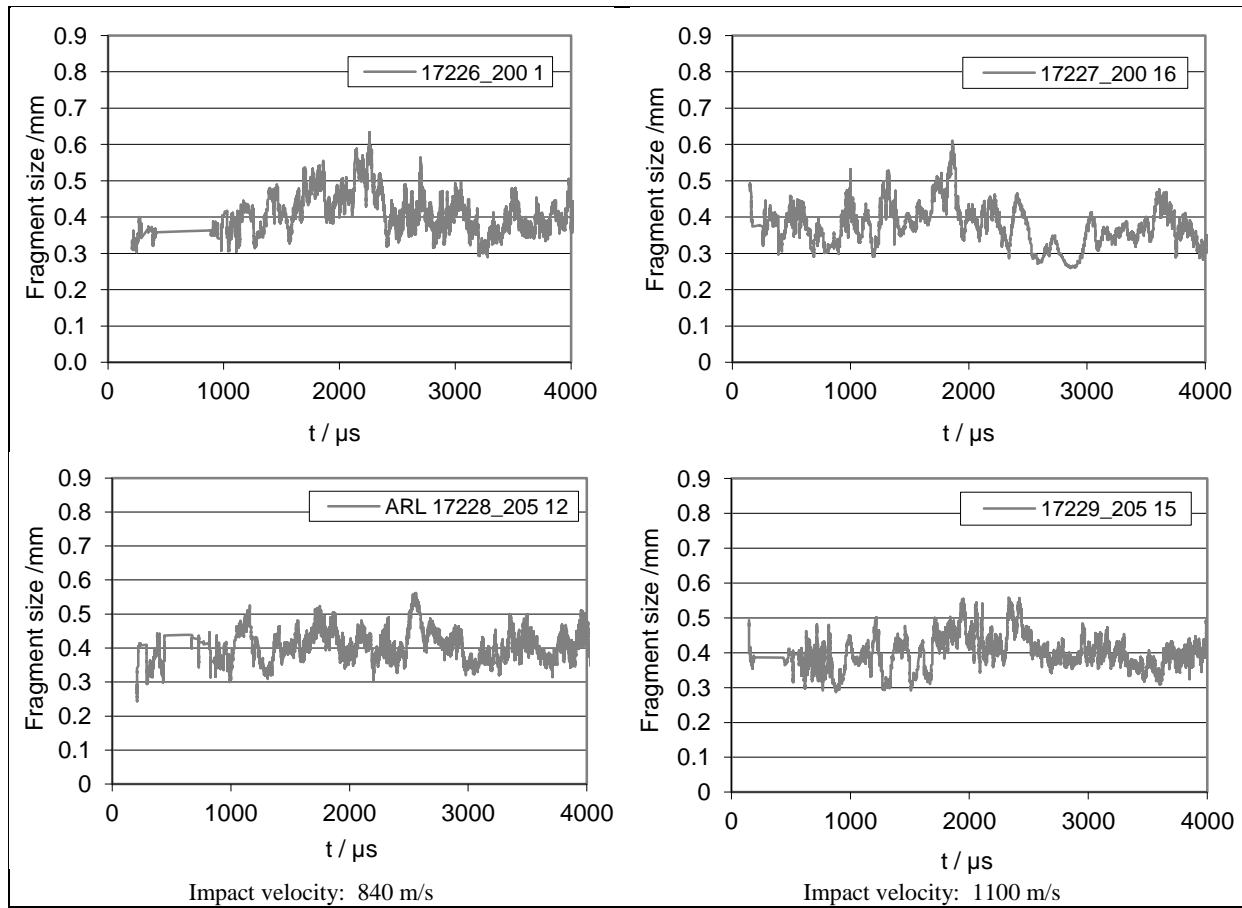


Figure 61. Average fragment size vs. time; moving average (mean of 50 frames).

Since it is assumed that the fragments appearing in the beginning have been in contact with the projectile and contributed to projectile erosion, the fragment sizes during the first several hundred microseconds need to be scrutinized. Figure 62 shows the first millisecond of the fragment size distributions from the four tests and the moving average of 10 consecutive photographs. The periods where no fragments could be registered lasted several hundreds of microseconds in some tests. One reason could be an inhomogeneous spatial distribution of the fragments, though a too-high density of particles can also prevent the recognition of single fragments. Note that particles smaller than 170 μm cannot be detected.

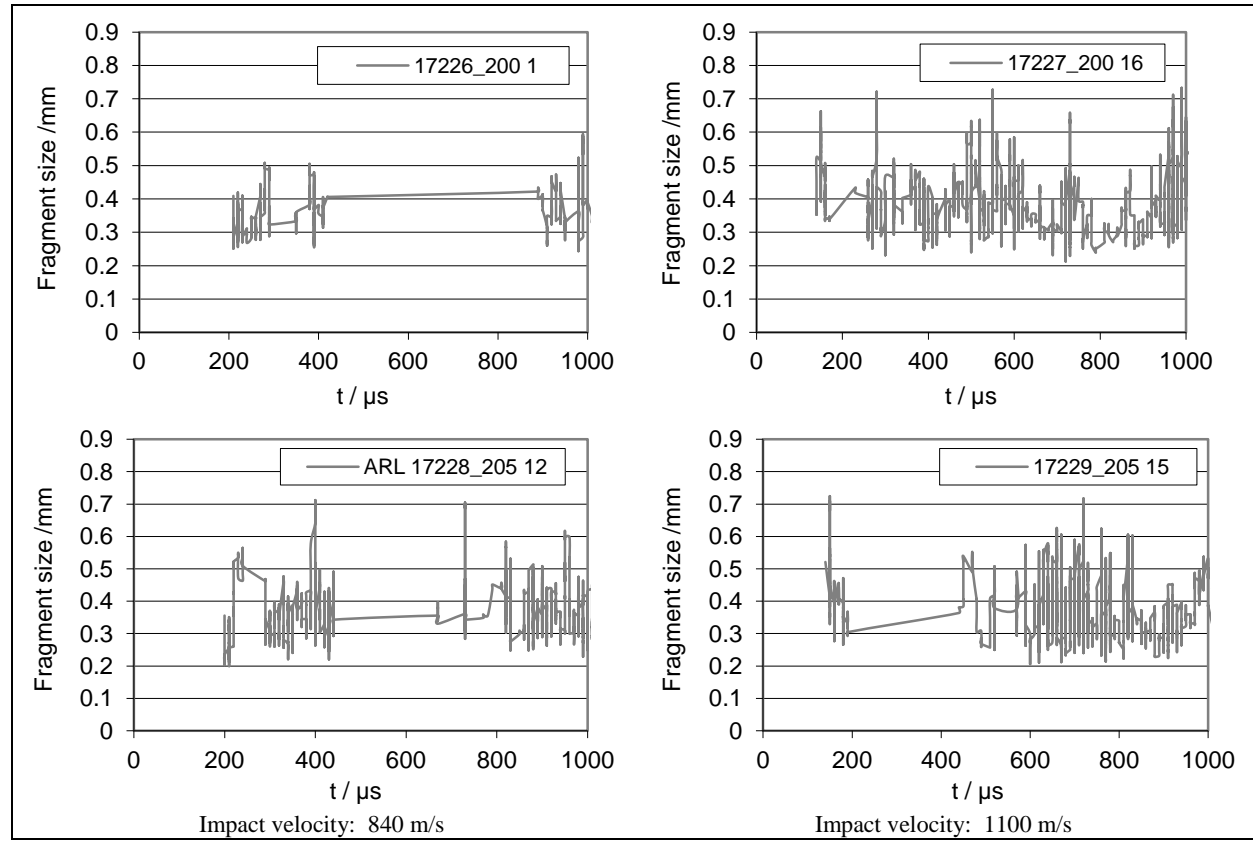


Figure 62. Average fragment size vs. time; moving average (mean of 10 frames).

In the first series of tests (no. 17226–17229), the measuring area was a rectangle of 3.1×50 mm positioned above the shot axis so that, theoretically, all fragments ejected from the impact area at an angle $\leq 50^\circ$ could be registered. For the second series (no. 17490–17493), an improved version of the high-speed camera was available, which allowed a measuring area of 4×70 mm at the same frame rate (100 kHz) and spatial resolution. The measuring area could, therefore, be positioned at a greater distance to the target. However, time intervals with no particle recognition also occurred.

The form and density of the fragment cloud also depend on the target configuration, i.e., type and thickness of ceramic and the types of backing and bonding layer. To get a complete record of the size distribution of the ejected fragments during the first hundreds of microseconds, pretests are necessary to establish the best position of the measuring area, and a higher number of tests with particle tracking will be required.

No significant differences with respect to fragment size as a function of time can be recognized during the first millisecond. These results are in agreement with the ballistic results, where no significant differences between the two types of spinel were observed at both impact velocities. Considering the relatively small difference in spinel grain size, the ballistic result appears plausible and consistent with other test results. Only minor differences have been observed with spinel ceramics of grain sizes ranging from 0.5 to 35 μm in tests with a similar impact configuration (6). It has also been demonstrated that the influence of grain size on the hardness of transparent spinel ceramics is small (7). Only in the far sub- μm range was a significant increase of hardness observed.

4.8.5.3 Summary

The fragmentation of two types of spinel with average grain sizes 0.6 and 1.6 μm , under impact of 7.62-mm AP projectiles at two different impact velocities, was analyzed. Different methods were applied to study the fragmentation behavior.

Sieving analysis of the recovered fragments revealed a higher degree of fragmentation with the material of smaller grain size at both impact velocities.

From high-speed photographs, a fracture velocity of \sim 3000 m/s was determined for both materials and impact velocities.

Ceramic fragments were ejected from the impact area at velocities in the range from 500 to 650 m/s.

The size distribution of the ceramic fragments shortly after formation and ejection from the crater area was analyzed by means of the laser lightsheet illumination technique coupled with a high-speed video camera. Average fragment sizes in the range from 0.2 to 0.5 mm were measured.

No significant differences with respect to fragment size as a function of time could be recognized during the first millisecond. These results were in agreement with the ballistic results, where no significant differences between the two types of spinel were observed at both impact velocities.

References

1. Strassburger, E. Ballistic Testing of Transparent Armour Ceramics. *Journal of the European Ceramic Society* **2009**, *29*, 267–273
2. Curran, D. R.; Seaman, L.; Shockley, D. A. Dynamic Failure in Solids. *Phys. Today* **1977**, *30* (46), 1977
3. Shockley, D. A.; Bergmannshoff, D.; Curran, D. R.; Simons, J. W. Physics of Glass Failure During Rod Penetration. *Advances in Ceramic Armor IV, Ceramic Engineering and Science Proceedings* **2008**, *29* (6), 23–32.
4. Curran, D. R.; Shockley, D. A.; Simons, J. W. Mesomechanical Constitutive Relations for Glass and Ceramic Armor. *Advances in Ceramic Armor IV, Ceramic Engineering and Science Proceedings* **2008**, *29* (6), 3–13.
5. Krell, A.; Strassburger, E. Hierarchy of Key Influences on the Ballistic Strength of Opaque and Transparent Armor. *Advances in Ceramic Armor III, Ceramic Engineering and Science Proceedings* **2008**, *28* (5), 45–55.
6. Strassburger, E.; Hunzinger, M.; Krell, A. Fragmentation of Ceramics Under Ballistic Impact. *Proceedings of the 25th International Symposium on Ballistics*, Beijing, China, 17–21 May 2010, International Ballistics Society, Vol. 2; pp 1172–1179
7. Krell, A.; Hutzler, T.; Klimke, J.; Potthoff, A. Nano-Processing for Larger Fine-Grained Windows of Transparent Spinel. *Advances in Ceramic Armor VI, Ceramic Engineering and Science Proceedings* **2010**, *31* (5).

5. Summary and Conclusions

It is our belief that this is the first detailed study attempting to relate the ballistic performance of a transparent armor ceramic material with two significantly different grain sizes to a comprehensive set of material characteristics (phase, microstructure, and defects) and quasi-static and dynamic properties.

The fine-grain spinel material V50 was determined to be about 60 ft/s (18 m/sec) better than the coarser grain material. This is close to a difference that is considered to be significant. Tables ES-1 and ES-2 depict the full set of materials characteristics and properties considered to be important in our analysis.

The key characteristics and properties we focused on consisted of the following: porosity determined indirectly from density measurements, hardness, bulk plasticity from load/Knoop hardness curves, spherical indentation, quasi-static bend-bar strength, dynamic compressive strength, and quantification of fragmentation in a ballistic impact event. Although the density determined from B-size bend-bars at 3.57 g/cm^3 for both materials is about 100% of theoretical density, densities determined from smaller Kolsky bar specimens show a much wider range and average densities of 3.552 g/cm^3 (99.5%) for the fine grain and 3.539 g/cm^3 (99.1%) for the coarser grain material. Thus, on a finer scale the fine-grain material has less overall porosity than the coarser material, which would lead to a larger V50 for the fine-grain material without considering other variations in the materials. The clearly visible yellow spots in the coarser material were not solid defects/inclusions that would nucleate cracks, but rather apparent clusters of very fine pores resulting from the lithium fluoride sintering aid. Hardness determined from standard Knoop and Vickers tests showed no differences. However, using a Meyers test, the fine-grain material had a hardness (14.8 GPa) slightly larger than the coarser material (13.5 GPa). In the spherical indentation test, the onset of observable dimpling in the fine-grain material occurred at a load of 49 N compared to the other material at 32 N, and the yield stress was, respectively, 12.16 and 11.6 GPa. These data suggest that the fine grain material is more resistant to penetration than the coarser material. There were no significant differences in the bend strength, Weibull modulus, or fracture toughness.

The highest strain rate ($10^{3\text{s}^{-1}}$) compression test (more related to a ballistic event) resulted in a slightly larger compression strength (4.35 GPa) for the fine-grain material over the other material (4.20 GPa)—a very small difference. Two series of measurements were carried out in the ballistic tests: perpendicular impact depth into the aluminum backup plate and quantification of the fragmentation in the plates. In the former, there were very small differences, but the depth in the Al plate for the fine-grain material was slightly larger for both velocities than the coarser material. The total mass of the fragments greater than 2 mm were larger for both velocities in the coarse-grain material. This suggests that if the Krell et al.

hypothesis is correct, the coarse-grain material should have a slower penetration velocity after dwell than the fine-grain material. Finally, the transitional velocity was calculated using the McCauley-Wilantewicz methodology, resulting in 1207 m/s for the fine-grain material and 1219 m/s for the other material.

From the current analysis of these data, it is hard to draw immediate relationships and conclusions relating to the dominant effects of the key material characteristics and properties. There are ongoing investigations into domestically produced spinels that are more coarse-grained microstructures. The challenge in benchmarking these materials to the materials studied here are the differences in processing, such as powder source, concentrations of sintering/processing aids, and densification process. These differences lead to varying microstructures. However, more systematic analysis may shed more clarity on this critical subject. It does seem clear that grain size can have a significant influence on ballistic performance and further grain-size reduction, further into the nanostructure range, may show even better ballistic performance for these materials.

<u>NO. OF COPIES</u>	<u>ORGANIZATION</u>	<u>NO. OF COPIES</u>	<u>ORGANIZATION</u>
1 (PDF)	DEFENSE TECHNICAL INFORMATION CTR DTIC OCA 8725 JOHN J KINGMAN RD STE 0944 FORT BELVOIR VA 22060-6218	1 (PDF)	COMMANDER US ARMY RSRCH OFC D STEPP PO BOX 12211 RSRCH TRIANGLE PARK NC 27709-2211
1 (PDF)	DIRECTOR US ARMY RESEARCH LAB RDRL CIO LL 2800 POWDER MILL RD ADELPHI MD 20783-1197	1 (PDF)	NAVAL SURFACE WARFARE CTR CARDEROCK DIV R PETERSON CODE 28 9500 MACARTHUR BLVD WEST BETHESDA MD 20817-5700
1 (PDF)	GOVT PRINTG OFC A MALHOTRA 732 N CAPITOL ST NW WASHINGTON DC 20401	1 (PDF)	LAWRENCE LIVERMORE NATL LAB J E REAUGH L282 PO BOX 808 LIVERMORE CA 94550
1 (PDF)	NATL INST OF STANDARDS & TECH G QUINN MS 852 GAITHERSBURG MD 20899	1 (PDF)	SANDIA NATL LAB E STRACK PO BOX 808 ALBUQUERQUE NM 8715-0820
1 (PDF)	ASSOC DIR MTRLS & STRUCTURES OASD(R&E) WEAPONS SYS AT&L (ASDR&E) L SLOTER 4800 MARK CTR DR STE E 17E08 ALEXANDRIA VA 22350-3600	1 (PDF)	RUTGERS THE STATE UNIV OF NJ DEPT OF CRMCS & MATLS ENGRG R HABER 607 TAYLOR RD PICATINNY NJ 08854
1 (PDF)	WASHINGTON ST UNIV INST OF SHOCK PHYSICS Y GUPTA PULLMAN WA 99164-2814	1 (PDF)	THE UNIV OF TEXAS AT AUSTIN S BLESS IAT 3925 W BRAKER LN STE 40 AUSTIN TX 78759-5315
1 (PDF)	COORS CERAMIC CO F ANDERSON 600 9TH ST GOLDEN CO 80401	1 (PDF)	COMMANDER US ARMY TACOM AMSTA TR S L PROKURAT FRANKS WARREN MI 48397-5000
1 (PDF)	SIMULA INC V KELSEY 10016 1ST ST PHOENIX AZ 85044	4 (PDF)	JOHNS HOPKINS UNIV DEPT OF MECH ENGRG K T RAMESH T W RIGHT L CHROHM-BRADY K HEMKER 3400 CHARLES ST BALTIMORE MD 21218
1 (PDF)	PM HBCT SFAE GCS HBCT S J ROWE MS 506 6501 11 MILE RD WARREN MI 48397-5000		

<u>NO. OF COPIES</u>	<u>ORGANIZATION</u>	<u>NO. OF COPIES</u>	<u>ORGANIZATION</u>
1 (PDF)	CERADYNE INC M NORMANDIA REDHILL AVE COST MESA CA 96626	RDRL WMP D T HAVEL M KEELE D KLEPONIS H MEYER J RUNYEON	
<u>ABERDEEN PROVING GROUND</u>			
67 (25 HC, 42 PDF)	DIR USARL RDRL DP R COATES RDRL WM P BAKER S KARNA J MCCUALEY (15 CPS) J ZABINSKI RDRL WML M ZOLTOSKI RDRL WML H T FARRAND L MAGNESS J NEWILL D SCHEFFLER R SUMMERS RDRL WMM J BEATTY R DOWDING RDRL WMM A J SANDS RDRL WMM B G GAZONAS T WEERASOORIYA RDRL WMM D E CHIN K CHO R SQUILLACIOTI RDRL WMM E J LASALVIA P PATEL (10 CPS) J P SINGH RDRL WMM F J MONTGOMERY RDRL WMP S SCHOENFELD RDRL WMP B C HOPPEL M SCHEIDLER RDRL WMP C R BECKER T BJERKE J CLAYTON D DANDEKAR M GREENFIELD S SEGLETES W WALTERS	RDRL WMP E P BARTKOWSKI M BURKINS W GOOCH D HACKBARTH E HORWATH T JONES	